CORRELATIVE IMAGING AND SPECTROSCOPY OF FUNCTIONAL LAYERS COMPOSED OF NANOPARTICLES AND MOLECULE AGGREGATES

Dissertation
zur Erlangung des akademischen Grades

doctor rerum naturalium (Dr. rer. nat.)

der Mathematisch-Naturwissenschaftlichen Fakultät
der Universität Rostock

Universität Rostock
Traditio et Innovatio

INSTITUT FÜR PHYSIK

vorgelegt von
Kevin Oldenburg

Rostock, Juni 2020

https://doi.org/10.18453/rosdok_id00002803

BETREUER/IN:	Prof. Dr. Sylvia Speller (Universität Rostock) Dr. Ingo Barke (Universität Rostock)
GUTACHTER/IN:	Prof. Dr. Sylvia Speller (Universität Rostock) Prof. Dr. Winfried Daum (Technische Universität Clausthal)
TAG DER EINREICHUNG:	09.06.2020
TAG DER VERTEIDIGUNG:	23.10.2020

ABSTRACT

Organic dyes are promising candidates for a manifold of new devices due to their striking and versatile optical and electronic properties. In this work, heterogeneous structures consisting of copper porphyrins and tetracene are investigated mainly by photoemission electron microscopy (PEEM) in the vicinity of small silver nanoparticles where strong coupling phenomena are expected to occur. As shown for silver clusters on a pristine silicon surface, an important effect is strong coupling to the substrate leading to dramatically altered plasmonic properties which have to be treated beyond the commonly employed dipole approximation. By utilizing the plasmonic properties of the nanoparticles, it was possible to locally excite molecular aggregates by the enhanced plasmonic near-field. This demonstrates their role as couplers from far-field to near-field to excitons with promising potential in future organic optoelectronic devices.

ZUSAMMENFASSUNG

Aufgrund ihrer vielfältigen und bemerkenswerten optischen und elektronischen Eigenschaften sind organische Farbstoffe vielversprechende Kandidaten für eine Vielfalt neuer Anwendungen. In dieser Arbeit werden heterogene Strukturen aus Kupfer-Porphyrin und Tetracen in der Umgebung kleiner Silbernanopartikel primär mit dem Photoemissions-Elektronenmikroskop (PEEM) untersucht, wobei das Auftreten starker Kopplungsphänomene erwartet wird. Wie für Silbercluster auf einer reinen Siliziumoberfläche gezeigt werden konnte, führt die starke Kopplung zum Substrat zu drastisch veränderten plasmonischen Eigenschaften, welche jenseits der üblich verwendeten Dipolnäherung behandelt werden müssen. Durch Ausnutzen der plasmonischen Eigenschaften der Nanopartikel konnten molekulare Aggregate lokal, durch das verstärkte Nahfeld, angeregt werden. Dies veranschaulicht ihre Bedeutung als Koppler zwischen Fernfeld, Nahfeld und Exzitonen mit einem vielversprechendem Potential für zukünftige Anwendungen in der organischen Optoelektronik.

CONTENTS

LIST OF ABBREVIATIONS vii

1 INTRODUCTION 1

2 CONCEPTS AND THEORETICAL ASPECTS 3
2.1 Localized Surface Plasmon Polariton 3
2.1.1 Theoretical Descriptions 4
2.1.2 Plasmon Resonance Frequency 6
2.1.3 Damping and Lifetime of the Plasmon 8
2.1.4 Field Enhancement and Quality Factor 9
2.2 Excitons in Molecular Aggregates 9
2.2.1 Molecular States 9
2.2.2 Exciton Migration 10
2.2.3 Tetracene 10
2.2.4 Copper Porphyrin 12

3 EXPERIMENTAL SETUPS AND METHODS 13
3.1 Two Photon Photoemission Electron Microscopy 13
3.1.1 Basics of Photoemission Electron Microscopy 13
3.1.2 UHV PEEM System 15
3.1.3 Excitation Sources 16
3.1.4 Two Photon Photoemission 16
3.2 Sample Preparation 17
3.2.1 Si(111)-(7x7) 17
3.2.2 Cluster Production and Deposition 17
3.2.3 Molecular Evaporator 18

4 OPTICAL AND ELECTRONIC PROPERTIES OF SUPPORTED SILVER NANOPARTICLES 19
4.1 Plasmonic Properties and Cluster Surface Interaction 19
4.1.1 Plasmonic Resonance Curves 20
4.1.2 Mapping Plasmon Resonances and Dephasing Times 22
4.1.3 Correlation with Cluster Heights 24
4.1.4 Plasmon Resonance Splitting on Si(111)-(7x7) 26
4.1.5 Discussion 27
4.2 Kinetic Energies of the Photoelectrons 36
4.2.1 Spectral Dependence on Excitation Wavelength 36
4.2.2 Spatial Contributions 37
4.2.3 Determining the Work Function 42
4.2.4 Spectral Dependence on Polarization 42
4.2.5 Spectral Dependence on Excitation Intensity 44
4.2.6 Discussion 45
4.3 Distribution of Electron Emission Angles 57
4.4 Conclusion 57

5 TETRACENE AND SILVER NANOPARTICLE HYBRID SYSTEM 59
5.1 Morphology of Evaporated Tetracene . . . 59
5.2 Silver Nanoparticles on Tetracene Films . . . 61
5.2.1 Appearance at Different Wavelengths . . . 62
5.2.2 Electron Spectra . . . 63
5.2.3 Blinking & Bleaching . . . 63
5.2.4 Coupling Enhancement . . . 65
5.2.5 Exciton Lifetimes . . . 66
5.3 Fluorescence Lifetime Imaging . . . 68
5.4 Discussion . . . 71
5.5 Conclusion . . . 81

6 COPPER PORPHYRIN AND SILVER NANOPARTICLE HYBRID SYSTEM . . . 83
6.1 Morphology and Cluster arrangement . . . 83
6.2 Silver Nanoparticles on Copper-Porphyrin-Aggregates . . . 84
6.2.1 Broadband Illumination with Mercury Lamp . . . 87
6.2.2 Laser Excitation with fs Laser Pulses . . . 88
6.2.3 Electron Spectra . . . 89
6.2.4 Dependence on Polarization . . . 91
6.3 Discussion . . . 93
6.4 Conclusion . . . 97

7 COMPARATIVE DISCUSSION AND OUTLOOK . . . 99

A APPENDIX . . . 101
A.1 Overview of the Analyzed Samples . . . 101
A.2 Fundamental PEEM Image Processing . . . 102
A.3 Analysis of the Order of a Multiphoton Process . . . 103
A.4 Comparison of p- and s-Polarization . . . 103
A.5 Conversion of Time of Flight to Binding Energy . . . 105
A.6 Spatially Resolved Map of the Order of the Photoemission Process . . . 106
A.7 Angular Resolved Photoemission Microscopy - k-Space PEEM . . . 106
A.8 Electronically Controlled Pump Probe Using a Diode Laser . . . 109
A.9 Superposition of Incoming and from the Surface Reflected Light Fields . . . 110

BIBLIOGRAPHY . . . 111

PUBLICATIONS . . . 121
SUPERVISED MASTER PROJECTS . . . 123
PRESENTATIONS . . . 125

LIST OF ABBREVIATIONS

1PPE	one-photon photoemission
2PPE	two-photon photoemission
3PPE	three-photon photoemission
AFM	atomic force microscopy
ARPES	angle-resolved photoemission spectroscopy
ATI	above threshold ionization
CBM	conduction band minimum
CuTUP	copper 5,10,15,20-tetraundecylporphyrin
cw	continuous wave
DLD	delay line detector
DOS	density of states
EEA	exciton-exciton annihilation
EELS	electron energy loss spectroscopy
FLIM	fluorescence lifetime imaging microscopy
FoV	field of view
FRET	Förster resonant energy transfer
FWHM	full width at half maximum
HAADF-STEM	high-angle annular dark-field scanning transmission electron microscopy
HOMO	highest occupied molecular orbital
HOPG	highly oriented pyrolytic graphite
HR-TEM	high resolution transmission electron microscopy
IEF	imaging energy filter
IP	ionization potential
LEED	low energy electron diffraction
LSPP	localized surface plasmon polariton
LSPR	localized surface plasmon resonance
LUMO	lowest unoccupied molecular orbital
MCP	multi channel plate
nPPE	n-photon photoemission
OD	optical density
OLED	organic light emitting diode
PEEM	photoemission electron microscopy
PES	photoemission spectroscopy
QLED	quantum dot light emitting diode
SCR	space charge region
SERS	surface-enhanced raman spectroscopy
SNOM	scanning near-field optical microscopy
SPP	surface plasmon polariton
SPV	surface photovoltage
STM	scanning tunneling microscopy
TEM	transmission electron microscopy
ToF	time of flight
UHV	ultra high vacuum
UPS	ultraviolet photoelectron spectroscopy
VBM	valence band maximum
ZnTPP	zinc tetraphenylporphyrin

1 INTRODUCTION

"QLED or OLED?" is the question of choice in today's television market. A segment which underwent an incredibly rapid development in the past two decades compared to the minor changes since the invention of color television more than half a century ago. The development strongly benefited from progress in nanoscience and photonics leading for example to the utilization of quantum dots in QLED TVs. Nowadays organic light emitting diodes (OLEDs) are the first commercially successful applications in the rising field of organic electronics [1, 2]. A similar trend can be expected in other applications as sensing [3], photovoltaics [4], or lasers [5]. Not only obvious properties like flexibility, low cost production or transparency are advantages of this new technological area. Moreover, the enormous amount of different materials with individual properties forms the basis of manifold prospects and enables the design of individual organic structures on demand.

However, a solid base in fundamental research will be necessary to invent new devices instead of reinventing existing tools with new technology. Especially heterogeneous structures combining benefits of different material classes are promising. In such systems especially the interaction and energy transfer at interfaces is in the focus of interest since most materials are individually well studied. The aim of this work is to study such fundamental interactions in a class of heterogeneous model systems such as shown in Figure 1.1.

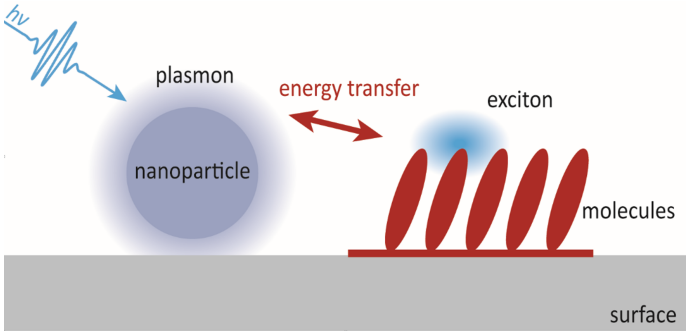

Figure 1.1: Schematic representation of a heterogeneous model system consisting of plasmonic nanoparticles and molecular aggregates on a surface. The system shows various complex couplings which are in the focus of this work.

The hybrid structure consists of metallic nanoparticles in near vicinity of molecular aggregates both deposited on a substrate. By illuminating the nanoparticle with light at a suitable wavelength, a collective electron oscillation, known as plasmon, can be excited leading to an enhancement of light intensity in the vicinity of the particle. Within this near-field the molecules can be locally excited far below the diffraction limit of the light. The excitations in the molecules, known as excitons, could now migrate in the aggregates until they decay radiatively or non-radiatively. On the other hand, the nanoparticles could quench excitations resulting in a lower excitation density in their vicinity. However, in both cases it would be possible to access this specific interaction.

In this system numerous different kinds of coupling are involved: the interaction between light and plasmon, the coupling and energy transfer between plasmon and exciton, and all the couplings with the substrate affecting each of the processes.

To address individual types of coupling in this heterogeneous system and to avoid statistical ensemble averaging a microscopic approach is necessary or at least highly beneficial. This allows direct observation in real space and enables access to the influence

of local structural differences like morphology, cluster size, or defects. By using time resolved photoemission electron microscopy (PEEM) in combination with a tunable femtosecond laser system a simultaneous measurement of spatially, time and energetically resolved spectra becomes possible allowing conclusion on the spatial distribution of involved electronic states, lifetimes, local field strengths, amongst other quantities. The measurements are complemented by correlative atomic force microscopy (AFM) and high resolution transmission electron microscopy (HR-TEM) to associate the results with morphological information, and by fluorescence lifetime imaging microscopy (FLIM) to increase the available timescales of observed lifetimes and to validate the results with an established method.

The main concepts and theoretical basics will be briefly introduced in Chapter 2, in particular localized surface plasmon polaritons (LSPPs) and excitons in molecular aggregates. Chapter 3 gives an overview of the used experimental equipment and explains details of the sample preparation.

In Chapter 4 the coupling between silver nanoparticles in a size range between 10 and 35 nm and light is studied. To unravel the role of the substrate both natively oxidized and pristine silicon was used. Although such systems are well studied in ensemble measurements [6–8], statistical relevant data of individual nanoparticles can rarely be found in literature. Hence, we can use the knowledge from ensemble measurements to benchmark our detection method and benefit from the spatial resolution to study the individuality of the couplings. Special focus is put on the influences of the cluster sizes and the substrate on the plasmon resonance. In addition, the effect of the nanoparticles on the evolution of a surface photovoltage (SPV) can be analyzed.

After having studied the isolated system of silver nanoparticles on a substrate we expand the studies to the full heterogeneous system in Chapter 5 by including a tetracene film as an organic molecular aggregate. Tetracene crystals are well studied and long range exciton migration was shown [9]. In addition, it forms two triplet excitons by a singlet fission process [10] upon absorption of one photon of the wavelength of typical silver plasmon resonances. Hence, tetracene is a promising candidate to study the coupling of plasmon and exciton. Relevant scientific questions are: Do plasmon and exciton affect each other? Is a possible coupling beneficial for the transfer of light into the molecular aggregates? Can we selectively and locally excite molecules by utilizing the nanoparticles as far-field near-field couplers? Are there signatures of exciton migration processes and can we image them? How does the local molecular structure affect migration? What is the lifetime of those excitations? Especially to answer the latter question additional FLIM measurements are presented at the end of this chapter.

Afterwards we change the molecule from pure organic towards a copper coordination complex and study a hybrid system of silver nanoparticles and copper porphyrin molecules in Chapter 6. Here, the morphology is substantially different forming large branch like structures possibly enabling a directional long range exciton transport. Similar aggregates were already studied in our group with various methods leading to a broad knowledge of the aggregates' properties [11, KO-2]. The system will be studied for the same scientific aspects as the tetracene system.

Finally, the results are summarized, and comparative conclusions are drawn together with an outlook for future work in Chapter 7.

CONCEPTS AND THEORETICAL ASPECTS 2

In this chapter theoretical basics relevant for a general understanding of the main part are introduced. We start with some properties of localized surface plasmon polaritons which are the key topic in Chapter 4. Afterwards, the fundamentals of molecular excitations are explained. At the end, the molecules studied in this work, namely tetracene (Chapter 5) and the synthesized copper 5,10,15,20-tetraundecylporphyrin (CuTUP) (Chapter 6) are described, and peculiarities concerning electronic excitations are presented.

2.1 LOCALIZED SURFACE PLASMON POLARITON

A plasmon is a quasi particle representing a quantized collective oscillation of quasi-free electrons. Plasmons in solids are often referred to as bulk or volume plasmons which are, different than photons, longitudinal waves [12]. Three different types of plasmons are commonly distinguished, namely bulk, surface, and particle (or localized surface) plasmons. Due to the strong coupling especially of surface and particle plasmons to the electromagnetic field they are (localized) surface plasmon polaritons.

Let us start with the plasma frequency of a free electron gas as frequently used as model for the description of metals with quasi-free electrons. Within the Drude-Sommerfeld model [13] we can write the plasma frequency as

$$\omega_P = \sqrt{\frac{n_e e^2}{m^* \epsilon_0}} \tag{2.1}$$

with the density of free electrons n_e, the elementary charge e, the effective mass of conduction electrons m^*, and the vacuum permittivity ϵ_0. Exemplarily calculating the plasmon energy for silver using values from [14, 15] gives $E_P = \hbar\omega_P = 9.1\,\text{eV}$ as can be measured by electron energy loss spectroscopy (EELS) [16, 17].

While these bulk plasmons are restricted to the volume of solids, surface plasmon polaritons are confined at the interface between a conductor and a dielectric. These propagating longitudinal waves with a strong localization at the interface can be used to guide light [18], amongst others. However, due to the momentum mismatch within the surface plasmon and the photon dispersion it can not be excited directly by light shining on the interface. To provide an additional momentum to the photon the light is guided through a medium with a high refractive index which could be a prism either in Otto [19] or Kretschmann configuration [20]. Another possibility for coupling is to disturb the plasmon mode by a regular grating at the interface [12, 21]. In addition to this, excitations over a macroscopic area, surface plasmon polaritons (SPPs) can be excited within the near-field of an optical microscope probe as in a SNOM for example. Phase matching is naturally allowed due to the probe geometry [12]. After successful excitation, the SPP can be visualized with different techniques such as e. g. near-field microscopy, PEEM or indirectly by placing fluorescent emitters on the interface [12, 21].

Within the Drude-Sommerfeld model under negligible damping we can find the SPP frequency to be

$$\omega_{\text{SPP}} = \frac{\omega_p}{\sqrt{1+\epsilon_m}} \tag{2.2}$$

with the permittivity of the dielectric medium ϵ_m. Hence, for the conductor vacuum interface we observe $\omega_{\text{SPP}} = \omega_p/\sqrt{2}$.

In contrast to this propagating plasmons, we can excite non-propagating so called localized surface plasmon polaritons in metallic nanostructures. Due to the curvature of nanoparticles these excitations can be directly excited by light [12]. Here, electrons displaced due to an external electric field encounter a restoring force leading to an oscillating behavior and the development of a resonance with a field amplification in the near-field of the particle.

2.1.1 THEORETICAL DESCRIPTIONS

To theoretically describe the interaction of a nanoparticle with an electromagnetic field, several approaches exist. Let us have a closer look on the lowest order approximation working adequately for most purposes with particles of 50 nm diameter and below [12]. The following derivation will sketch the key points to solve this problem and will follow the book of Maier [12]. For a detailed description see [22].

For particles with a diameter d much smaller than the wavelength λ of the incident light ($d \ll \lambda$), we can use the quasi-static approximation assuming that the phase of the electromagnetic field is constant over the entire particle volume, which brings us to an electrostatic problem for each time. We model the particle to have a spherical shape and a dielectric response described by the complex dielectric function $\epsilon(\omega)$. By solving the Laplace equation $\nabla^2\Phi = 0$ for the potential Φ we can calculate the electric field with $\boldsymbol{E} = -\nabla\Phi$. Due to the azimuthal symmetry we can write the solution as [22]

$$\Phi(r,\theta) = \sum_{l=0}^{\infty}[A_l r^l + B_l r^{-(l+1)}]P_l\cos(\theta) \tag{2.3}$$

with the Legendre Polynomials $P_l\cos(\theta)$ and θ being the angle between the position vector $\boldsymbol{r}$ and the incident electric field. By splitting Φ into a potential inside Φ_{in} and outside the sphere Φ_{out} and applying necessary boundary conditions at the interface and far away from the sphere, we can determine the coefficients A_l and B_l which brings us to

$$\Phi_{out} = -E_0 r\cos(\theta) + \frac{\epsilon-\epsilon_m}{\epsilon+2\epsilon_m}E_0 d^3\frac{\cos(\theta)}{r^2} \tag{2.4}$$

describing the superposition of the incident field $\boldsymbol{E_0}$ and the induced dipole at the particle center. We can rearrange this equation with the use of the dipole moment $\boldsymbol{p}$ to

$$\Phi_{out} = -E_0 r\cos(\theta) + \frac{\boldsymbol{p}\cdot\boldsymbol{r}}{4\pi\epsilon_0\epsilon_m r^3} \quad \text{with} \quad \boldsymbol{p} = 4\pi\epsilon_0\epsilon_m d^3\frac{\epsilon-\epsilon_m}{\epsilon+2\epsilon_m}\boldsymbol{E_0} \quad . \tag{2.5}$$

By using $\boldsymbol{p} = \epsilon_0\epsilon_m\alpha\boldsymbol{E_0}$ we can write the polarizability α of a small sphere in dipole approximation as

$$\alpha = 4\pi d^3\frac{\epsilon-\epsilon_m}{\epsilon+2\epsilon_m} \quad . \tag{2.6}$$

With this we can easily see that the enhancement is maximal when $|\epsilon+2\epsilon_m|$ is a minimum. Under the assumption of a slowly varying $\Im(\epsilon)$ we obtain the Fröhlich condition for the dipole surface plasmon of a metallic nanosphere:

$$\Re[\epsilon(\omega)] = -2\epsilon_m \quad . \tag{2.7}$$

For a Drude like metal sphere in vacuum this condition is fulfilled at the localized surface plasmon resonance (LSPR) with

$$\omega_{\text{LSPPR}} = \frac{\omega_P}{\sqrt{3}} \quad . \tag{2.8}$$

The corresponding cross-sections for absorption C_{abs}, scattering C_{sca} and extinction C_{ext} are [12, 23]

$$C_{\text{abs}} = 4\pi \frac{\omega}{c} d^3 \Im\left[\frac{\epsilon - \epsilon_m}{\epsilon + 2\epsilon_m}\right] \tag{2.9}$$

$$C_{\text{sca}} = \frac{8\pi}{3}\left(\frac{\omega}{c}\right)^4 d^6 \left|\frac{\epsilon - \epsilon_m}{\epsilon + 2\epsilon_m}\right|^2 \tag{2.10}$$

$$C_{\text{ext}} = 9\frac{\omega}{c}\epsilon_m^{3/2} V \frac{\epsilon_2}{(\epsilon_1 + 2\epsilon_m)^2 + \epsilon_2^2} \tag{2.11}$$

with the speed of light c and $\epsilon = \epsilon_1 + i\epsilon_2$. Note the different scaling of absorption and scattering with d having massive influence on experimental purposes.

Beside this quasi-static approximation, an exact solution of the Maxwell equations for spheres in a homogeneous environment exists which is known as Mie theory [24]. However, for small particles ($d < 50\,\text{nm}$) the accordance is sufficient for most purposes as shown in Figure 2.1 where the Mie extinction cross-section of a 20 nm silver sphere is compared to the result obtained within dipole approximation.

To overcome the geometrical restrictions several extensions of the Mie theory exist allowing calculations for e. g. core-shell particles [25–27], non-spherical geometries [28] (see [29] for an overview), aggregated particles [30, 31], Gaussian beam illumination [32, 33] or a sphere on a flat surface [34]. However, for complicated geometries that do now allow solving Maxwell's equations analytically several numerical methods are available, e. g. discrete dipole approximation (DDA) [35], multipole multipole method [36], and finite difference time domain (FDTD) method [37, 38].

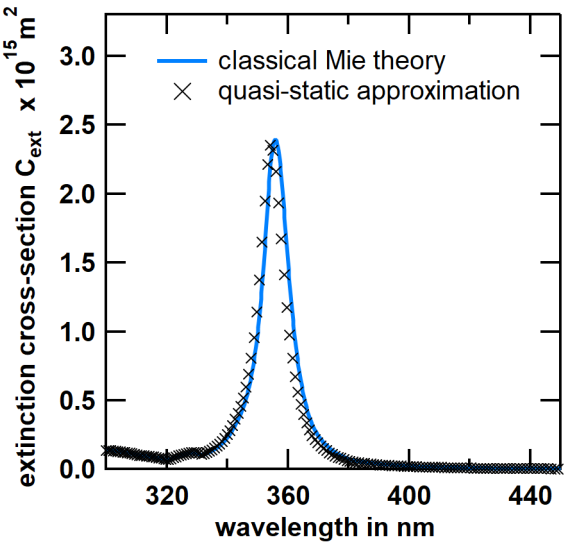

Figure 2.1: Extinction cross-sections of a silver sphere ($d = 20\,\text{nm}$) in vacuum calculated with Mie theory (blue line) [24, 39] and in quasi-static approximation (black crosses).

2.1.2 PLASMON RESONANCE FREQUENCY

Determining the actual plasmon resonance frequency of individual nanoparticles is the key topic in Section 4.1. In general, the resonance depends on the composition of the nanoparticle, strictly speaking its dielectric function $\epsilon(\omega)$, the size of the nanoparticle, the shape, and the dielectric properties of the local environment [29, 40].

Composition and Structure

As we have seen for example in the Fröhlich criteria (Equation 2.7) the dielectric function of a material is significantly determining its plasmonic properties. Figure 2.2 shows the LSPR extinction cross-sections of gold and silver spheres with a diameter of 20 nm as a function of wavelength calculated with Mie theory [39]. While the silver resonance is around 350 nm, the one of gold is red-shifted to $\approx$ 500 nm. In addition, it is much weaker and significantly broadened compared to silver. As we will see in Section 2.1.3 this is a direct consequence of a stronger damping of the resonance.

In addition to the differences in the material, clusters can be composed of material gradients or as core-shell particles with an oxide layer for example. These kinds of compositions are more complex and not in the focus of this work. For further details see [25–27, 29, 40].

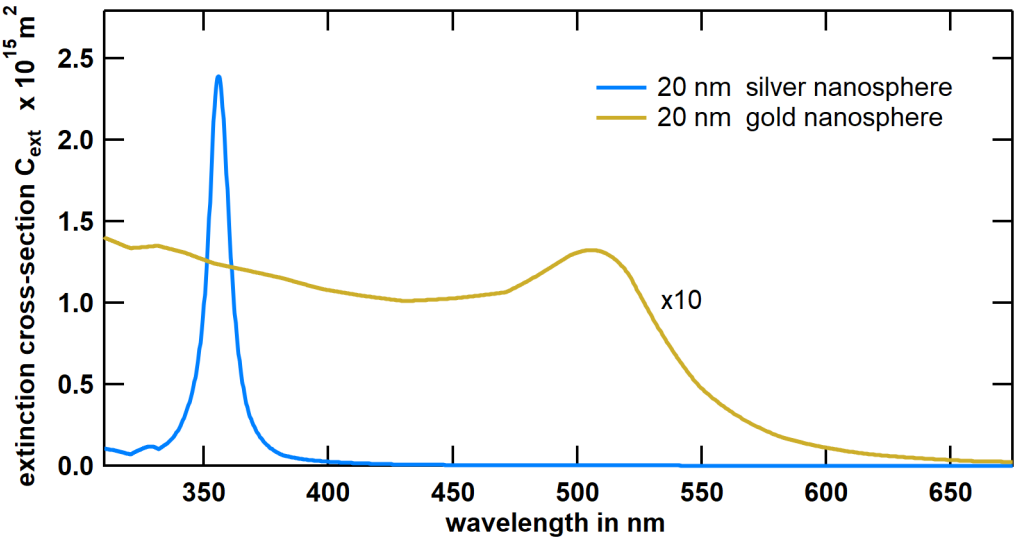

Figure 2.2: Extinction cross-sections of a silver (blue curve) and a gold (yellow) sphere ($d = 20$ nm) in vacuum calculated with Mie theory [39].

Size

In addition to the material the size of the nanoparticle plays a role. In quasi-static approximation we have no size-dependence included since for particles up to 20 nm the dependence on particle size is weak as can be seen in Figure 2.3 showing the plasmon resonance of silver spheres in vacuum with diameters between 10 nm and 50 nm. With increasing size the resonance is red-shifted and the extinction cross-section increases. In particular the logarithmic plot in b) shows the weak dependence of the resonance on the cluster size below 20 nm which becomes steeper for larger nanoparticles. This behavior has its origin in retardation effects[1] and can be shown by expanding the first mode in Mie theory leading to a size dependent polarizability [41, 42]. An intuitive explanation

1 Here, retardation of the exciting field over the sphere as well as retardation of the depolarization field inside the particle causing a red-shift of the resonance for Drude and noble metals [12].

is the increasing distances of charges at opposite interfaces with increasing particle size leading to a weaker restoring force. However, for sizes below 10 nm the resonance is shifting towards higher energies with decreasing particle size. Here, the particle size becomes smaller than the mean free path of the oscillating electrons [12]. This behavior was experimentally observed using EELS and modeled by a quantum mechanical model showing that the shift is due to a change in particle permittivity [17]. Note, that the behavior described for particles below 10 nm is valid for silver while for other materials the direction of a shift differs [12, 40].

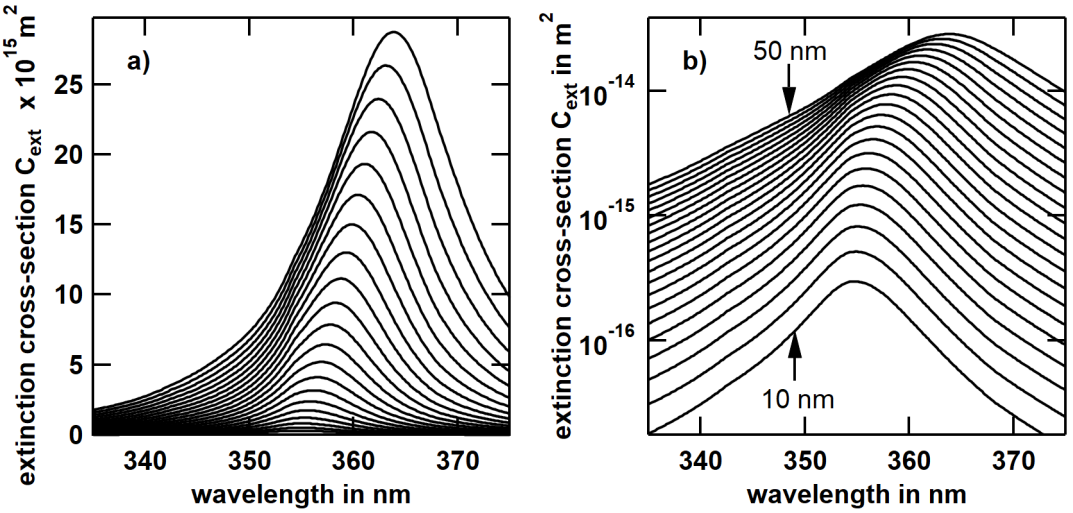

Figure 2.3: Extinction cross-sections of silver spheres with diameters from 10 nm to 50 nm in increments of 2 nm in vacuum on linear (a) and logarithmic scale (b) calculated with Mie theory [39].

Shape

Until now we always considered spherical particles for reasons of simplicity and for the possibility of using analytical models. However, in experiments particles can have arbitrary shapes having a crucial influence on the plasmon resonance frequency. In the simple case of an oblate particle, the resonance splits into two modes associated with the long- and short-axis [29, 40]. Since different shapes are not in the focus of this work, the interested reader is referred to literature [29, 40, 43, 44].

Dielectric Environment

The dielectric environment has a crucial influence on the resonance position as can already be seen in the quasi-static approximation polarizability (see Equation 2.6) and the Fröhlich condition (Equation 2.7). Figure 2.4 shows the extinction cross-sections for 20 nm silver spheres embedded in a homogeneous medium of different refractive indexes. We observe a significant red-shift of the resonance with increasing refractive index of the dielectric environment and therefore an increasing permittivity. Intuitively, we can understand this shift due to the polarizability of the medium partially shielding electric fields and therefore reducing the restoring force leading to a lower eigenfrequency of the plasmon. However, analytically considerations are mostly limited to a homogeneous medium. For most purposes it is sufficient to describe an inhomogeneous medium with an effective dielectric function ϵ_{eff}, e. g. for a particle on a substrate the dielectric function of substrate ϵ_{sub} and the medium ϵ_m above can be averaged with certain weights. Depending on the polarization of the incident light this average could be $\epsilon_{eff} = p\epsilon_{sub} + (1-p)\epsilon_m$ mostly used for s-polarization as this matches the model of two parallel capacitors or

$\frac{1}{\epsilon_{eff}} = \frac{p}{\epsilon_{sub}} + \frac{1-p}{\epsilon_m}$ for p-polarization and the model of two serial capacitors [29]. The weighting parameter p can be chosen between zero and one. However, especially for highly polarizable substrates this description with an effective permittivity does not necessarily describe the system sufficiently as we will see for small silver nanoparticles on a pristine silicon surface in Section 4.1. Here, more advanced theoretical approaches are needed as e. g. Generalized Mie theory [34] or FDTD methods [37, 38].

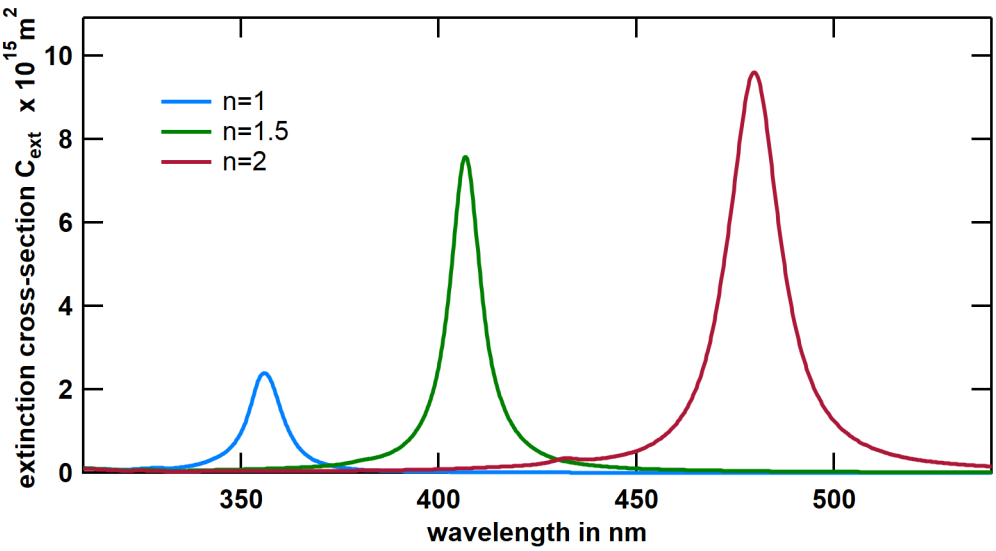

Figure 2.4: Extinction cross-sections of a silver sphere ($d = 20$ nm) embedded in three different dielectric environments with refractive index 1 (blue curve), 1.5 (green), and 2 (red) calculated with Mie theory [39].

2.1.3 DAMPING AND LIFETIME OF THE PLASMON

After excitation of the collective plasmon mode, several decay channels are present leading to a lifetime T_2 of the plasmon of a few fs [40, 45, 46]. We can divide the contributions of T_2 into a decay of the plasmon population T_1 and a pure dephasing of the collective mode T_2^*. Hence, we can write

$$\frac{1}{T_2} = \frac{1}{2T_1} + \frac{1}{T_2^*} \tag{2.12}$$

where the two in the denominator comes from the fact that T_1 is describing a population, i. e. an oscillator energy while T_2 is describing the oscillation amplitude [46].

The population decay can occur either radiatively by a decay of the coherently oscillating electrons into a photon [47] or non-radiatively via excitation of an electron-hole pair. For the latter case, we can distinguish intraband and interband damping depending on the origin of the electron getting excited into the conduction band mainly due to scattering events [46, 48].

The population decay itself is strongly size dependent, while smaller particles are mostly damped non-radiatively, larger particles however decay preferentially radiatively as can be seen in the scattering cross-sections. As a consequence the absorption cross-sections starts to decrease for larger particles [49], and the resonance is significantly broadened.

For the pure dephasing we look at the oscillating ensemble of electrons. Due to elastic scattering on surfaces or inhomogeneous phase velocities of individual electrons the

fixed phase correlation decays [45]. Especially for small noble metal particles ($d < 10\,\mathrm{nm}$) pure dephasing is increased due to additional elastic scattering at the particle's surface (known as chemical interface damping) since the particle is smaller than the electron mean free path [12].

Plasmon Lifetime Measurements

For the experimental determination of plasmon lifetimes, two approaches are popular. On the one hand, T_2 is accessible in the time domain for example via pump-probe experiments [48, 50]. However, in this work we will access the plasmon dephasing in the frequency domain via the energetic width Γ of the resonances[2]. Both approaches are connected by a Fourier transformation which would result in a sharp energetic plasmon resonance for the case of long lifetimes and a broadened resonance spectrum for short dephasing times. T_2 and Γ are connected by

$$\Gamma = \frac{2\hbar}{T_2} \quad . \tag{2.13}$$

2.1.4 FIELD ENHANCEMENT AND QUALITY FACTOR

An important quantity to characterize resonators is the quality factor Q, usually defined as the ratio between the enhancement of the oscillation amplitude of a driven system per cycle to the driving amplitude [51]. A more accessible approach is the ratio of resonance energy and spectral bandwidth

$$Q = \frac{E_{\mathrm{res}}}{\Gamma} \tag{2.14}$$

which corresponds to the local field enhancement factor of the LSPR [51–53]. For silver nanoparticles a typical value is in the order of 10 [46, 54, 55, KO-4] while gold nanorods can reach a factor up to 23 [51]. This has drastic consequences for the detection in nonlinear experiments like surface-enhanced raman spectroscopy (SERS) or two-photon photoemission (2PPE) as the signal increases with Q^4 [51, 56, 57].

2.2 EXCITONS IN MOLECULAR AGGREGATES

In general, an exciton is a quasi-particle describing a bounded electron hole pair. In molecular aggregates this corresponds to a bound state of excited electron and the "hole", which is the absence of an electron in the ground state. Due to the weak intermolecular coupling, molecular excitons are usually spatially confined to one or a few molecules. Hence, the exciton binding energy of this so called Frenkel excitons is relatively large ($0.1 - 1\,\mathrm{eV}$) compared to Mott-Wannier excitons which are highly delocalized and typical of inorganic semiconductors at low temperatures. In this section, we will focus on Frenkel excitons and limit the discussion to aspects critical for this work, e. g. generation, transport, and decay. For further details on excitons see [58]. We will start by looking at the typical energetic structure of single molecules.

2.2.1 MOLECULAR STATES

Figure 2.5 shows a typical Jablonski diagram of molecular states consisting of a highest occupied molecular orbital (HOMO) (S_0) and a lowest unoccupied molecular orbital

2 The homogeneous linewidth Γ is the full width at half maximum (FWHM) of the Lorentzian plasmon resonance peak.

(LUMO) (S_1) each with a manifold of vibrationally excited states and of the lowest triplet state T_1, which also can have vibrational level. In the ground state the system has two electrons in S_0 which have opposite spin, hence the total spin is 0. After absorbing a photon (1 in Figure 2.5) the system is in an excited singlet state which relaxes to the vibrational ground state in $\approx 100\,\text{fs}$ (2). Typically, we have two scenarios. The electron can radiatively decay into the ground state emitting a photon (3a) and finally vibrationally relax (4a). This process is known as fluorescence and has a typical lifetime in the ns range. Due to the vibrational relaxation processes the emission is shifted with respect to the absorption, known as Stokes shift. In contrast, the electron in the S_1 state can undergo an inter-system crossing into the triplet state T_1 (3b). During this process the spin state must be altered to a total spin of 1 which can occur by spin-orbit coupling, particularly in the presence of heavy atoms. Due to the changed symmetry of the wave function, Coulomb repulsion is lower in the triplet state lowering its energy [59]. Afterwards the triplet state can only decay in the S_0 ground state which is again spin forbidden (4b). Hence, the lifetime of this process, known as phosphorescence, is increased to several µs [58].

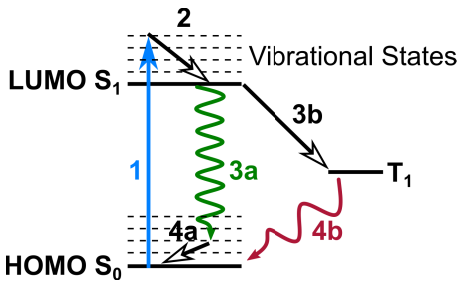

Figure 2.5: Simplified scheme of possible molecular excitation pathways. 1) absorption of a photon 2) relaxation 3a) fluorescence 4a) ground-state relaxation 3b) inter-system crossing 4b) phosphorescence

2.2.2 EXCITON MIGRATION

In a system of many molecules like a molecular aggregate, the excitations are not fixed to one molecule. Instead exciton migration is possible. Figure 2.6 illustrates two possible exciton transfer mechanisms known as Förster resonant energy transfer (FRET) (top) [60] and Dexter energy transfer (bottom) [61]. In a FRET the exciton is transferred via dipole-dipole interaction which is, due to spin restrictions, the dominant mechanism for radiative singlet excitons and works for large intermolecular distances ($\approx 5\,\text{nm}$) making the migration fast. However, the maximum migration length is fundamentally limited due to the inherent connection between diffusion constant and exciton decay rate [62]. On the other hand, the Dexter energy transfer requires an overlap of wave functions between donor and acceptor molecule to simultaneously exchange two electrons. This process is dominant for triplet excitons due to the spin restrictions from radiating. Interestingly, although Dexter type migration is slow, no fundamental limit for exciton migration lengths exists here [62].

2.2.3 TETRACENE

The first organic molecule to be studied in this work was tetracene ($C_{18}H_{12}$) which belongs to the group of polyacene molecules. The inset of Figure 2.7 shows the structure consisting of four linear benzene rings with the transition dipole ($S_0 \rightarrow S_1$) polarized along the short axis. The absorption spectra (a) for monomer, film, and aggregate is

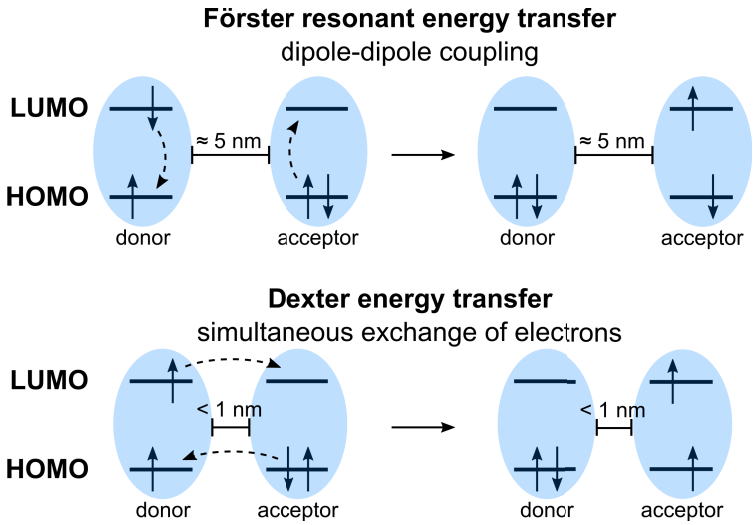

Figure 2.6: Schematic representation of FRET (top) and Dexter energy transfer (bottom). Figure adapted from [59, 62].

shown in Figure 2.7 together with the emission spectra (b). Film and aggregate have similar optical properties and show a red shift of approximately 50 nm.

Tetracene is known to form large crystals with a highly ordered internal structure e. g. when prepared by vapor phase method [9]. Moreover, laser assisted aligning during thin film deposition was reported [63]. The bulk crystal forms a triclinic lattice with unit cell dimensions of 7.9 Å × 6.0 Å × 13.5 Å [64].

Special interest in research is focused on tetracene due to a strong singlet fission, a process of splitting one singlet excitation into two triplet excitations each with approximately half the energy enabling an efficient inter-system crossing. Especially for applications in solar cell systems, this property allows to overcome the Shockley-Queisser limit by doubling the amount of charge carrier per absorbed photon [65]. The efficiency of the singlet fission is described to be high at typical resonance frequencies of silver nanoparticles potentially enabling a coupling as will be studied in Chapter 5. Once in the triplet state, excitons are known to have a lifetime up to several ten µs and a migration length above 600 nm [9, 66]. Two triplet excitons can undergo a fusion process leading to delayed fluorescence which will be studied in more detail in Section 5.3.

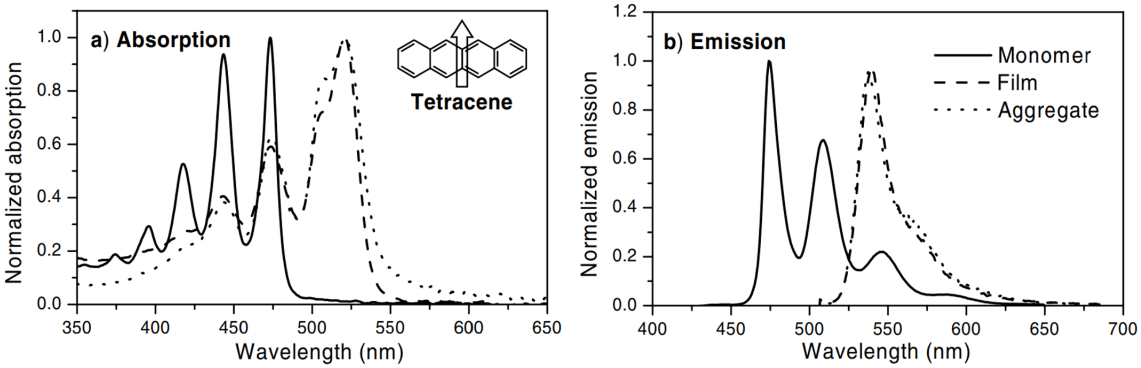

Figure 2.7: Normalized absorption (a) and emission (b) spectra of tetracene. Monomer spectra (solid line) were obtained from tetracene diluted in THF, while the film data (dashed) originate from tetracene nanoparticles in aqueous solution and aggregate data (dotted) are acquired from vacuum-deposited film. Inset: Molecular structure and orientation of transition dipole ($S_0 \rightarrow S_1$). Figure adapted from [67].

2.2.4 COPPER PORPHYRIN

Porphyrins are aromatic organic dyes composed of four pyrrole rings arranged around a center which optionally hosts a metal atom (then called metalloporphyrin). The optical and electronic properties are mainly defined by the system of delocalized π-electrons leading to a strong absorption in the visible range which especially holds for metalloporphyrins. A popular representative is heme, the pigment in red blood cells, having an iron center. In this work we use CuTUP which has a copper atom in the center and four undecyl groups ($C_{11}H_{23}$) at the meso-positions 5,10, 15 and 20 [68] as shown in the inset of Figure 2.8. Due to the interactions of the porphyrin ring with the metal center a special electronic structure with a ground state in a doublet configuration occurs [KO-2]. For a detailed description see [69, KO-2]. However, the extinction spectra of the monomer diluted in n-heptane (blue curve) and the nanostructures on glass (red) shown in Figure 2.8 have an intense peak around 400 nm which can be assigned to the Soret band excitation ($S_0 \rightarrow S_2$). The Q-bands ($S_0 \rightarrow S_1$) in between $\approx$ 500 nm and $\approx$ 600 nm are less intense due to limitations by the selection rule of Laporte [69].

It is remarkable that phosphorescence is more intense than fluorescence in this particular molecule. Due to the special electronic structure the inter-system crossing ($S_2, S_1 \rightarrow T_1$) into the triplet states is not spin forbidden and can occur via a charge transfer state [70]. Hence, a large amount of excitations take a decay path into the triplet system where they can radiatively decay via phosphorescence. In addition, a long living dark (i. e. non-radiating) state was found with a lifetime of $\approx$ 25 µs [KO-2] making this molecule a promising candidate for long range exciton migration processes. In addition, the strong absorption at the Soret band superimpose with typical plasmon resonances of silver nanoparticles as will be studied in a hybrid-system in Chapter 6.

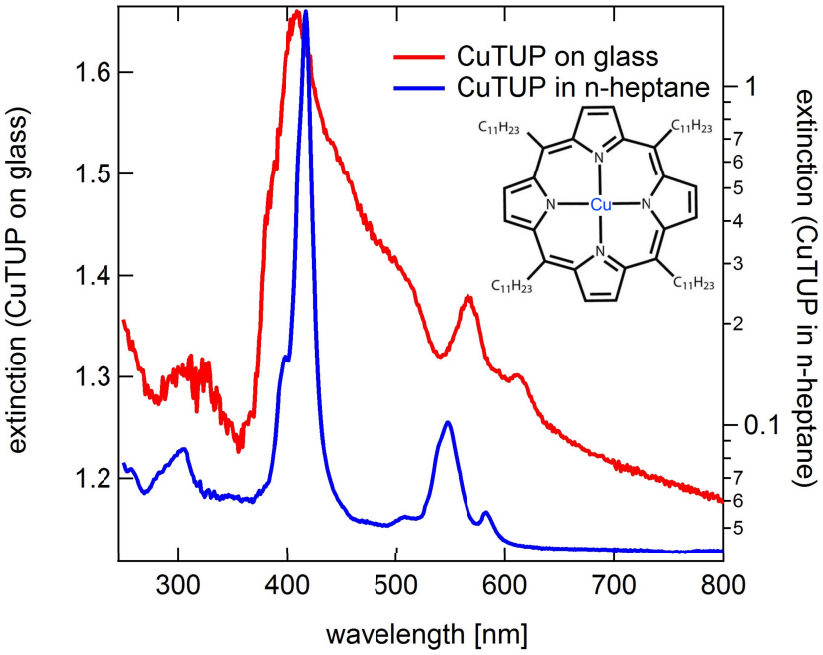

Figure 2.8: Extinction spectra of CuTUP monomer in n-heptane (blue curve) and aggregates on glass (red). The main peaks correspond to the Soret band while the smaller peaks in between $\approx$ 500 nm and $\approx$ 600 nm can be attributed to the Q-bands. Inset: Molecular structure of CuTUP. Figure adapted from [69].

3 EXPERIMENTAL SETUPS AND METHODS

After the overview of general theoretical basics we now focus on our explicit experimental setup used for this work. The main instrument used for this study is the PEEM in combination with a fs laser system which will be described in the first part of this chapter. Afterwards, we take a closer look on the sample preparation especially on the setup for cluster deposition and molecular evaporation.

3.1 TWO PHOTON PHOTOEMISSION ELECTRON MICROSCOPY

Due to the photoelectric effect a sample irradiated by light with a sufficiently small wavelength emits photoelectrons. By the use of magnetic lenses these electrons can be imaged as already shown in 1933 by Brüche [71]. Before the invention of lasers, photoemission experiments were typically performed using gas discharge lamps providing sufficient photon energy to excite an electron directly above the vacuum energy. Hence, only occupied states can be probed. To access unoccupied states via photoemission a two step process is necessary where first the electron is excited into an unoccupied state by absorbing a photon and afterwards can be probed by absorbing a second photon within its lifetime and getting photoemitted. However, the yield of this process scales with the square of the light intensity [72, 73] and is therefore strongly suppressed in non-coherent excitation sources. Fortunately, the invention of laser light sources enabled probing of intermediate states via 2PPE and added flexibility in the choice of the photon energy. Especially for short living intermediate states pulsed lasers became more important and gave access to temporal information via pump-probe experiments. In addition to real intermediate states also quasiparticle states, as plasmonic oscillations of an electron system can be imaged by 2PPE [74, 75]. However, the higher intensities also result space charge effects decreasing the spatial and temporal resolution of PEEM which is of special interest at free electron lasers or synchrotrons [76] but also appear in laboratory environments [77] and can be seen with our system as well [MT-3]. Before we are going deeper into fs laser excitations for 2PPE processes at our specific setup we start with the basics of the image formation in PEEM.

3.1.1 BASICS OF PHOTOEMISSION ELECTRON MICROSCOPY

In principle only an electrostatic objective lens in combination with an imaging unit would be sufficient for the operation of a PEEM as used by Tonner and Harp [78, 79]. However, in order to magnify the image a projective lens will be needed after the objective. For a light microscope this might be sufficient and satisfying images can be acquired. In contrast, the used electromagnetic lenses in electron microscopy are more limited by aberrations compared to light lenses. Especially spherical and chromatic aberrations and axial astigmatism play a crucial role and need to be corrected. Therefore stigmators, deflectors, and several apertures are used as sketched in Figure 3.1. The drawing shows the setup of the used PEEM from Focus GmbH with electrostatic lenses, retarding field analyzer, and delay line detector (DLD) detection unit. After photoexcitation from the sample at the bottom, electrons are accelerated by the electric field of the extractor which belongs to the objective lens. If the sample shows low field emission due to a flat morphology, a typical voltage of 12 kV is applied. After the objective lens the accepted emission angles can be restricted by use of the contrast aperture decreasing spherical

aberrations. Afterwards, the electrons pass a system of two octupole stigmators/deflectors to align the optical axis and correct the axial astigmatism. The transfer lens between the stigmators is needed to magnify imaging in k-space mode. By use of the iris aperture the origin of photoelectrons can be restricted to a certain spatial region which is particularly beneficial in k-space mode. The setup is followed by two projective lenses and a drift tube which is needed to disperse the electrons depending on their kinetic energy to use the time of flight (ToF) information obtained by the removable DLD for conversion to energy scale with a typical resolution of 100 meV. As an alternative to the DLD a system of multi channel plate (MCP), a YAG fluorescence screen, and CCD camera can be used for imaging. A retarding field analyzer can be operated as a high pass filter to obtain the electrons' kinetic energies. Hence, PEEM can be seen as photoemission spectroscopy (PES) with the benefit of spatial mapping. In our case, the typical lateral resolution of the used instrument is 60 nm and the field of view (FoV) can be selected between 2.5 µm and 1800 µm.

The contrast in PEEM images can have many origins depending on the explicit photoemission process. Typical origins are a spatially variating work function of the sample, different local (near-)field intensities (see Chapter 4), topographic contrast at edges etc., and different excitation pathways in the system, e. g. different energetic configuration or lifetimes of involved states of organic molecules (see Chapter 5 and 6) [80].

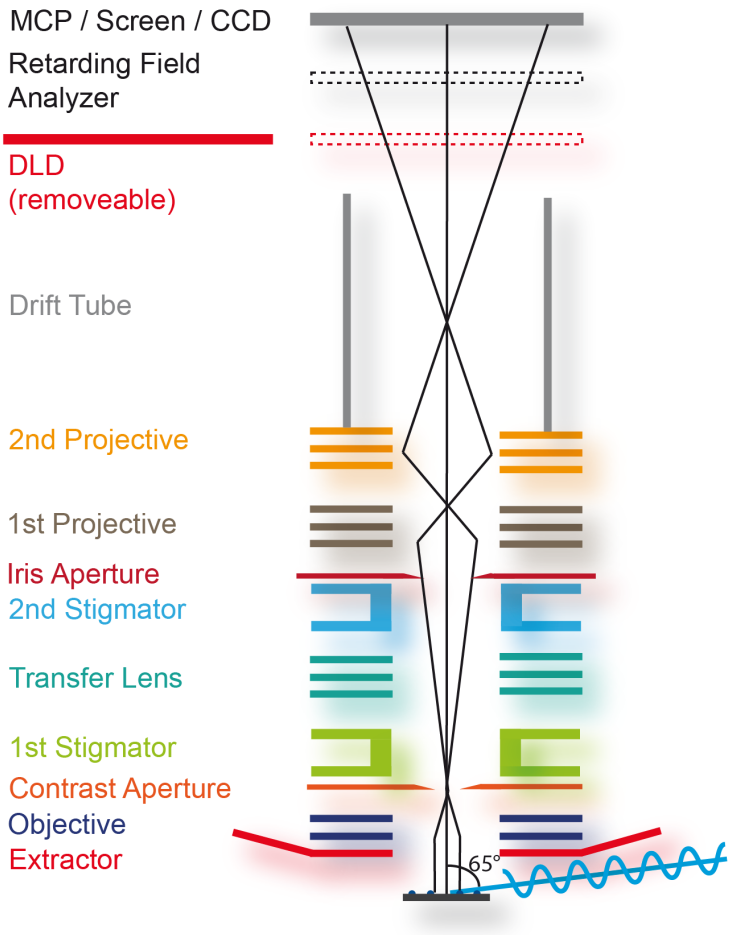

Figure 3.1: Schematic representation of the electron optics of the ToF-PEEM. Figure adapted from [69].

3.1.2 UHV PEEM SYSTEM

The PEEM is integrated in an ultra high vacuum (UHV) setup as shown in Figure 3.2. The main chamber has a base pressure of $1 \cdot 10^{-10}$ mbar and is pumped by an ion getter, a turbomolecular and a titanium sublimation pump. A residual gas analyzer (e-Vision 2, MKS) is used for inspection. For surface characterization the chamber is equipped with a low energy electron diffraction (LEED) instrument. Sample preparation can be done by use of the manipulator enabling direct current heating, a sputter gun or a resistive evaporator. Sample transfer is realized using a load lock at a base pressure of $5 \cdot 10^{-8}$ mbar. The system is directly connected to the magnetron sputtering cluster source which will be described in Section 3.2.2.

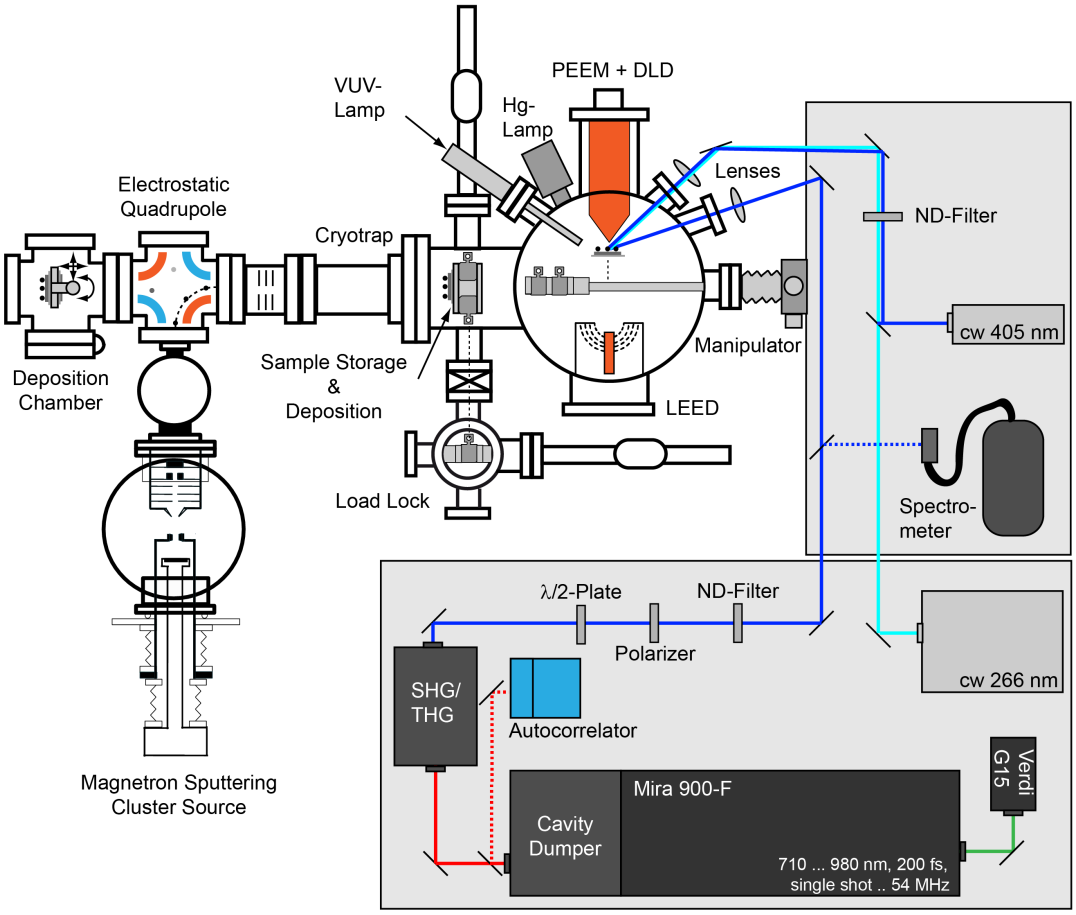

Figure 3.2: Schematic representation of the PEEM setup with cluster deposition source and laser setup. Figure adapted from [69].

3.1.3 EXCITATION SOURCES

For photoexcitation several photon sources are available which can illuminate the sample under 65° to the surface normal. A mercury lamp ($\hbar\omega = 4.9\,\text{eV}$) and a VUV-lamp (HIS-13, Focus) are directly attached to the main chamber. The VUV-lamp can be used with several rare gases as e. g. He I with an emission at 21.2 eV enabling the acquisition of ultraviolet photoelectron spectroscopy (UPS) spectra using the retarding field analyzer. Both sources emit continuous randomly polarized light. Further photon sources are installed on two optical tables next to the device and can be coupled in through calcium fluoride vacuum windows. For this work linear polarized continuous wave (cw) lasers at wavelength of 405 nm (Stradus 405-100, Vortran, max. 100 mW) and 266 nm (CryLas, max. 12 mW) were used. For pulsed illumination a Ti:Sa laser (Mira 900-F, Coherent) with a pulse length of $\approx 200\,\text{fs}$ and $\approx 20\,\text{nJ}$ pulse energy is used in combination with a cavity dumper (pulse-switch, APE) allowing a variable repetition rate between single shot and 54 MHz. The laser is optically pumped by a cw laser with 532 nm wavelength (Verdi-15, Coherent, max. 15 W). To access wavelength dependent sample properties as plasmon resonances (see Chapter 4) the wavelength of the laser must be varied. The fundamental laser light can be tuned between 710 nm and 980 nm. By creating the second harmonic by frequency doubling in a BBO crystal (HarmoniXX, APE) a wavelength range between 355 nm and 490 nm can be used. By frequency mixing the third harmonic can be generated enabling one photon photoemission at most samples between 237 nm and 327 nm. The wavelengths are monitored with a fiber coupled spectrometer (USB4000, OceanOptics) and the polarization of all lasers is adjusted using a $\lambda/2$-plate together with a linear polarizing grid. The laser power is varied using neutral density filters and is measured directly in front of the entrance window with a power meter (PD300, Ophir).

3.1.4 TWO PHOTON PHOTOEMISSION

In 1961 Kaiser and Garrett first reported a two photon absorption process [81]. The first theoretical explanation for a 2PPE process was given by Bloch in 1964 [82]. In 1980 the first two-photon photoelectron PEEM was done by Jones et al. [83, 84]. 2PPE combines the benefits of PES and inverse PES as it is also sensitive to unoccupied intermediate and final states and has a high energetic resolution [85]. To differentiate between signals from occupied states which are emitted by a virtual intermediate state and signals from real intermediate states (resonant 2PPE) it is possible to analyze the shift of kinetic energy when changing the excitation photon energy as sketched in Figure 3.3. For a real intermediate state the shift corresponds to the change in photon energy $\hbar\Delta\omega$ while for a virtual state it is $2\hbar\Delta\omega$. These energetic studies can be done with a single laser pulse, as two photons are absorbed from the same pulse within the lifetime of the intermediate state. To access the lifetime of the intermediate state a second pulse is used in a pump probe setup. In Chapter 4 we will study the plasmon resonance of silver nanoparticles which can be seen as the intermediate state in photoemission. Hence, in principle the lifetime can be accessed via time resolved 2PPE [50]. However, due to experimental reasons we decided to access the lifetime by the spectral width off the resonance as described in Section 2.1.3.

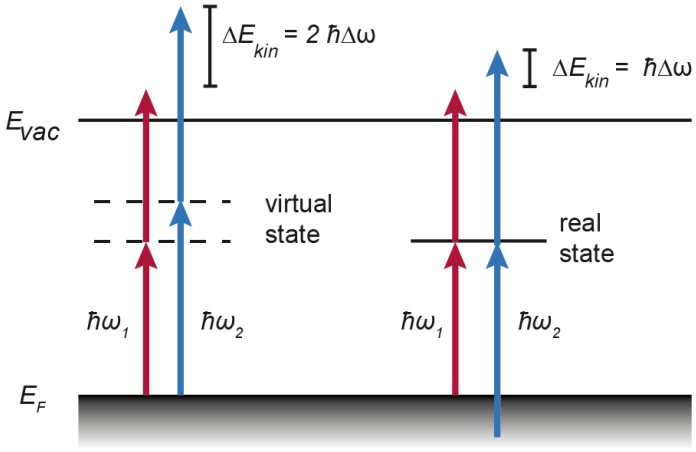

Figure 3.3: Schematic representation of the 2PPE process for two different photon energies with a virtual intermediate state (left) and a real intermediate state (right), respectively. Figure adapted from [69].

3.2 SAMPLE PREPARATION

In this section the key techniques of sample preparation for this work are described. An overview of the analyzed samples can be found in the Appendix A.1. All PEEM samples with natively oxidized silicon were mounted on a standard Focus PEEM sample holder while Si(111)-(7x7) substrates are mounted onto home-built sample holders enabling direct current heating. Since the sample is a part of the lens system in the PEEM it is crucial to have the wafer aligned parallel to the holder which is given by directly contacting it to the standard frame. For the home-built holder this was achieved by a height adjustable setup which was aligned using the reflection of a laser beam in approximately 5 m distance and comparing it to the reflection spot of a reference plane.

3.2.1 Si(111)-(7x7)

After mounting the sample onto the holder and having transferred it into the PEEM main chamber the samples were degassed at 650 °C for several hours or overnight to desorb water molecules or weakly bond adsorbates. After degassing, the samples were repeatedly flashed at 1230 °C to desorb the oxide layer. The temperature was monitored using a pyrometer with an emission-coefficient set to 0.38.

3.2.2 CLUSTER PRODUCTION AND DEPOSITION

Clusters were produced in a magnetron sputtering source of Haberland type (NC200U, Oxford Applied Research) which is described in detail in [86]. Figure 3.4 shows the experimental setup. After sputtering the target material with ≈ 50 W in a dc magnetron, clusters are formed in an argon and helium atmosphere of typically a few mbar and expand through a nozzle into the source chamber at a pressure of ≈ 10^{-4} mbar. For cluster beam formation a conical skimmer and a system of ion optics is used. After passing the ion optics chamber clusters are size selected by the electrostatic quadrupole. Assuming the same charge and velocity for all clusters, their mass can be selected by the quadrupole voltage. Nanoparticles having passed the mass selection enter either a

deposition chamber or are reflected towards the PEEM main chamber. To increase the cluster flux and collimate the beam an ion optics can be used in the differential pumping chamber. To ensure clean vacuum conditions during deposition into the PEEM chamber a cryotrap is used before entrance being at a base pressure $< 10^{-9}$ mbar. Clusterflux can be continuously monitored via several grids in the clusterbeam. Additionally, a Faraday cup can be used in the deposition chamber, here the clusters have opposite charge than the ones getting deposited into the PEEM. During this work, always negatively charged nanoparticles were used since the flux is approximately five times higher. For deposition the sample is placed in the PEEM main chamber behind the entrance valve which is sealed with a copper gasket having just a central opening with a diameter of 12 mm. By opening the valve manually clusters were deposited. The deposition time was estimated to fit the desired coverage at the measured cluster flux. With the used setup it is possible to deposit clusters under clean and controlled conditions. Compared to chemically prepared particles in a solution, the nanoparticles just consist of the target material and are free of ligands or other components.

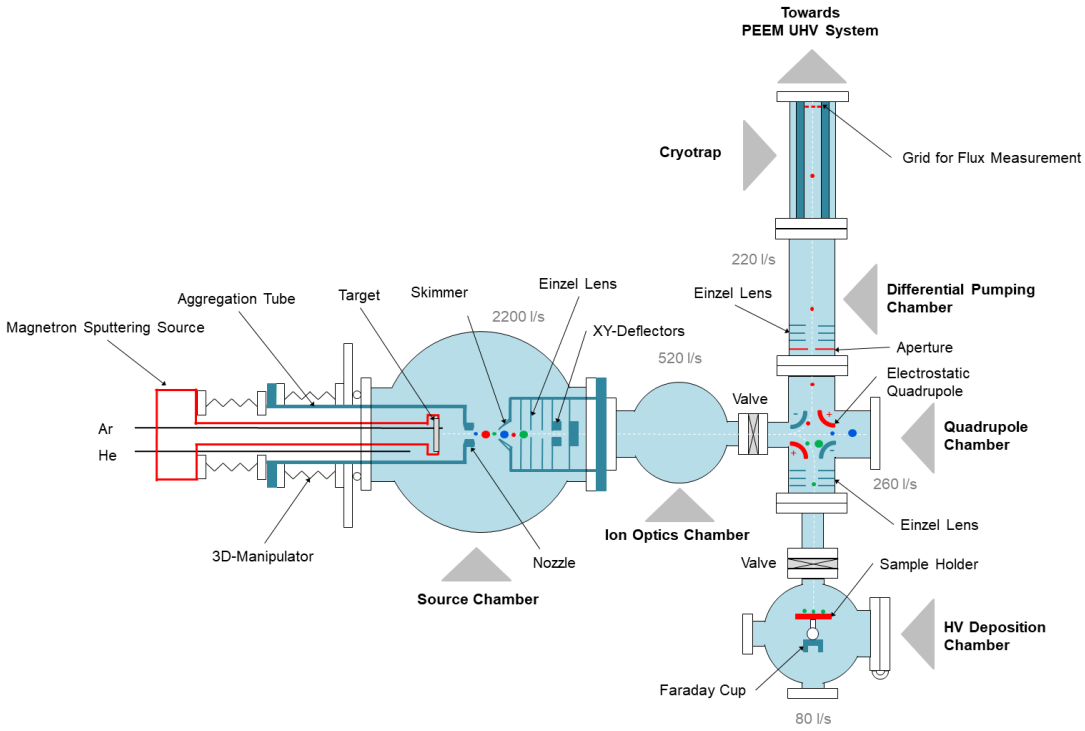

Figure 3.4: Schematic drawing of the experimental cluster source setup with electrostatic quadrupole for size selection. Figure adapted from [86].

3.2.3 MOLECULAR EVAPORATOR

Molecules were evaporated in a home-built thermal evaporator. The setup was built and characterized in the framework of the master's thesis by Bahaaeddin Irziqat [MT-1]. Tetracene powder (Sigma-Aldrich, 98 % purity) was thermally heated to 135°C in a test tube connected via a cf-flange to a vacuum chamber with a base pressure of $\approx 5 \cdot 10^{-8}$ mbar. The sample was orientated in line with the opening of the tube being separated by a gate valve. Deposition can be continuously monitored via a quartz crystal micro balance [MT-1]. Deposition time was 25 min.

4 OPTICAL AND ELECTRONIC PROPERTIES OF SUPPORTED SILVER NANOPARTICLES

For utilizing single metallic nanoparticles as local near-field excitation sources a detailed knowledge of their optical properties is of fundamental importance. While nanoparticles are well studied in ensemble measurements [6–8], experimental data on single metallic clusters in a size range below 20 nm can rarely be found in literature. For addressing individual clusters this knowledge is crucial. Hence, the optical and electronic properties of individual supported silver nanoparticles are studied in this chapter. To access cluster surface interactions as well as the dependence on the actual cluster size, three samples were prepared with different characteristics. An overview of the samples can be found in the Appendix A.1. For Sample A a broad size distribution of silver nanoparticles between 10 and 35 nm were soft landed on a piece of a Si(111) wafer with native oxide layer (n-type (As), $< 0.01\,\Omega$cm, CrysTec GmbH) by ramping the voltage of the electrostatic quadrupole (see Section 3.2.2 for details) from 0.1 to 1 kV during deposition at a gas flux of around 52 sccm argon and 6 sccm helium. A particle density of $\approx 2\,\mu m^{-2}$ was chosen (deposition time: ≈ 20 s). In order to elucidate the role of the substrate atomically flat Si(111)-(7x7) was used for the Samples B and C (for details of preparation see section 3.2). On Sample B a constant quadrupole voltage of 1.5 kV was used at a gas flux of around 57 sccm argon and 3 sccm helium to achieve a narrow size distribution around 11 nm diameter. The particle density was $\approx 0.3\,\mu m^{-2}$ in this case. For Sample C the quadrupole voltage was changed to 4 kV yielding an average diameter of ≈ 25 nm at a comparable particle density as Sample B.

The first section deals with the plasmonic properties where especially the impact of the underlying substrate is investigated. In the second part we will focus on the distributions of the photoelectrons' kinetic energies while the possibility to analyze momenta and associated emission angles is presented in the third section.

4.1 PLASMONIC PROPERTIES AND CLUSTER SURFACE INTERACTION

While for ensemble studies it is possible to investigate plasmonic resonances down to clusters consisting of less than 10 atoms [87], single-object spectroscopy of optically excited plasmon resonances in nanoparticles of sizes below 20 nm diameter is highly demanding in terms of sensitivity. Different methods have been employed including near-field microscopy [53], photothermal microscopy [88], spatial modulation spectroscopy [89, 90], and EELS [17, 91] for the case of electron-excited plasmons, see [92, 93] for reviews. Optical Mie scattering intensities decrease to the sixth power of particle size, compromising spectroscopy of small particles. On the contrary, the absorbed intensity only scales with the third power, but for technical reasons (e.g. background light) optical absorption detection of individual nanoparticles is hard to achieve. Absorbance is the relevant property for plasmonic systems coupled to electronic devices such as plasmon-enhanced solar cells, whereas scattering is more relevant for optical sensor applications. Here we focus on optically excited plasmons in order to keep the mechanism as close as possible to the situation for plasmonic applications. Photoelectron spectroscopy has been shown to be a versatile tool for accessing various properties of supported nanoparticles [94, 95]. To address the near fields of individual small nanoparticles photoelectron detection was employed in a PEEM. The total electron yield is a measure for the local near-field intensity [96–98] which in turn reflects the particle absorbance. By sweeping

the wavelength of the monochromatic incident light one obtains excitation spectra with high spatial resolution. The role of the environment is revealed by comparing plasmon spectra of particles on silicon with a native oxide layer (typically $1-2\,\mathrm{nm}$ thick) to those on clean Si(111)-(7x7). This section will roughly follow [KO-4] where the majority of the results has been published.

4.1.1 PLASMONIC RESONANCE CURVES

As a first step we start by investigating Sample A with a native oxide layer, in the following referred to as "oxidized silicon", and a broad size distribution of silver nanoparticles. Figure 4.1a shows a total electron yield PEEM CCD-image under illumination with a mercury lamp (photon energy $\approx 4.9\,\mathrm{eV}$). The image shows bright spots with comparable intensities, each corresponding to an individual silver nanoparticle. Since the illumination does not coincide with plasmonic resonances the electron intensity is tentatively scaling according to the particle's volume (for small clusters) or to the exposed surface (for larger particles) (cf. [99, 100]), apart from possible variations due to different work functions. In some rare cases nanoparticles are located in close vicinity to each other and cannot be resolved individually in this image.

The same area but now under 410 nm fs-laser illumination is shown in Figure 4.1b. Compared to Figure 4.1a a highly varying intensity is observed, such that many of the particles are hardly visible. In earlier experiments such variability has been attributed to a resonant, plasmon-assisted 2PPE process [96, 97, 99, 101–103]. In the inset of Figure 4.1 the laser power dependence of the total electron yield with 410 nm fs-laser excitation is shown on a double logarithmic scale. The linear fit shows a slope of ≈ 2.3 indicating 2PPE processes prevailing (for details on the analysis see Appendix A.3). Each particle exhibits a slightly different plasmon resonance energy and depending on whether the respective resonance is matched by the laser light excitation the electron yield varies by orders of magnitude.

To determine the plasmonic properties of each nanoparticle the excitation energy is now varied while keeping all other laser parameters as constant as possible (e. g. cw intensity $= 6\,\mathrm{mW}$, $f_{\mathrm{rep}} = 1.09\,\mathrm{MHz}$, p-polarization, spot position, focus size $\approx 200 \times 100\,\mu\mathrm{m}^2$) and PEEM CCD-images[1] are acquired for each photon energy (for details on data processing see Appendix A.2). The pulse duration was about 200 fs which is assumed to vary little during a scan. Exemplarily, the photoelectron yields for some selected particles are plotted versus the excitation photon energy in Figure 4.2 (dots). The graph shows a strong dependence of the photoelectron yield on the incoming photon energy with a pronounced maximum. Signatures of different nanoparticles are varying in energy position, width, and intensity. We attribute the presence of the peak to the resonant excitation of the LSPR of each individual particle [96, 97, 103–106]. The curves are shown together with least-square fits to a squared Lorentzian which accounts for the second-order nature of the 2PPE process [96–98]. In the following the peak locations and widths are being addressed.

1 The CCD camera was used here because the DLD's MCP showed some artifacts and was replaced later.

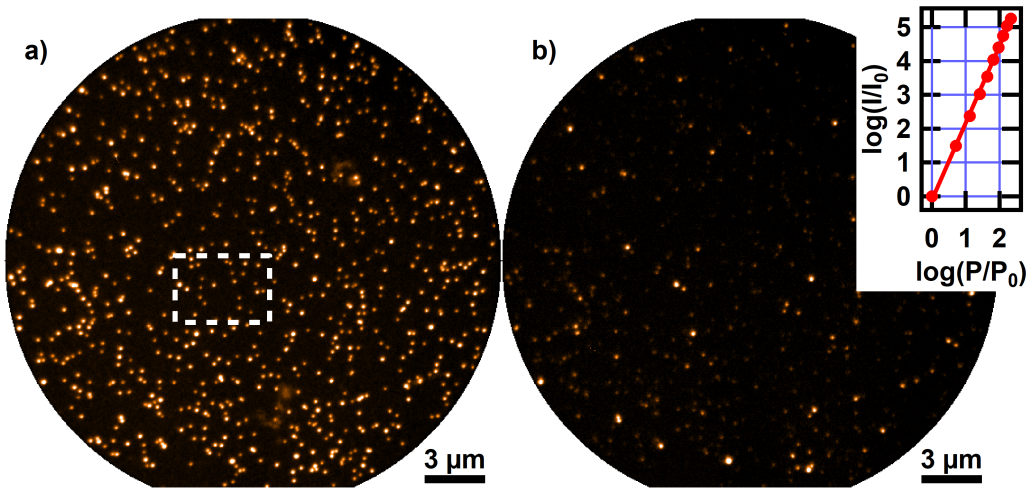

Figure 4.1: PEEM images (field of view: 25 µm) showing the total electron yield of silver nanoparticles (height: 10 to 35 nm) on silicon with a native oxide layer. Brighter colors correspond to a higher electron yield. a) For mercury lamp illumination essentially all particles are visible as bright spots. An AFM image of the marked area is shown in Figure 4.6a. b) 2PPE total electron yield PEEM image of the same sample location for 410 nm fs laser illumination. Here the contrast is governed by the individual plasmonic properties of each nanoparticle. Inset: Double logarithmic plot (slope: 2.3) of total electron yield I/I_0 vs. laser power P/P_0 demonstrating that 2PPE is the dominant process. Figure adapted from [KO-4].

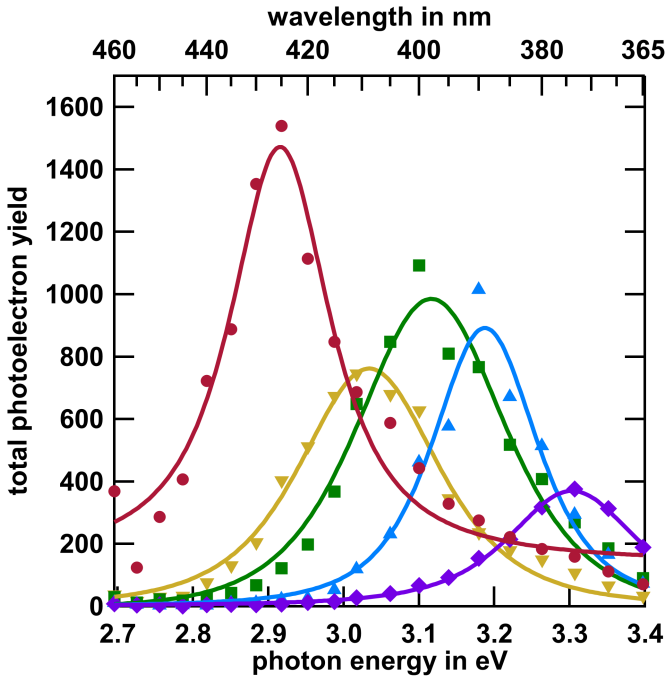

Figure 4.2: Total electron yield (dots) of selected individual silver nanoparticles on oxidized silicon as a function of excitation photon energy. The spectra show the plasmonic response of single nanoparticles and are fitted (solid lines) by squared Lorentzians. Figure adapted from [KO-4].

4.1.2 MAPPING PLASMON RESONANCES AND DEPHASING TIMES

As expected from the intensity variation (Figure 4.1b) the resonance peak position strongly depends on the particular particle under investigation. For a more systematic study the resonance energies are now extracted for each pixel of the acquired PEEM images. The resulting energy map is shown in Figure 4.3a where the colors indicate the resonance position obtained by the fit. Pixels belonging to the same particle occur in the same color while different particles exhibit various colors. Most nanoparticles show a resonance between 3.1 eV and 3.3 eV (green to blue colors), while energies above 3.3 eV (purple) or below 3.0 eV (red) are less frequently observed. The apparent lateral size of each particle does not reflect the actual geometry but rather is a direct consequence of chosen intensity threshold (see Appendix A.2).

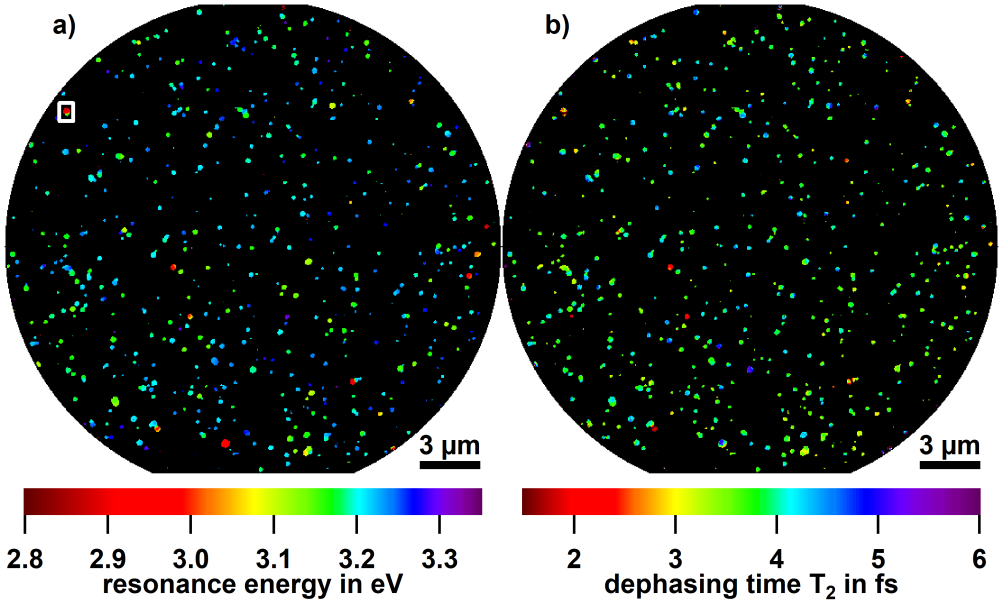

Figure 4.3: a) Plasmon resonance map of silver nanoparticles on oxidized silicon. The map shows the central energy of the spectral fit for each pixel as exemplarily shown in Figure 4.2. The marked area is shown in detail in Figure 4.4b b) Map of the dephasing time T_2 as calculated from the FWHM of the pixel-wise fit. Figure adapted from [KO-4].

Compared to an ordinary PEEM image the additional information on the spectral properties has an interesting implication: in some cases the lateral distance between two particles is less than the spatial resolution so that they appear as a single spot in the raw PEEM images (Figure 4.4a). However, due to their different spectral response they can be clearly distinguished (Figure 4.4b) as also verified by AFM measurements (not shown). The typical spatial FWHM of the particle signature is around 160 nm, reflecting the instrumental resolution at these specific measurement conditions. Due to different spectral properties it is possible to distinguish nearby nanoparticles even if their separation is less than the native resolution, which is referred to as super-resolution, e. g. in the field of fluorescence imaging [107, 108]. A necessary condition is that the separation is sufficiently large to avoid plasmonic coupling. In this case the averaged resonance curve obtained by the wavelength scan (electron yield vs. excitation energy) can be fitted by a sum of two squared Lorentzians in order to separate the two resonances. The corresponding intensity "deconvoluted" maps are shown in Figure 4.4c-d. They are

obtained by keeping the resonance energy, width, and offset fixed so that the only fitting parameters are the two peak heights. Each map now reflects the separated signal of one of the two nanoparticles. The center of each particle can be determined with an accuracy (i. e. one standard deviation) of 4.4 nm for Figure 4.4c and 3.2 nm for 4.4d, respectively. Hence, a particle distance of 105 nm $\pm$ 8 nm is obtained. From the correlated AFM image (see Section 4.1.3) a distance of 84 nm $\pm$ 9 nm is inferred. Remaining deviations may be due to AFM tip or feedback artifacts, or due to systematic errors of the spectral "deconvolution" or of determination of the center location. Concluding, it could be shown that the distance between two nanoparticles can be determined based on their plasmonic properties with an accuracy $\approx$ 20 times beyond the native instrumental resolution.

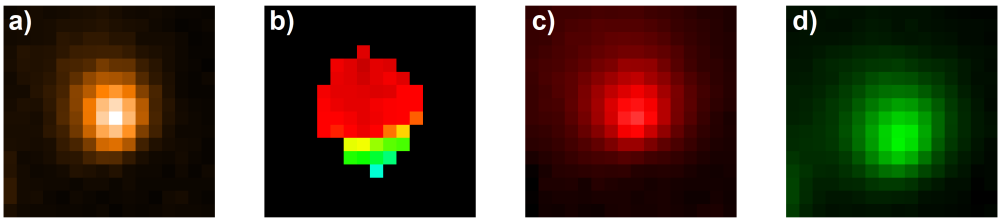

Figure 4.4: Detailed analysis of the locations of two nearby nanoparticles (marked area of Figure 4.3a). a) Total electron yield PEEM image obtained under mercury lamp excitation. b) Plasmon resonance map of the same area under femtosecond laser excitation, revealing two separate particles. c-d) Fitted intensity of each of the two plasmonic resonances in the same region, yielding the lateral interparticle distance. Figure from [KO-4].

Under the assumption that the linear response of a nanoparticle corresponds to the square root of the 2PPE intensity the width of each Lorentzian spectrum Γ is directly connected to the dephasing time T_2 of the plasmon via $T_2 \cdot \Gamma = 2\hbar$ [51, 109] (see Section 2.1.3). The value of Γ is hardly affected by the experimental energy resolution, because the latter is only determined by the laser linewidth which is estimated to be $\approx$ 15 meV. Moreover, it contributes equally to each data point leading to a statistical error significantly below this value. Due to the single-object approach inhomogeneous broadening is not present either. It can be concluded that the observed spectra correctly reflect the intrinsic width of each individual silver nanoparticle under optical excitation. On average the FWHM amounts to $\Gamma \approx 360$ meV which corresponds to $T_2 \approx 3.7$ fs.

Like in the case of the resonance energies also lifetimes can be analyzed pixel-wise, yielding a spatially resolved lifetime map of T_2 (Figure 4.3b). Here the question whether the variation of the relative permittivity in vicinity of the particles is connected to a corresponding change of the dissipative channels (damping) is addressed. To this end dephasing times and resonance energies are correlated as shown in Figure 4.5a. Each dot represents one particle. A significant correlation is not obvious, indicating independent mechanisms for energy shift and damping. From the excitation spectra the plasmonic quality factor $Q = E_{\mathrm{res}}/\Gamma$, describing the local field enhancement [52, 53, 110] (see Section 2.1.4), can be extracted within a simple Lorentzian model. In Figure 4.5b the resulting distribution for the same particles as in Figure 4.5a is shown together with the best Gaussian fit, yielding $\langle Q \rangle = 9.0$ with a standard deviation of ± 1. The variation of Q factors is primarily attributed to heterogeneities in the close surrounding of the particles, resulting in differences in the available de-excitation pathways at the interfaces.

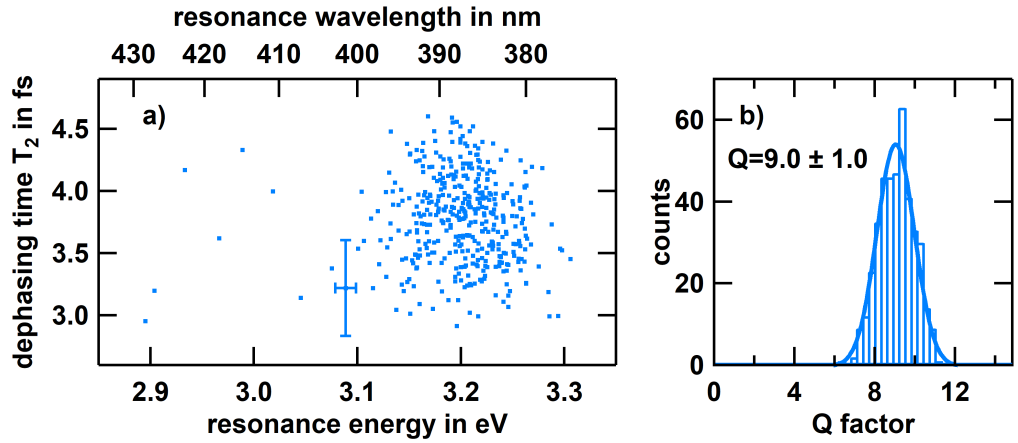

Figure 4.5: a) Deduced dephasing time versus plasmon resonance energy for a large number of individual silver nanoparticles (blue dots) on oxidized silicon obtained by PEEM. The estimated typical experimental uncertainty along both directions is exemplarily indicated for one particle. b) Resulting distribution of the quality factor Q for the clusters shown in a), together with a Gaussian fit (blue line). Figure adapted from [KO-4].

4.1.3 CORRELATION WITH CLUSTER HEIGHTS

In the following the correlation of plasmon resonance energies with their sizes are addressed, since a part of their variation should just stem from the size distribution on the sample. To gain information about the height of the silver nanoparticles a correlative AFM measurement is conducted under ambient conditions subsequent to the PEEM study, see Figure 4.6a. High-angle annular dark-field scanning transmission electron microscopy (HAADF-STEM) images from a separate deposition indicate that the nanoparticles exhibit mini-facets but are approximately of spherical shape, see Figure 4.6b for a typical example. From previous investigations the aspect ratio is known to be close to unity [111], which is compatible with this combined AFM/TEM study.

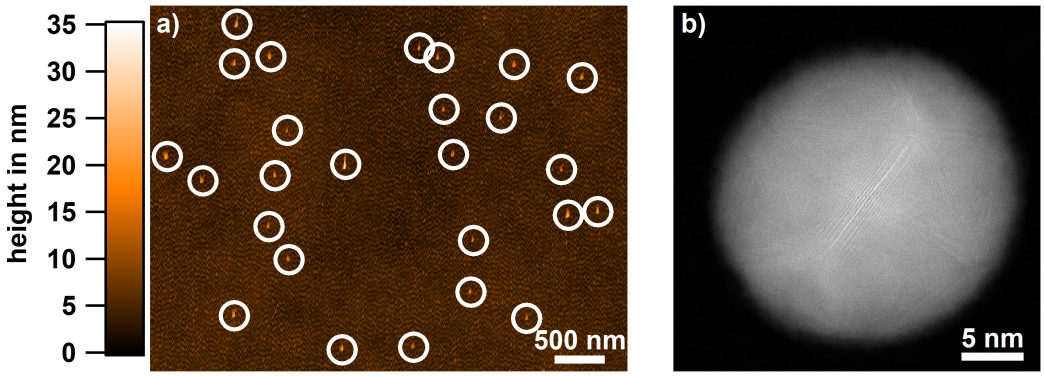

Figure 4.6: a) Part of an AFM image showing the marked area of Figure 4.1a. The white circles mark the position of the silver nanoparticles as a guide to the eye. b) HAADF-STEM image of a representative silver nanoparticle deposited under similar deposition conditions onto a TEM grid. The cluster shows facets forming a nearly spherical geometry. Figure from [KO-4].

Using information obtained from AFM the plasmonic properties can now be correlated with the geometry. In Figure 4.7 the plasmon resonance energy is plotted versus the height for 412 individual particles. Around 5% of all particles were rejected due to obvious failure of the fit (see Appendix A.2 for details). A direct application of Mie's theory requires a homogeneous environment which is not the case for particles on a substrate. One approach is to apply a correction by assuming an effective dielectric constant which is chosen in between substrate ($\varepsilon = 2.16$, fused silica (SiO_2) for 400 nm wavelength [112]) and vacuum ($\varepsilon = 1$) values [29, 40]. Corresponding Mie trends are plotted as dashed lines for different effective dielectric constants of the environment. Apart from a weak global trend in accordance to the Mie calculations for $\varepsilon_{\text{eff}} = 1.85$ the particle data show pronounced scattering of the order of ± 0.05 eV around the trend curve. This implies that the particle size is not the dominating reason for the precise eigenenergy of each LSPR, despite its known and intuitive effect. The origin of this interparticle scattering is addressed in the discussion below. For larger particles there appear to be some outliers having a clearly red-shifted resonance, most likely caused by particle oligomers, being neither resolvable by AFM nor PEEM measurements. This is supported by the off-resonant PEEM image (illumination by mercury lamp, see Figure 4.1a) which shows unusually high intensities for most of these cases, indicating the presence of large particles or agglomerates. Moreover, the majority exhibit a second peak in the excitation energy spectra, or at least a weak shoulder which would be expected for such structures.

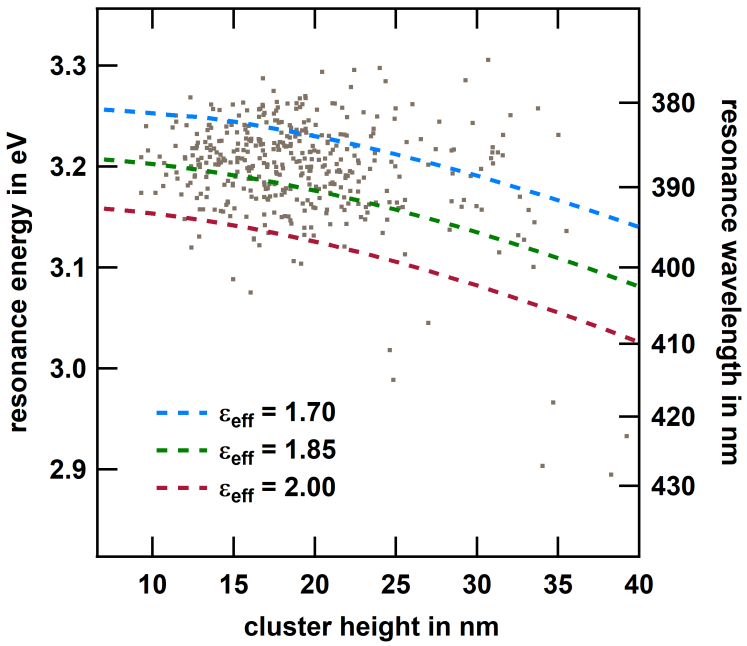

Figure 4.7: Correlative plot of the resonance energy of individual silver nanoparticles (dots) on oxidized silicon versus their geometric height. The dashed lines are calculations from Mie theory for spherical particles with diameters corresponding to the measured height, embedded in an effective medium using three different dielectric constants. Figure adapted from [KO-4].

4.1.4 PLASMON RESONANCE SPLITTING ON SI(111)-(7X7)

In order to elucidate the role of the substrate the results are now compared to those obtained from Sample B where small particles on atomically flat Si(111)-(7x7) were deposited. This time only a narrow size distribution was selected during deposition in order to avoid the necessity of elaborate correlative AFM measurements.

A height histogram obtained from AFM measurements of the same sample but at a different location than that used for PEEM is shown in Figure 4.8a, yielding an average height of approximately 11 nm. In this size range the dependence of the resonance position on the particle height (corresponding to the diameter in Mie calculations) is weak, see slope of dashed lines in Figure 4.7. Due to the higher relative permittivity of pristine silicon ($\varepsilon \approx 30$ for 400 nm wavelength [113]), Mie theory would predict a red shift of more than 100 nm of the plasmon resonance. A representative excitation spectrum is shown in Figure 4.8b. Instead of exhibiting a single peak, the resonance splits into two peaks with a separation of approximately 0.5 eV, typical of the majority of the particles. The ratio of the intensities of both modes varies from particle to particle.

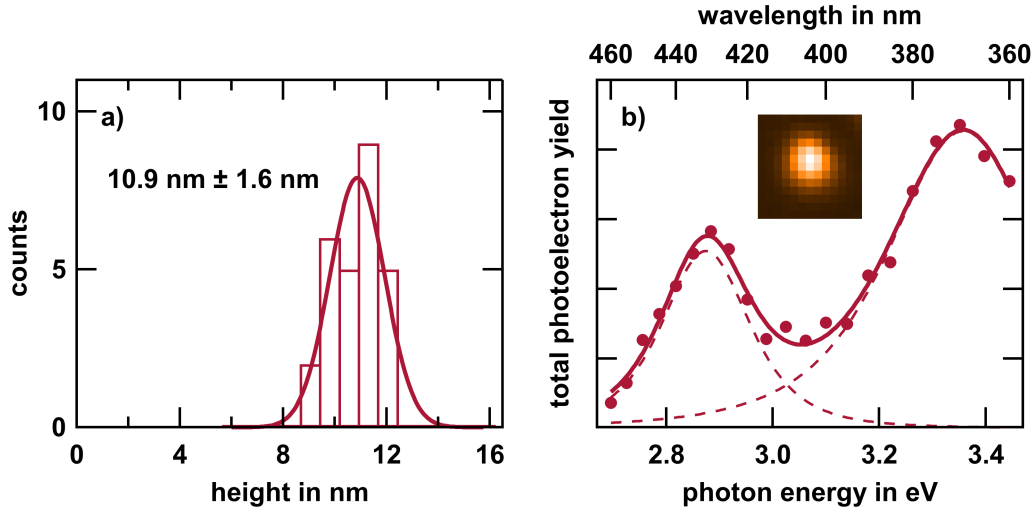

Figure 4.8: a) Histogram (bars) of the height distribution of silver nanoparticles deposited on Si(111)-(7x7) as observed by AFM, together with a Gaussian fit (solid line). b) Representative optical excitation spectrum (dots) of a single silver nanoparticle deposited on Si(111)-(7x7). The spectrum was fitted by a superposition (solid curve) of two squared Lorentzians (dashed curves). The inset shows the total electron yield PEEM image averaged over all excitation wavelengths shown in the spectrum. Figure adapted from [KO-4].

For further studying the role of the particle size, Sample C with larger particles on Si(111)-(7x7) is investigated. For the above mentioned reasons a narrow size distribution was selected as well, the lateral diameter of the particles was determined by HAADF-STEM images from a parallel deposition onto a TEM grid. The resulting distribution is shown in Figure 4.9a while an excitation spectrum is exemplarily shown in Figure 4.9b. Compared to the spectrum shown in Figure 4.8b (small particles on Si(111)-(7x7)) a third peak arises. Peak positions and intensities are strongly sensible to the specific particle under investigation.

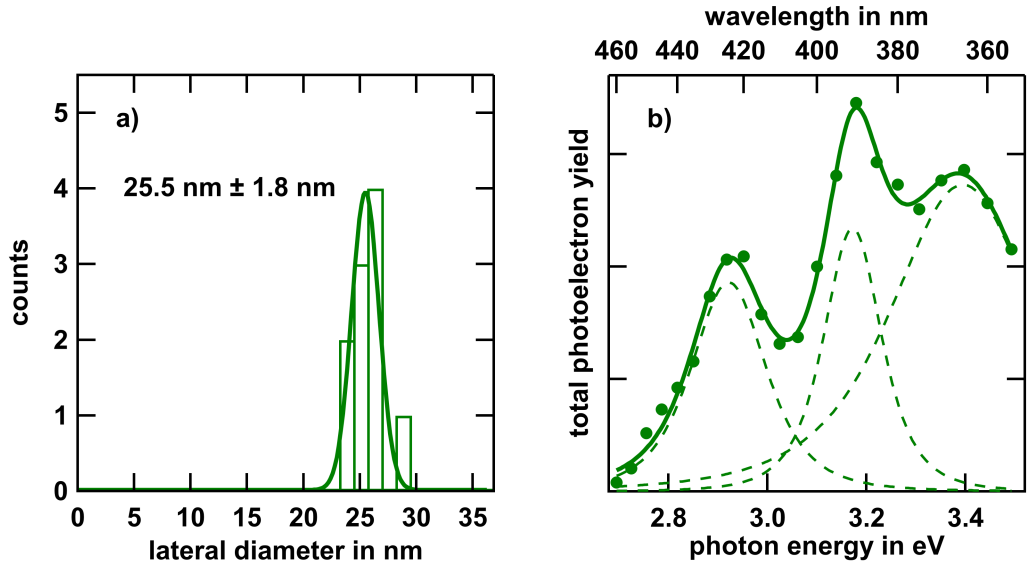

Figure 4.9: a) Histogram (bars) of the diameter distribution of silver nanoparticles deposited on Si(111)-(7x7) as observed by HAADF-STEM, together with a Gaussian fit (solid line). b) Exemplary spectrum (dots) of a single silver nanoparticle deposited on Si(111)-(7x7). The spectrum was fitted by a superposition (solid curve) of three squared Lorentzians (dashed curves).

4.1.5 DISCUSSION

In this part different observations are interpreted and discussed with respect to literature.

Image Dipoles

A peculiar property of silicon is its large dielectric constant for the relevant wavelength range [113]. Consequently, one could expect the formation of image dipoles in the material close to the surface which can couple to the excited particle plasmon, thus resulting in the observed mode splitting (Figure 4.8b). This effect is closely related to that observed in the case of two nearby particles (dimers) with interacting dipole moments. Furthermore, higher order multipoles can be excited due to strong field inhomogeneities. Such behavior has been predicted by theories beyond Mie [34, 44, 114–116] and experimentally observed for large ($>$ 100 nm diameter) colloidal particles [117]. Earlier calculations have shown a crucial dependence of the extinction and therefore the absorption cross section on the angle of incidence and the polarization of the incoming light [114].

Generalized Mie Calculations

To get a deeper understanding of the cluster-surface coupling in our system calculations based on Generalized Mie theory [34] were performed by our collaboration partner Jean Lermé[2] using the actual geometry of our optical setup. The coupling between particle (10 nm and 30 nm diameter) and substrate (silicon with complex $\varepsilon(\omega)$) was varied via the effective distance d_{eff} between the center of the metal sphere and the surface of the substrate. As a consequence of the high relative permittivity of silicon the ratio of the square moduli of the irradiating field components perpendicular and parallel to the surface is of the order of 30. Hence we are only sensitive to vertical excitations since the 2PPE signal exhibits a square dependence on this ratio. In addition, the absorption cross sections of the perpendicular modes are two orders of magnitude larger than for the parallel one (for details see Appendix A.4).

2 University of Lyon, Institut Lumière Matière, 39622 Villeurbanne Cedex, France

The calculated absorption cross sections for 10 nm particles are shown in Figure 4.10a for different values of d_{eff}. For a larger d_{eff} the interaction of the sphere and the surface is negligible, and only the dipolar plasmon resonance can be excited. For decreasing distances the electrostatic coupling to the image dipole in the substrate increases leading to strong field inhomogeneities. As a result, the dipole mode undergoes a prominent red-shift with decreasing d_{eff} and additional higher-order multi-polar plasmon modes evolve in the spectra. This implies that the frequently employed dipole approximation falls short, although the geometry of our system is more than an order of magnitude smaller than the wavelength of the incoming light. In contrast to retardation effects which result in a break-down of the dipole approximation (i.e. quasistatic limit) in case of large particles, here the clusters themselves create higher order multipole fields due to strong coupling to the surface. Note that this mechanism resulting in the appearance of two peaks (dipole and quadrupole contributions) is fundamentally different from the frequently reported effect of mode splitting due to anisotropic particle shapes (longitudinal and transversal modes).

For comparing the measured spectra to the calculated absorption cross sections we need to account for the total number of accessible initial states as a function of photon energy. Since the density of states (DOS) of polycrystalline silver is roughly constant in this regime [119] a normalization factor $(2E_{Ph} - W)^{-1}$ was applied, where E_{Ph} is the photon energy of the incoming light and $W = 4.26\,\text{eV}$ is the work function of silver [120]. To account for the 2PPE process the square root of the normalized spectra is shown in Figure 4.10b, so that the experimental data may be directly compared to the calculation results. Up to two peaks are visible in both experimental and calculated data, where the most red-shifted one can be attributed to the dipolar surface plasmon mode. The position of this mode varies indicating differences in the local environmental coupling as expressed by the distance d_{eff} in the calculations. The results suggest that the effective spacing between particles and surface is below 2 Å which is plausible in view of the soft landing conditions. In comparison to theory the peaks appear broader which is pointing to a shorter dephasing time T_2 of the plasmon compared to the calculations, potentially induced by interface damping effects [121]. Higher order multipole modes (beyond quadrupole) are not clearly resolved separately on this sample either due to their positions outside the accessible photon energy regime or as a result of the mentioned broadening.

The calculated absorption cross sections for large particles with a diameter of 30 nm are shown in Figure 4.11a for different values of d_{eff}. Analogous to Figure 4.10 exemplary experimental spectra are shown in Figure 4.11b, using a similar normalization procedure as described above. For larger particles the peak positions undergo a red-shift leading to the presence of three clearly distinguishable peaks in the accessible photon energy regime. The spectra show a high variability in the peak intensities as well as in the peak positions. These variations are attributed to a crucial dependence on the exact local geometry, which varies more for larger particles possibly due to an increased facet size. The blue curve in Figure 4.11b shows only one prominent peak with a small shoulder on the low energetic side. This spectral signature is found to be common in the data set. Comparing with theory the peak can be assigned to the dipolar plasmon mode. In this scenario the small kink is most likely an artifact due to the smoothening procedure or due to the imaging system itself. In order to avoid the necessity of smoothening the data obtained at different wavelengths due to minor changes of the laser-pulse characteristics, the setup could be extended using the photoemission signal from a reference sample [103].

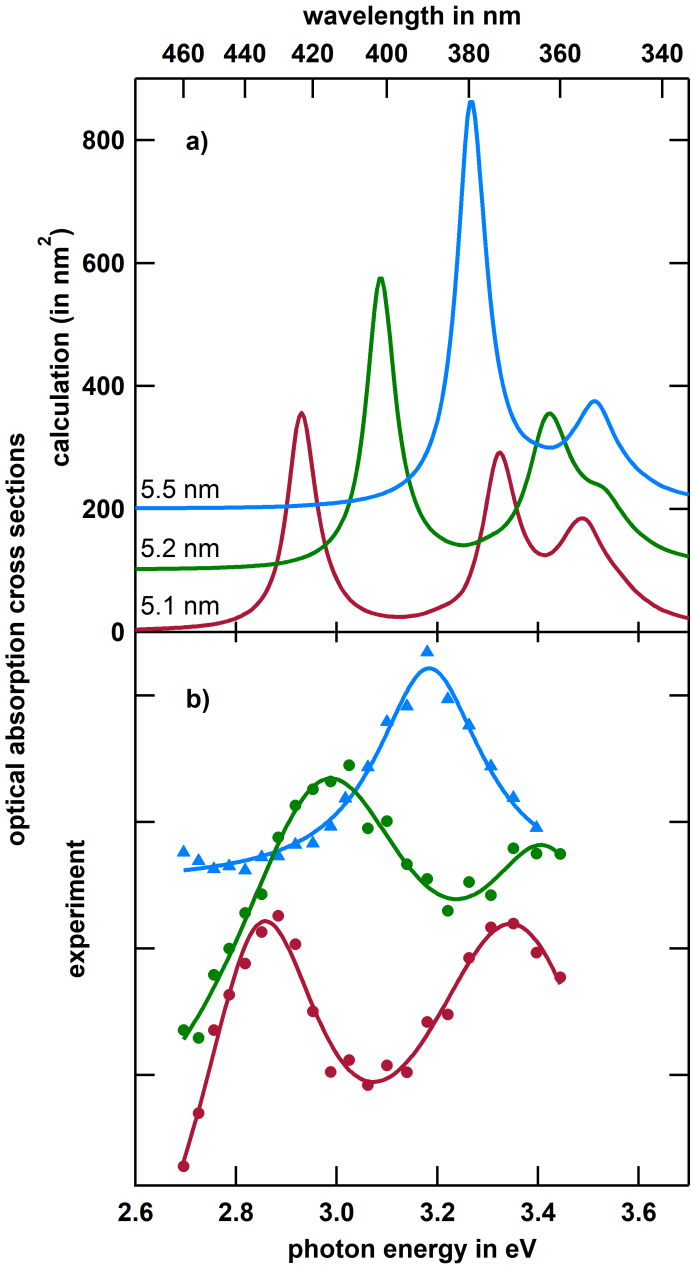

Figure 4.10: a) Calculated absorption cross sections for silver spheres of 10 nm diameter above a silicon surface for three different distances d_{eff} between substrate and the center of the sphere, ranging from 5.1 nm (red) to 5.5 nm (blue). b) Examples of experimental absorption cross sections extracted from electron yield spectra of individual supported silver nanoparticles. The lower two curves (circles) represent particles on Si(111)-(7x7), taken from the same dataset shown in Figure 4.8b. The upper blue spectrum (triangles) is taken from the oxidized sample (A) to illustrate the case of weak coupling. All curves are offset vertically for clarity. See text for details. Calculations done by Jean Lermé [118]. (According to [KO-4])

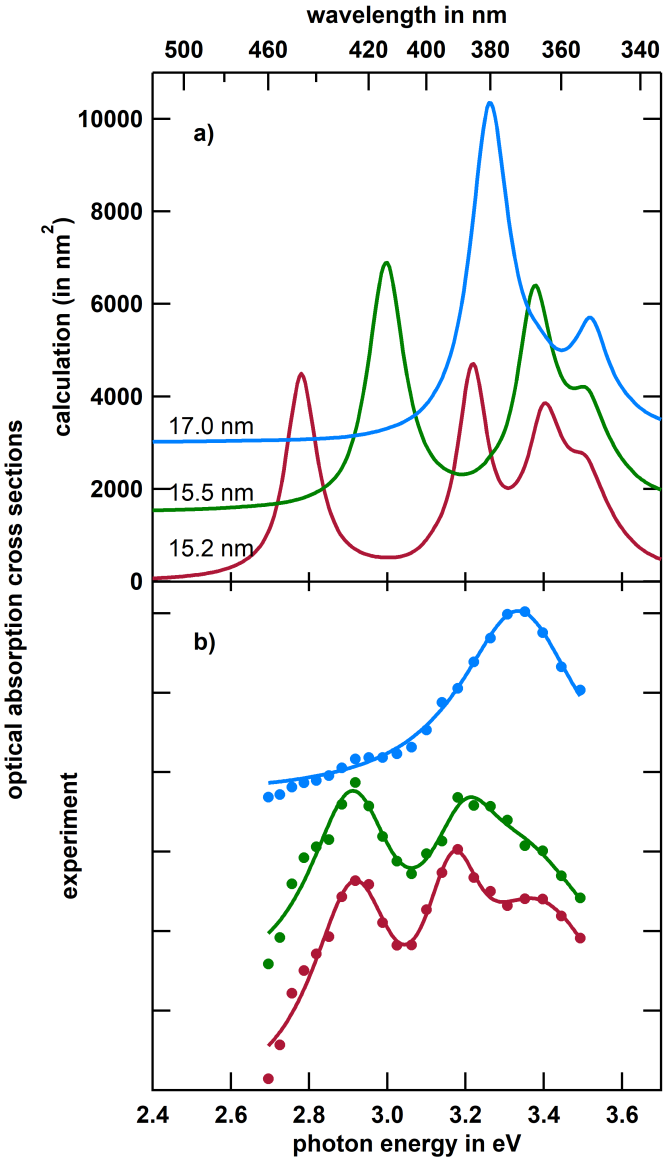

Figure 4.11: a) Calculated absorption cross sections for silver spheres of 30 nm diameter above a silicon surface for three different distances d_{eff} between substrate and the center of the sphere, ranging from 15.2 nm (red) to 17.0 nm (blue). b) Examples of experimental absorption cross sections extracted from electron yield spectra of individual silver nanoparticles on Si(111)-(7x7). The measurements are taken from the same dataset shown in Figure 4.9b. All curves are offset vertically for clarity. See text for details. Calculations done by Jean Lermé [118].

Alternative Explanations for a Multi-Peak Structure

Alternative explanations for the double-peak structure are also considered since a mode splitting in principle could be attributed to various other mechanisms which are addressed in the following.

a) Nanoparticles may change shape upon deposition on surfaces [122]. In the case of non-spherical, e.g. ellipsoidal particles, splitting of modes along the two half-axes is well known [40, 44]. As also discussed above in the context of oxidized silicon as a substrate, a splitting of $\approx 0.5\,\mathrm{eV}$ observed here implies an aspect ratio (width/height) of 2 or larger [40]. However, in view of AFM and TEM data (see also [111] for related STM data) such geometries appear highly unlikely, particularly since the particle size is known due to mass-selection in the gas phase prior to deposition. Furthermore, the vicinity of the substrate results in a suppression of the peak corresponding to the horizontal mode, see discussion below and Figure A.2: even if the particles were oblate a single peak would still be observed because the experiment is only sensitive to plasmon modes perpendicular to the surface.

b) Similar double peaks have been found for core-shell particles [29]. In this case both deposition and measurement were performed in ultra-high vacuum avoiding exposure apart from the surface itself. A possibly related structure may result from the formation of a silicide film at the particle/silicon interface or around the particle. However, considering that the deposition conditions are within the soft-landing regime [122] and in view of the miscibility gap of silver and silicon [123] we rule out a complex core-shell geometry or similar structures in this case.

c) Particle-particle interaction leads to a red shift of the resonance which is utilized for sensor applications [124]. For dimers or longer chains of particles a splitting of the plasmon mode is indeed expected [29, 40]. However, the low nanoparticle density of ≈ 0.3 particles per μm^2 renders the presence of particle oligomers highly unlikely. Furthermore, most of the particles show the same behavior which could only be possible if exactly the same multiparticle arrangement was formed for each object which we also consider unlikely. Another piece of evidence against the formation of oligomers is the absence of a strong azimuthal dependence on the excitation path which was checked by using illuminating from a different direction which is rotated by 60° around the surface normal. Finally, a similar argument as mentioned in a) is valid here: for lateral dimers a single peak corresponding to the in-phase transversal mode would be actually expected. Note that for such small particles the transversal out-of-phase mode can not be excited [29, 40].

It can be concluded that strong coupling to the substrate by formation of image dipoles is the only plausible scenario resulting in the observed double-peak pattern of the 2PPE signal. It also naturally explains the qualitative difference between both types of surfaces which would be hard to interpret otherwise. In contrast to the strong coupling on clean Si(111)-(7x7) ($\varepsilon \approx 30$ for 400 nm wavelength [113]) the small permittivity of oxidized silicon ($\varepsilon = 2.16$, fused silica (SiO_2) for 400 nm wavelength [112]) effectively acts as a spacer layer; hence, the dipolar mode dominates the spectra (see Figure 4.2 and Figure 4.10a).

Scattering of Resonance Energies

Now the question of the origin of the large interparticle scattering of the resonance energies around the Mie trend on oxidized silicon is addressed, see Figure 4.7. The major contribution is assigned to the inhomogeneous structure of the nanoparticle substrate system. Due to the fact that the native oxide layer on the Si sample is neither fully crystalline nor is its composition well-defined but has a certain roughness, the local coupling is expected to differ depending on the detailed local structure of the particle-substrate interface.

As noted above, instrumental uncertainties cannot explain the observed scattering of data points: the statistical standard deviation from the Lorentzian fit (as shown in Figure 4.2) is typically below 4 meV. Pixel-wise fluctuations in the resonance energy maps (e.g. Figure 4.3a) are of the order of $\approx$ 10 meV for each particle, i. e. about one order of magnitude lower than the interparticle variations. The pixel-wise noise is tentatively attributed to the imaging system or to a systematic effect due to a more complex shape of the spectra. A frequently discussed physical origin of local variations of plasmon resonance energies is an inhomogeneous distribution of particle shapes and sizes. However, uncertainties of the height which are estimated to be 0.2 nm would not result in such scattering due to the relatively flat behavior of the plasmon energy size-dependence. Different shapes are only expected to lead to such pronounced variations if they significantly deviate from a spherical geometry. For supported ellipsoidal particles the vertical dipolar mode (mostly related to the short revolution axis of the particles) only weakly depends on the aspect ratio [29, 40]. The observed range of resonance energies would require aspect ratios (width/height) varying between unity and two which can be excluded based on AFM and transmission electron microscopy (TEM) data. Furthermore, a mode splitting would be expected which can not be seen for the vast majority of the particles on oxidized silicon (see rare exceptions for large particles described above). In the following, the oxidized sample (A) is compared to the pristine silicon sample with small nanoparticles (B) in a more quantitative way using statistical analyses.

Figure 4.12 shows a histogram of the resonance positions of all analyzed particles on oxidized Si (blue) and clean Si(111)-(7x7) with small particles (red). For the latter the peak positions are obtained via a fit of a sum of two squared Lorentzians (see Figure 4.8b). For better comparability only particles in the size range between 8 and 14 nm were considered for the oxidized sample (A) representing an upper limit for the size distribution of the silver nanoparticles on the pristine silicon surface (see Figure 4.8a). The dipolar plasmon peak positions follow Gaussian distributions with a FWHM of $\approx$ 75 meV for pristine silicon (B) and $\approx$ 65 meV for the oxidized sample (A). Please note that the analysis of quadrupole mode on Si(111)-(7x7) is only qualitatively valid because in some cases the resonance frequency is already located outside the available excitation range (dashed line and white bars of the peak on the right in Figure 4.12) and might overlap with higher order excitations (beyond quadrupole). Nevertheless, the data indicate comparable or even slightly higher variations of the resonance positions on pristine silicon, despite the expected smaller scattering of data points due to a better defined surface compared to the oxidized sample (A) as discussed in context of Figure 4.6. Interestingly, an increased variability of plasmon energies on Si(111)-(7x7) is easily explained for the image dipole scenario described above: because of stronger Coulomb coupling to the substrate even slight variations of the local environment substantially affect the particles' plasmon resonances as predicted in [114] and shown in Figure 4.10a. This mechanism also implies that on highly polarizable substrates such as Si(111)-(7x7) the particles can act as extremely sensitive plasmonic probes for the geometry of the system, particularly for the effective particle-substrate distance. From the theoretical calculations shown in Figure 4.10a a value of the order of 1 Å may be estimated for this system with a sensitivity in the sub-

Ångström regime. Note that these considerations are not limited to the assumption of spherical particles since the arrangement of facets in the vicinity of the particle-substrate interface is expected to play an important role for the exact position of the resonance, leading to strong variation of plasmon energies among the particle ensemble. A similar behavior has also been observed for electron-beam excitation using EELS [17] or dark field scattering [51].

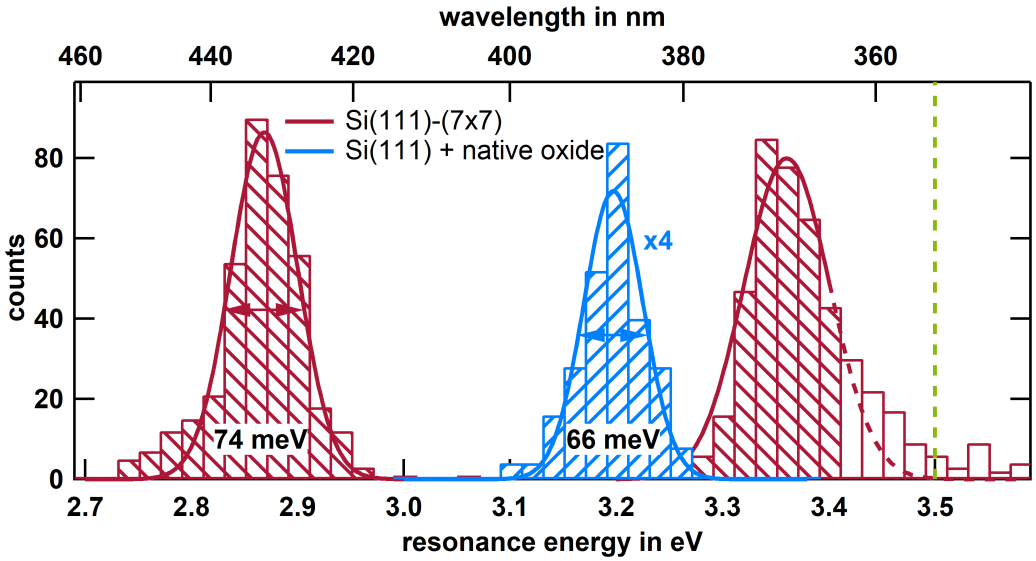

Figure 4.12: Histogram showing the position of resonance energies of silver nanoparticles on Si(111)-(7x7) (red, two resonances) and on oxidized silicon (blue, single resonance). The dashed green line at 3.5 eV indicates the plasmon energy of a free particle in vacuum as a reference. The uncertainty of each individual particle is within the width of the bars. Particles are of comparable size for both substrates. The distributions were fitted by Gaussians (solid lines) to determine the FWHM. For energies > 3.4 eV the dashed part of the red curve, and the blank bars of the histogram indicate a higher uncertainty since part of the corresponding resonance curves are outside of the available excitation range. Figure adapted from [KO-4].

Dephasing Times

Like for plasmon resonance energy on oxidized and pristine silicon (see Figure 4.12) a corresponding statistical analysis is done for the dephasing times T_2. The results are shown in Figure 4.13. For A similar statistical analysis particles on oxidized silicon $T_2 = 3.7\,\text{fs} \pm 0.4\,\text{fs}$ is obtained (Figure 4.13a). Here the entire observed size range is used for this analysis in contrast to the restricted range used in Figure 4.12. For particles on Si(111)-(7x7) a slight increase to 4.2 fs of the dephasing time of the dipolar mode was observed along with a significant higher standard deviation. This change is considered not to be significant given the relatively broad distributions. For reasons mentioned above, the higher order mode is not analyzed quantitatively, but it seems to exhibit a reduced dephasing time T_2 compared to the low energy mode. The wider distribution of dephasing times on clean silicon again indicates a more sensitive dependence on the local arrangement near the particles compared to the oxidized surface, which further supports the scenario of pronounced coupling to the substrate via image dipole creation.

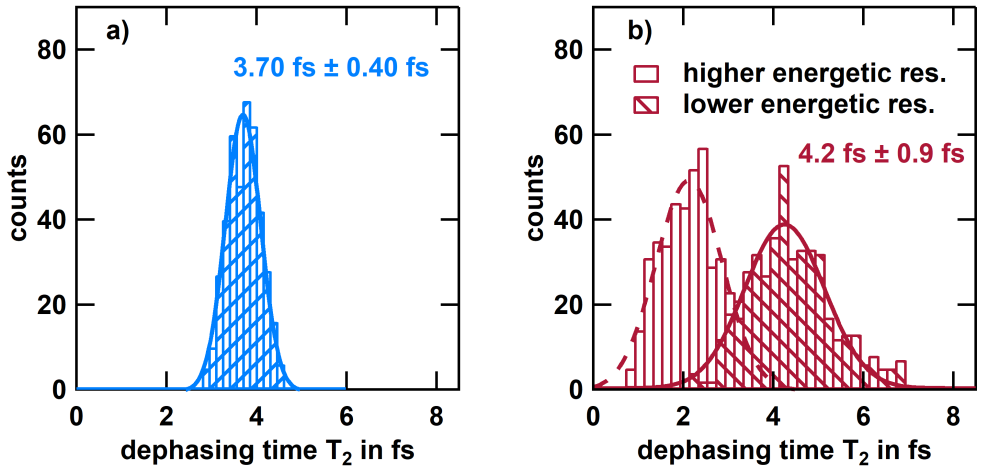

Figure 4.13: a) Distribution of dephasing times T_2 for clusters on oxidized silicon for the entire observed size range. b) Same for the low and high energetic mode on pristine Si(111)-(7x7). The results of the best Gaussian fits including the standard deviations of the distribution are indicated in both panels. Figure adapted from [KO-4].

The observed dephasing times T_2 can be separated into a part T_2^* and an inelastic lifetime T_1 describing pure dephasing and a decay via energy transfer, respectively (see Section 2.1.3):

$$\frac{1}{T_2} = \frac{1}{2T_1} + \frac{1}{T_2^*} \quad .$$

In the case of gold nanoparticles the influence of pure dephasing T_2^* due to scattering on surfaces or inhomogeneous phase velocities can be neglected [46] and therefore determination of T_1 becomes possible. For silver nanoparticles contributions from pure dephasing T_2^* and decay over energy transfer T_1 into photons or excitons are both involved [45, 46], such that further assumptions would have to be made to gain information about the detailed decay processes [45].

In contrast to the energetic position of plasmon resonances it is not straightforward to obtain information about averaged dephasing times from spectroscopic ensemble measurements due to inhomogeneous broadening of the resonance. For illustration, a single particle spectrum on oxidized silicon is compared to a spectrum averaged over all 66 particles analyzed in Figure 4.12 representing a narrow size distribution as shown in Figure 4.14. Consequently, experimental data of the damping behavior of single silver spheres in this size range are rare, e. g. Sönnichsen reported on dephasing times around 4 fs for 20 nm silver spheres in immersion oil [51]. To overcome this issue the persistent spectral hole burning method [125, 126] was established to estimate dephasing times from ensemble measurements, yielding $T_2 = 4.8$ fs for 15 nm oblate Ag particles on quartz [125] and $T_2 = 4.3$ fs for 18 nm Ag spheres on quartz [127]. Also other experiments with silver spheres in this size range, assuming weak inhomogeneous broadening, yielded values around 4 fs [54, 128, 129] which is compatible with our single-object data.

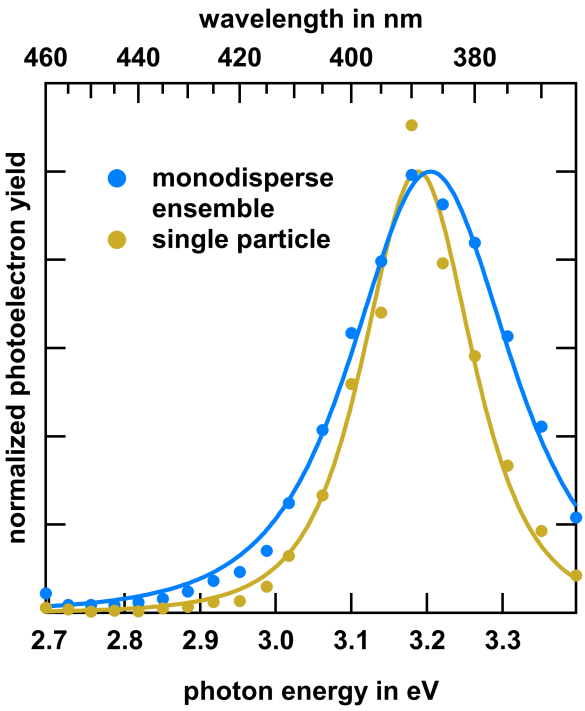

Figure 4.14: Comparison of a representative normalized single particle spectrum on oxidized silicon with a normalized spectrum averaged over the narrow size distribution used for Figure 4.12. The Figure illustrates that only resonance position can be determined straightforward from an ensemble measurement while inhomogeneous broadening is masking the width of individual spectra.

Quality Factor

The quality factor Q obtained from the resonance curves is of the order of 10, in accordance with data in the literature for related nanoparticles [46, 54, 55]. As the Q factor directly gives the local field enhancement [52, 53, 110] this leads to a hundred times higher local light intensity. For second order nonlinear processes like two photon photoemission the yield is increased by a factor of 10 000. This compares well to earlier single-object studies such in [97], where a signal enhancement of 30 was observed for silver nanoparticles compared to a thin silver film in slightly off resonant conditions, indicating an enhancement of about 30 000 when perfect matching of the resonance would have been achieved. Lower factors up to 2 000 were observed for 34 nm silver particles [130].

4.2 KINETIC ENERGIES OF THE PHOTOELECTRONS

After determining the plasmonic properties of the silver nanoparticles in the previous section, we now investigate the kinetic energy distributions of the emitted photoelectrons. These spectra allow deducing valuable information on the emission process itself, for example whether the initial, intermediate, or final state is participating, the work function, changes of surface potentials etc. The spectra are acquired using the DLD providing a three dimensional dataset (i. e. spatial origin (x,y) and the time of flight (t) of the photoelectrons) for each excitation configuration in a single shot experiment[3] enabling the correlation of spectral and spatial properties. For all measurements in this section Sample C with silver nanoparticles ($\approx$ 25 nm diameter) on Si(111)-(7x7) was used. All spectra are plotted as a function of binding energy using the Fermi level as zero energy reference. For details on the conversion from ToF to an energy scale and on the determination of the Fermi level see Appendix A.5. Unless otherwise stated the spectra show the photoelectron yield under p-polarized fs-laser excitation at 2 mW average laser power integrated over the whole FoV of 20 µm containing regions of pure silicon as well as regions where clusters are located.

4.2.1 SPECTRAL DEPENDENCE ON EXCITATION WAVELENGTH

Figure 4.15 exemplarily shows the photoelectron yield as a function of binding energy E_{bin} for four different excitation wavelengths. The position of the Fermi level corresponds to zero binding energy representing the low binding energy onset (high kinetic energy) of the curves. The spectra obtained from 360, 380 and 430 nm excitation wavelength show a similar slope at the Fermi level, the yellow curve (405 nm) has a noticeably flatter onset resulting in less counts in that regime. While the blue curve (360 nm) forms a plateau around 0.5 eV followed by a dominant peak with a weak shoulder, the other spectra show a continuous increase of the photoelectron yield developing a double peak structure with less intensity at the high energetic side[4]. The position of the dominant peak shifts to higher binding energies with decreasing excitation wavelength from $E_{bin} \approx 1$ eV (red curve, 430 nm) to $\approx$ 2.5 eV (blue curve, 360 nm). Except for the yellow spectra (405 nm) the peak height also increases with increasing photon energy. This behavior is a direct consequence of the secondary electron cutoff on the left side of the spectra which is visible best by comparing the red and green curve. Both spectra are starting identical at the Fermi level but the red curve is suddenly cut off. This cutoff at around 1.3 eV represents zero kinetic energy of the emitted photoelectrons. Hence, the apparent low-energy peak rather is caused by a sudden cutoff of the increasing intensity at low kinetic energies. The available photon energy does not suffice to lift stronger bonded electrons above the vacuum energy. Therefore the dependence of the cutoff on the photon energy becomes obvious leading to significant differences in the widths of the spectra.

3 Here, single shot means that all three quantities (x,y,t) are acquired simultaneously within each laser pulse whereas in imaging energy filter (IEF) mode the measurement must repeatedly be done with different retarding fields. The total signal however corresponds to a sum over many laser pulses.

4 Here, the high energetic side means high kinetic energies and higher lying initial electronic states corresponding to lower binding energies.

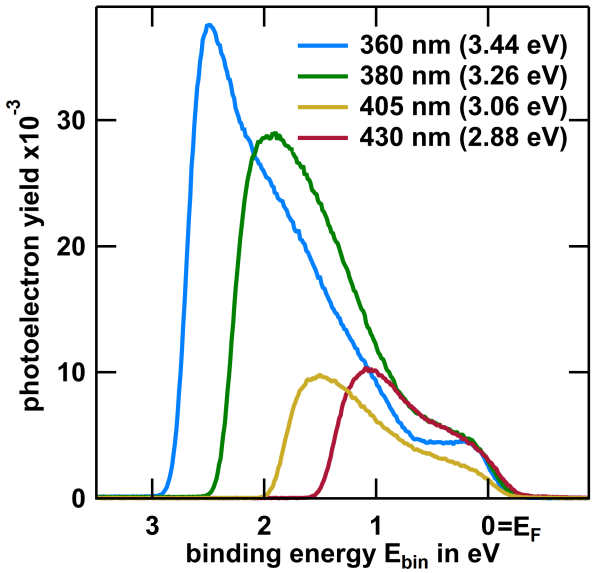

Figure 4.15: Photoelectron yield as a function of binding energy E_{bin} for four different excitation wavelengths ranging from 360 nm (blue curve) to 430 nm (red curve). The spectra are acquired at the same average laser power of 2 mW and are integrated over a FoV of 20 µm with a silver cluster density of $\approx 0.3\,\mu\text{m}^{-2}$ on Si(111)-(7x7).

For a better impression of the development of the spectra Figure 4.16 shows all measured curves in a waterfall plot as a function of photon energy. Different colors represent distinct excitation wavelengths as can be seen on the photon energy axes. The onset of the curves at the Fermi level is similar except for lowest photon energies and curves around 3 eV (yellow) as also visible in Figure 4.15. The continuous shift of the secondary electron cutoff ranges from around 1 eV to almost 3 eV binding energy, which will be further analyzed in Section 4.2.3.

4.2.2 SPATIAL CONTRIBUTIONS

In addition to the averaged spectra, we can now use the spatial resolution in PEEM to distinguish signals originating from the particles and the substrate to identify spatial contributions to the spectral shape. Figure 4.17 shows again the spectra integrated over a complete PEEM image with a FoV of 20 µm for 360 nm (a) and 430 nm (b) excitation wavelength as black curves. By selectively summing up only parts of the image where silver clusters are located the blue curves are obtained representing the photoelectron yield originating directly from the cluster or the near vicinity. The red curves are the result of integrating only areas of the image where clusters are far away, representing the silicon signal. The areas were selected by using a threshold value for the photoelectron yield per pixel. Since the emission of electrons from the cluster is much more spatially restricted the yield per pixel is much higher, therefore pixels above the threshold belong to the cluster area. For determining the silicon area another threshold was used acting as an upper limit of the yield. The usage of a second threshold was necessary to clearly distinguish between cluster and silicon avoiding regions were mixed signals are obtained due to limited spatial resolution. As a consequence the black curves in Figure 4.17 are not equal to the sum of cluster and silicon signals. For the case of 360 nm excitation wavelength (Figure 4.17a) the cluster signal shows a single peak at a binding energy around 2.5 eV directly at the secondary electron cutoff. For 430 nm (Figure 4.17b) the nanoparticle peak has shifted to approximately 1 eV which is at the low energetic cutoff

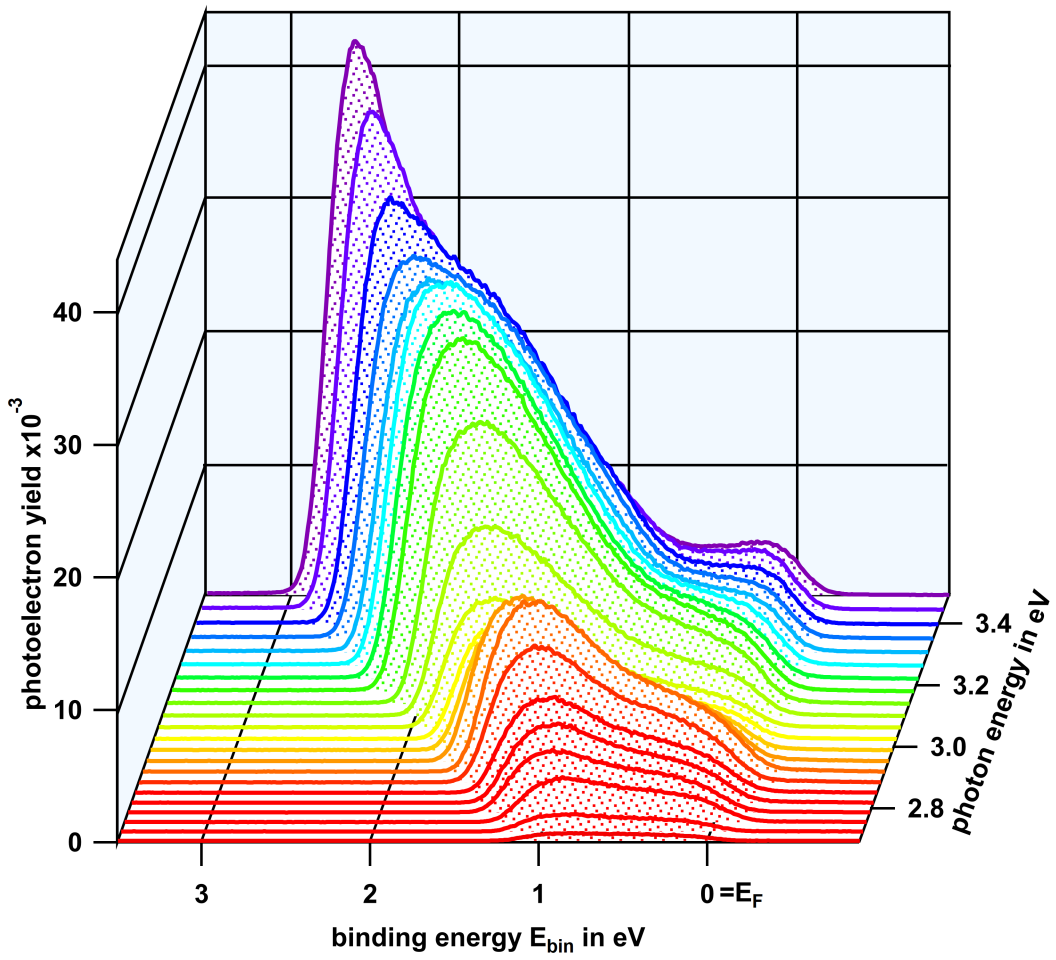

Figure 4.16: Same spectra as in Figure 4.15 with additional curves for all employed photon energies ranging from 2.7 eV (red) to 3.5 eV (purple).

as well. Apparently, the absolute photoelectron yield at this position has also increased. The silicon signal in both cases consists of two peaks where the smaller one is located directly below the Fermi level. The more intense peak has its maximum at 1.8 eV for 360 nm excitation and at 1 eV for 430 nm, respectively. In the latter case this is the position of the secondary electron cutoff which is at slightly lower binding energies compared to the silver signal. For higher photon energies the secondary electron cutoff is far beyond the maximum of this peak.

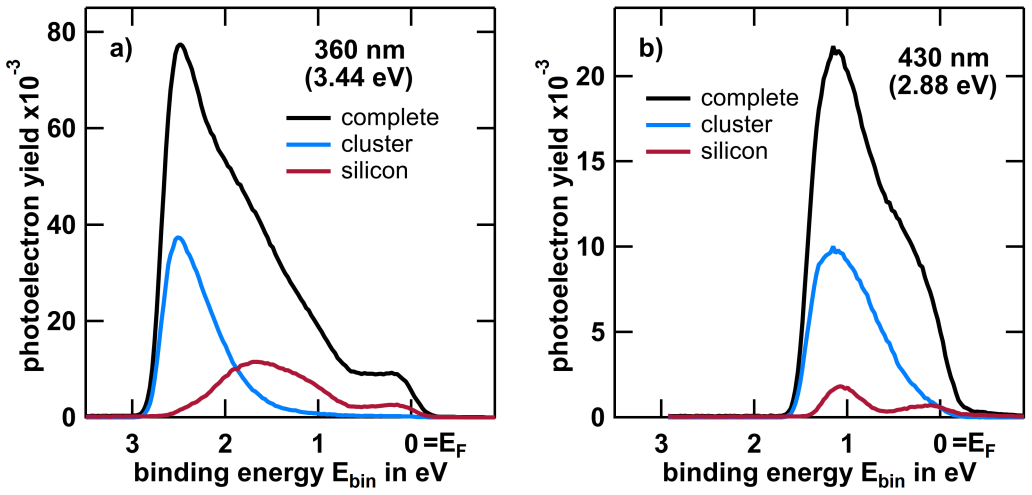

Figure 4.17: Photoelectron spectra as a function of binding energy obtained from areas with clusters (blue curves), without clusters (red curves), and a complete image (black curves) for a) 360 nm and b) 430 nm excitation wavelength, respectively. Please note that the complete signal is not equal to the sum of cluster and silicon signals. See text for details.

To evaluate the evolution of the peaks, the signals for all excitation wavelengths are plotted in waterfall graphs in Figure 4.18 for the cluster signal, and in Figure 4.19 for the silicon signal, respectively. The nanoparticle spectrum shows a single peak undergoing a strong shift in binding energy being always located at the cutoff energy. A Fermi edge is clearly visible on a logarithmic scale for all spectra at zero binding energy. The peak height shows some variations but tends to increase with rising photon energy. Variations will be discussed on page 45.

The silicon signal (Figure 4.19) shows a different behavior concerning the shifts of the peaks. While the lower signature is located at a constant energy near the Fermi level, the major peak is shifting much weaker compared to the cluster peak in Figure 4.18. Therefore its distance to the cutoff is increasing which can be recognized by comparing the evolution of the cutoff position and the peak's maximum. Concerning the peak height a clear growth is visible in contrast to the appearance near the Fermi level where the electron yield is constant apart from the lowest photon energies and the region about 3 eV (yellow curves). The origin of these spectral shapes will be discussed on Page 45.

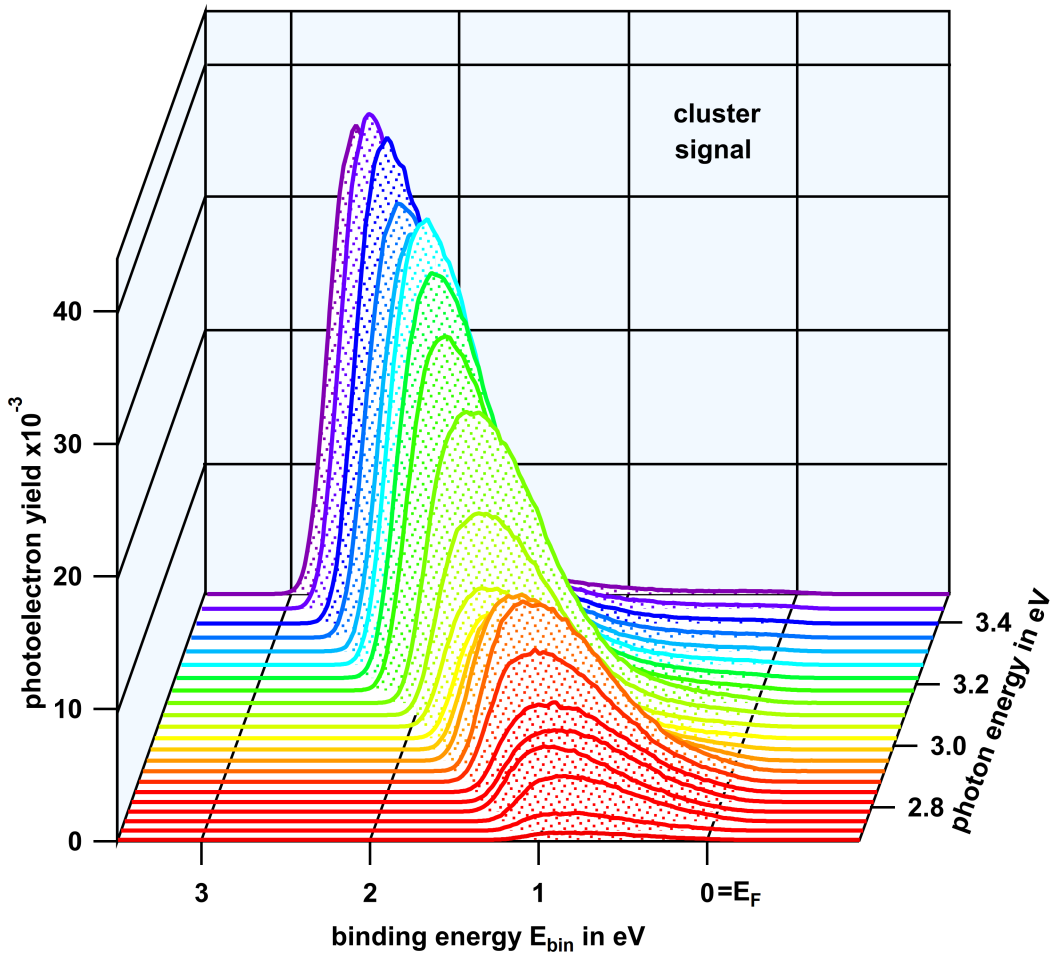

Figure 4.18: Extracted spectra from areas with silver nanoparticles for all excitation wavelengths employed. Curves for 3.44 eV and 2.88 eV are the same as shown in Figure 4.17a and b, respectively.

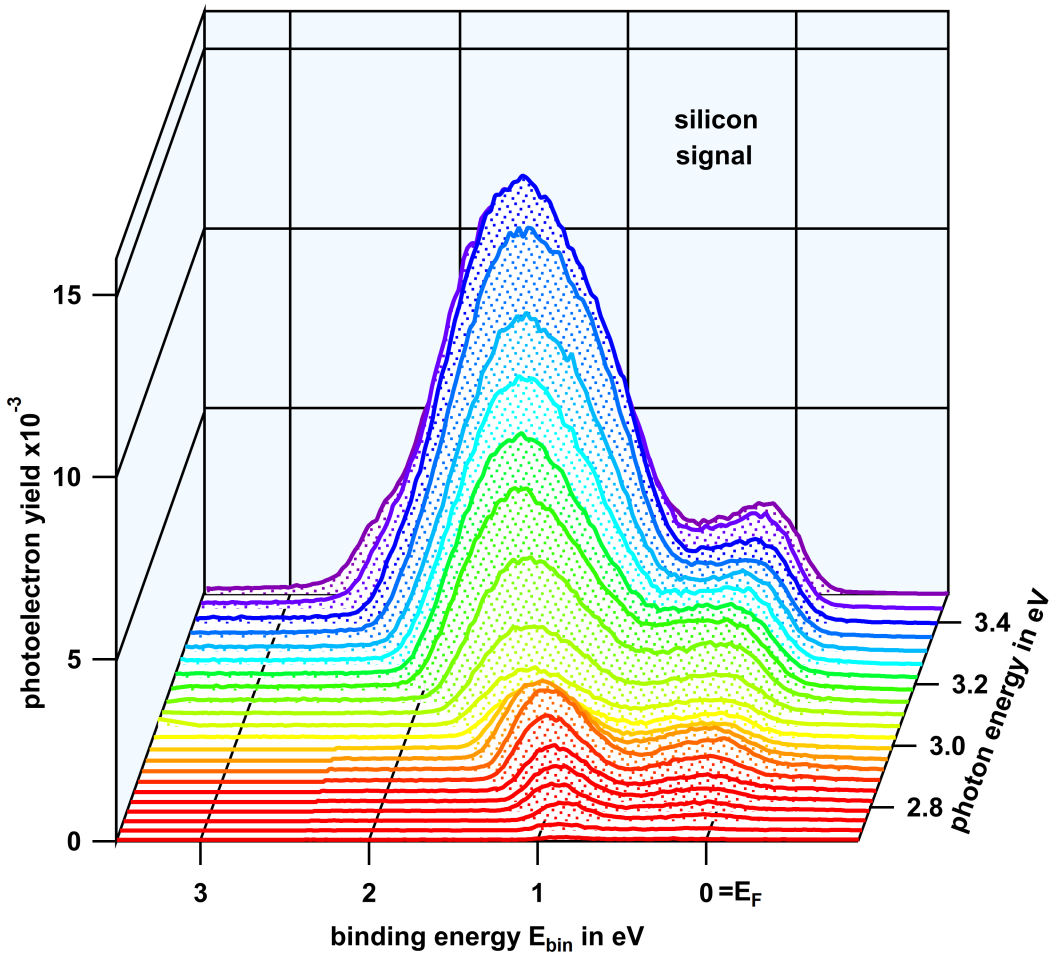

Figure 4.19: Same as Figure 4.18 for the signal obtained from areas without nanoparticles.

4.2.3 DETERMINING THE WORK FUNCTION

According to Einstein's famous equation [131]

$$\Delta E_{kin} = E_{exc} - W\,, \tag{4.1}$$

where W is the work function and E_{exc} is the excitation energy, here being equal to $2\hbar\omega$ due to the 2PPE process, the work function can be obtained from the widths ΔE_{kin} of the spectra. For an individual spectrum cutoffs could be hard to identify exactly therefore ΔE_{kin} is measured as a function of $\hbar\omega$ to determine W by a linear regression where individual measurements have less influence. In addition, the photon order n of the n-photon photoemission (nPPE) process can be determined by the slope independent from its power dependence. Figure 4.20a shows ΔE_{kin} (black dots) as a function of $\hbar\omega$ for all spectra shown in Figure 4.16. The dashed line represents the best fit according to Equation 4.1 leading to a work function of (4.284 ± 0.012) eV. The same procedure was done for the spectra plotted in Figure 4.18 and 4.19 resulting in $W_{Ag} = (4.194 \pm 0.013)$ eV and $W_{Si(111)-(7x7)} = (4.480 \pm 0.010)$ eV as shown in Figure 4.20b representing the silver (blue) and silicon signal (red), respectively. The given errors just representing the statistical error, systematic deviations are discussed later on Page 47. The obtained work functions are in accordance with values from the literature: 4.26 eV for polycrystalline silver [120] and 4.55 eV for Si(111)-(7x7) at room temperature [132, 133]. A detailed discussion can be found on page 47.

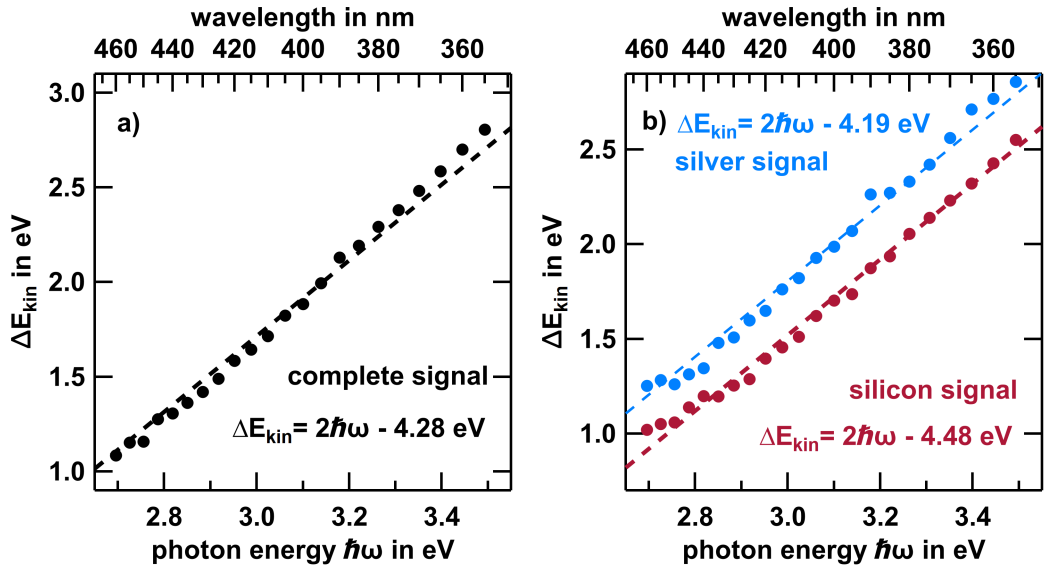

Figure 4.20: Energetic width of photoelectron spectra ΔE_{kin} as a function of excitation photon energy for the a) complete signal and b) for the silver (blue dots) and silicon signal (red dots), respectively. The dashed lines are least square fits of a linear function where the intersections with the y-axis represent the work functions leading to 4.28 eV for averaged spectra and 4.19 eV/4.48 eV for silver/silicon spectra, respectively.

4.2.4 SPECTRAL DEPENDENCE ON POLARIZATION

So far all measurements were done using p-polarized illumination containing both in-plane and out-of-plane components of the electric field with respect to the surface. By switching to s-polarization only in-plane components (parallel to the surface) of the light field are present. Hence, light can only be absorbed by electronic states having

sufficient oscillator strength in this direction giving a possibility to discriminate the origin of signals obtained in p-polarization. Figure 4.21a shows the photoelectron yield as a function of binding energy for the same sample area as investigated before for p- (red curve), and s-polarized (blue curve) light with 360 nm wavelength. It is obvious that the total electron yield decreased by nearly two orders of magnitude compared to p-polarized excitation of the same averaged laser intensity. The spectrum obtained from s-polarized excitation is magnified by a factor of 100 allowing us to compare the features in the same graph. The shape of the first peak, located slightly below the Fermi level, is not affected essentially while the ratio of the two following peaks has changed drastically. The feature around 1.8 eV, which was attributed to silicon (see Figure 4.17a), increased significantly compared to the peak originating from the silver nanoparticle system around 2.5 eV at this excitation energy. While with p-polarized excitation it was only a weak shoulder, it raised to the dominant contribution. The position of the secondary electron cutoff remains unchanged with respect to the Fermi level, leading to an identical spectral width ΔE_{kin}. In Figure 4.21b the evolution of the total photoelectron yield (green circles), which is the integrated signal over all binding energies, is shown as a function of the polarization angle φ for 430 nm excitation wavelength. P-polarization is achieved at $\varphi = 0°$ while $\varphi = 90°$ corresponds to s-polarization, respectively. The data show a minimum at s-polarization while the maximum yield achieved at p-polarized excitation is around 200 times higher. The dashed green line is a least square fit of $A + B\cos^4(\frac{2\pi}{360°}\varphi + C)$ with A, B, C as free parameters. The inset shows the total photoelectron yield PEEM images at p-polarization (top) and s-polarization (bottom), respectively. To fit on the same color scale like the top image, the yield obtained by s-polarized excitation was multiplied with a factor of 1 000. In the top image, silver nanoparticles are clearly dominating the total yield while the background appears nearly black. However, for s-polarization clusters are hardly visible while the complete image shows a statistically fluctuating background.

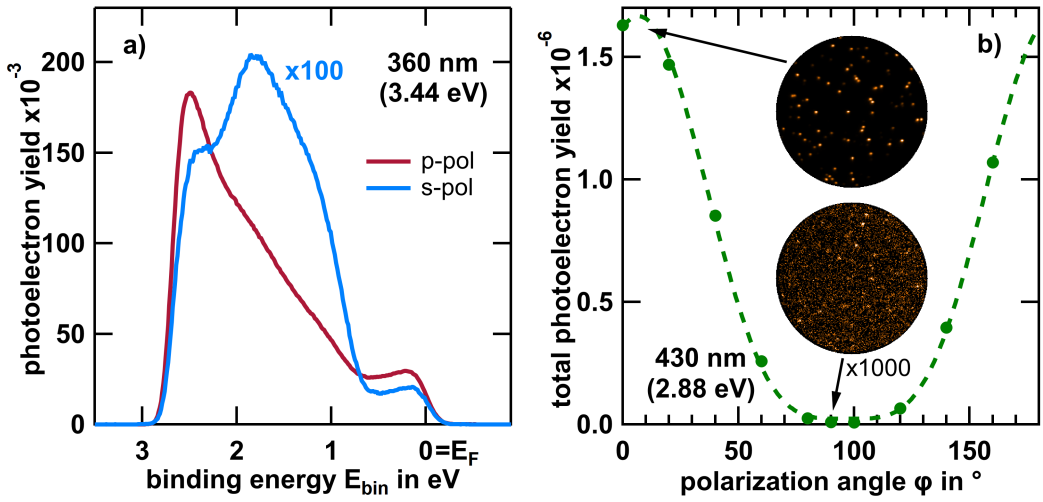

Figure 4.21: a) Spatially averaged photoelectron yield as a function of binding energy for p- (red curve) and s-polarized (blue curve) excitation at 360 nm wavelength. The blue spectrum is magnified by a factor of 100. b) Total photoelectron yield as a function of polarization angle φ of the illuminating laser. $\varphi = 0°$ corresponds to p-polarization. The dashed line is the result of a least square fit with a $\cos^4$ dependence. The insets show total photoelectron yield PEEM images obtained with p- (top) and s-polarization (bottom), respectively. The yield displayed in the lower image was multiplied by a factor of 1 000 for better visibility.

4.2.5 SPECTRAL DEPENDENCE ON EXCITATION INTENSITY

After having changed the excitation wavelength and polarization to study the photoelectrons' response, the last major property to adjust is the laser intensity. Figure 4.22a shows the total photoelectron yield Y as a function of laser power P at 360 nm wavelength. In the double logarithmic plot the data points follow the power law $Y \propto P^n$ with $n = 2.07$ as best fit (dashed line), demonstrating that 2PPE is the dominant process (for details see Section 3.1 and Appendix A.3) [104]. The same analysis was done for each binding energy separately providing the order of the multi-photon process as a function of binding energy as shown by the blue curve in Figure 4.22b. To guide the eye a typical photoelectron spectrum is shown as well (black curve). For the main part of the spectrum the order n of the nPPE process is around 2 with obvious deviations at both cutoffs. At the Fermi level the order decreases to a value of 1 followed by a fluctuation between 2 and 3, while values above 4 are obtained at approximately 3 eV binding energy. These results seem to be counterintuitive as one would expect increased kinetic energy of the emitted electrons for higher order processes leading to signatures on the right side of the spectrum where in contrast a reduced order is measured. The results will be discussed on page 54 in the context of the influence of SPVs on the apparent power dependence.

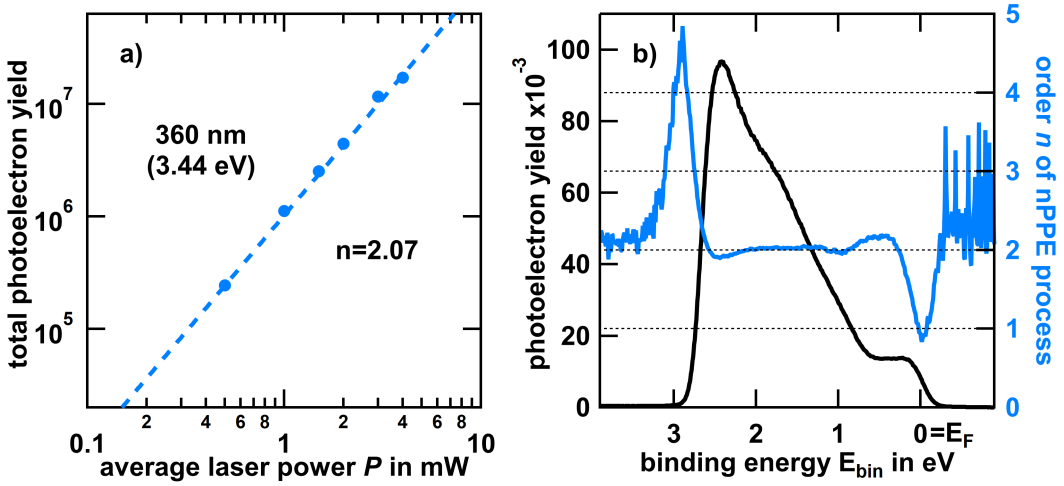

Figure 4.22: a) Double logarithmic plot of the total photoelectron yield (integrated over all binding energies, blue dots) as a function of laser power for 360 nm excitation wavelength. The dashed line represents the best linear fit of the obtained data. The slope of $n = 2.07$ indicates that 2PPE is the dominant emission process. b) The black curve shows a typical photoelectron yield at 360 nm illumination wavelength as a function of binding energy. Analogous to a) the fit was done for each binding energy separately giving the order n as a function of binding energy shown by the blue curve.

To visualize changes in shape, the photoelectron spectra for different excitation powers are shown in Figure 4.23. The curves were normalized according to the power law observed in Figure 4.22a. The main peak's height decreases with increasing laser power. In addition, a shift towards higher binding energies is visible for the entire spectrum.

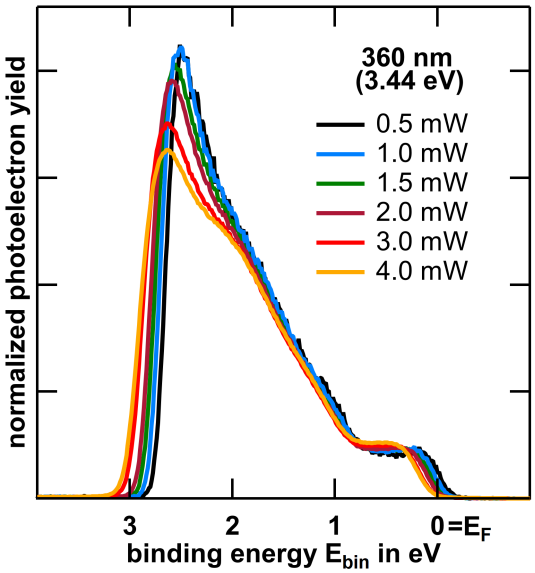

Figure 4.23: Normalized photoelectron yield as a function of binding energy for illumination with 360 nm wavelength with different laser powers ranging from 0.5 mW (black) to 4 mW (yellow).

4.2.6 DISCUSSION

In this part, the obtained results will be thematically interpreted and discussed with respect to literature.

Origin of Spectral Shapes

First we focus on the spectral shapes of the acquired spectra. To this end, spectra are decomposed into silicon and cluster contributions. In addition, the evolution of the spectra with excitation power is analyzed with regard to the involved states of the photoemission processes.

Let us start with the signal originating from the silver cluster positions which is shown in the waterfall plot in Figure 4.18. The spectra are dominated by a single peak always being located at the low energy cutoff. This is a typical signature of secondary electrons which have lost a part of their energy in scattering events prior to the photoemission process itself. In contrast to flat Ag surfaces where 2PPE processes only take place in direct transitions ($\Delta k = 0$) over virtual intermediate states due the mismatch of the photon and electron momentum k at these experimental conditions [57, 134] and the absence of a real intermediate state [135], 2PPE at nanoparticles can proceed via indirect transitions ($\Delta k \neq 0$) through real intermediate states due to the strong spatial dependence of the near field [57, 134]. After excitation of the intermediate state by absorbing a photon of the near-field or through the decay of the collective plasmon mode into an electron-hole pair, the population can undergo an energy-dependent relaxation process, mainly by electron-electron scattering [134, 136, 137]. In a typical collision an electron loses around 50 to 66 % of its excitation energy δE [138, 139]. The relaxation times of the intermediate state are proportional to $1/\delta E^2$, ranging from 2 fs at high energies to a few hundreds of femtoseconds close to the Fermi energy [134, 137]. This energy-dependent relaxation of the intermediate state explains the shape of the measured Ag cluster spectra with a dominant peak always located at the secondary electron cutoff. Beside these sequential processes also simultaneous excitations are possible, where the energy of two photons is coherently transferred to one electron in a single step without further scattering processes. The presence of a sharp Fermi edge as it will be discussed on page 47 as well as a shift of $2\hbar\Delta\omega$ of the electrons' kinetic energies at the Fermi edge show

that these direct transitions are a substantial part of those processes [54, 99, 140]. The simultaneous excitation preferentially occurs via the decay of a coherent multi-plasmon state [50, 101, 141, 142] where an at least double excited plasmon transfers the complete energy into a single electron. This ionization decay demonstrates the efficient Landau damping of the collective plasmon mode, i. e. the strong coupling between collective and single-particle excitations [101, 143]. Please note that the possibility of exciting a multi-plasmon state for metallic nanoparticles on surfaces has been an open discussion for a long time because of the distortion of the harmonic plasmon potential due to the presence of a substrate [50, 101, 141].

After analyzing the shape let us focus on the photoemission yield. The peak height as well as the sum of the emitted electrons does not monotonically increase with increasing photon energy. Instead it contains the signature of the plasmonic properties discussed in the previous section. For this sample (C) with silver nanoparticles of $\approx 25\,\mathrm{nm}$ diameter on Si(111)-(7x7) three resonances were expected as can be seen in Figure 4.9b) and 4.11b) which correspond to the modulation of the electron yield in the spectra.

In contrast, the silicon signal (Figure 4.19) shows a more complex structure mainly consisting of a minor peak slightly below the Fermi edge and dominant peak between 1 and 2 eV binding energy. The band structure of silicon shows a gap of 1.14 eV with the Fermi energy in between. Below the valence band, further states can be found with a monotonic rising DOS until approximately 3 eV below the band edge [144]. Apart from these bulk states the evolution of surface states was observed. For the Si(111)-(7x7) surface reconstruction investigated here, the presence of three filled surface states at binding energies of $S_1 \approx 0.2\,\mathrm{eV}$, $S_2 \approx 0.8\,\mathrm{eV}$, and $S_3 \approx 1.8\,\mathrm{eV}$ relative to the Fermi level is well known [145–150]. With this knowledge the minor peak at the Fermi level can be most probably attributed to the S_1 surface states which is formed by the adatom dangling bond within the dimer-adatom-stacking fault model [150, 151]. The other two surface states are supposably masked by the valence band photoemission. Figure 4.19 shows the inset of the peak at around 0.8 eV below the Fermi edge, typical of n-type silicon. With increasing photon energy the peak starts to shift and rise. Both are observations due to the secondary electron cutoff. With increasing photon energy, deeper lying states can be probed, and because of the monotonic rising DOS the peak shifts and intensity become larger. At the highest photon energies used here the photoemission yield increases slowly at small kinetic energies at the secondary electron cutoff which does not reflect the valence band's DOS [144]. But since we are doing 2PPE we preferentially need an intermediate state. For highest photon energies used here the intermediate state is located right at the onset of the conduction band where the DOS is low restraining the photoemission yield. Nevertheless, signal is still present in this region either due to direct 2PPE or sequential processes with a low dense intermediate state.

Polarization Dependence

In Figure 4.21 we have seen the polarization dependence of the spectra (a) and of the total photoelectron yield (b). The latter shows a $\cos^4(\varphi)$ dependence which is typical of a 2PPE process on planar surfaces where both photons are absorbed by a dipole resonance perpendicular to the surface [96, 152–154]. But also for nanoparticles on surfaces this behavior was observed and interpreted as an exclusive excitation of the perpendicular plasmon resonance [50]. This increases confidence in the interpretation that we are only sensitive to the perpendicular (out-of-plane) plasmon modes as stated in section 4.1.5. Although both cluster and substrate signal behave in good approximation to a $\cos^4(\varphi)$ dependence Figure 4.21a shows that the relative intensities change and the silicon signal becomes dominant in s-polarization which is also nicely visible in the PEEM images in Figure 4.21b. This means that slight deviations might occur due to the formation of the surface states.

Electron Temperature

Beside the patterns of the spectra and their polarization dependence also the shape of the Fermi edge contains valuable information. Figure 4.24 shows a detailed view on the Fermi edge of the entire system (silicon + nanoparticles) acquired at 360 nm wavelength (blue dots). Please note that the Fermi edge of the individual signals from cluster and substrate does not differ significantly from this spectra apart from the photoelectron yield. The wavelength was selected due to the relative constant signal below the Fermi level giving the possibility of an undistorted analysis. The interesting parameter is the width of the Fermi edge which is connected to the electron temperature T via the Fermi-Dirac distribution [155]

$$f(E) = \frac{1}{e^{(E-E_F)/k_B T} + 1} \quad . \tag{4.2}$$

The best fit using Equation 4.2 of the Fermi edge is shown as red line in Figure 4.24 and corresponds to a temperature of $T \approx 720\,\mathrm{K}$. For supported nanoparticles the temperature depends on the in-coupled power and on the coupling to the substrate allowing dissipation of the energy. In case of a poor coupling to the substrate reasonable heating of nanoparticles was reported [104, 134]. Here the same width of the Fermi edge from silicon and cluster signal is observed.[5] Since the substrate does certainly not warm up substantially under laser illumination at our experimental conditions we can assume that the whole system stays at room temperature of 300 K. Now, the Fermi width opens the possibility to determine the energetic resolution of the instrument, because a broadening is expected as well due to the experimental acquisition. By a convolution of the Fermi-Dirac distribution at 300 K with a Gaussian point-spread function the energetic resolution of the instrument was determined to be $\approx 100\,\mathrm{meV}$ (not shown) which is in accordance with the time resolution of the DLD under these specific experimental conditions using a drift voltage of 20 V.

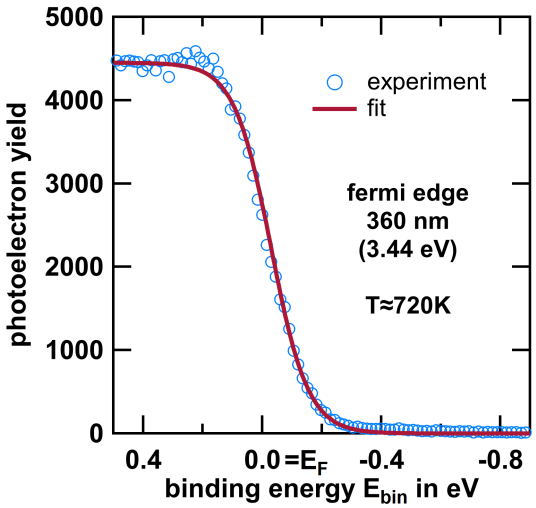

Figure 4.24: Detailed photoelectron yield (blue circles) as a function of binding energy around the Fermi level for 360 nm illumination wavelength together with a least square fit (red line) of a Fermi-Dirac distribution. The width of the Fermi edge corresponds to a temperature of 720 K in the Fermi-Dirac distribution.

5 Here, it is assumed that the Fermi edge of the cluster signal does not originate from the underlying silicon, which is supposed to be unlikely due to the lack of other spectral signatures.

Work Function

The work functions determined in section 4.2.3 were $W_{Ag} = (4.194 \pm 0.013)$ eV for the silver nanoparticles and $W_{Si(111)-(7x7)} = (4.480 \pm 0.010)$ eV for the Si(111)-(7x7) substrate, respectively. Both quantities are 0.07 eV smaller than the literature values [120, 132, 133], which is below the energetic instrumental resolution of approximately 0.1 eV. In addition, small nanoparticles are known to have a slightly reduced work function compared to the bulk material, which is around 0.1 eV for Ag cluster in this size range [134].

At a first glance it appears to be intuitive that the determined work function of the complete signal ($W_{compl} = (4.284 \pm 0.012)$ eV) is in between the individually acquired ones. Upon closer examination equation 4.1 implies that a combined work function must be less or equal to the smallest individually obtained since the width ΔE_{kin} is analyzed, which cannot become smaller by adding further photoelectron signal measured. Therefore the only possibility remaining is an imprecise determination of the spectral cutoffs leading to ΔE_{kin}. It turns out that the determined Fermi edges appear to shift sparsely when adding additional signal. To be precise, the signal close to the silver Fermi edge is weak compared to the one in the silicon spectra. At higher binding energies an additional Fermi edge appears which is followed by a three-photon photoemission (3PPE) yield (for details see page 54) overlapping with the silver's Fermi edge. Hence, the exact position of the silver Fermi edge is masked by silicon signal and the additional 3PPE yield. To conclude, the determination of individual work functions appear valid while in spatially averaged measurements only the lowest value is obtainable even though it might be slightly effected by other contributions.

In related PES experiments often the ionization potential is extracted from the width of the kinetic energies [156–158], while here the results are supposed to be equal with the work function. Indeed, the ionization potential is measured when the remaining photohole is not screened sufficiently by the system's charge carriers leading to an additional attractive coulomb interaction. The corresponding charge neutralization time τ_n [159] defines the gap between work function and ionization potential. In the limit of $\tau_n \to 0$ the shift is zero, for $\tau_n \to \infty$ the shift becomes $\propto e^2/R$ for the model of a spherical metal cluster with radius R [134, 160–162]. Hence, the electron requires more energy to leave the system. This behavior is typically observed for free clusters in a beam [158, 163] but e. g. Cinchetti et al. also reported a shift of 0.13 eV for silver clusters on a silicon substrate [134]. In our case, due to the coupling to the substrate which has metallic surface states it is assumed that the hole is efficiently screened leading at most to minor deviations, additionally the electrons' kinetic energies are relatively small compared to conventional UV-PES leading to a long residence time of the electrons in the Coulomb potential. Hence, the system has more time to sufficiently screen the photohole. Another possibility to access a possible electric conductivity is to analyze the sample temperature by the width of the Fermi edge and interpret the findings using Wiedemann-Franz law which connects thermal and electrical conductivity. However, due to energetic resolution of the instrument we can not see a significant broadening (see discussion on page 47) which hinders a detailed analysis. In addition, other transport channels as e. g. tunneling are not considered.

Another peculiarity of a PEEM experiment compared to conventional PES is the high extractor voltage of ≈ 12 kV lowering the potential barrier above the sample's surface and hence increases the photoemission extraction probability. In addition, the width of the electron's kinetic energy distribution can be broadened due to tunneling through this barrier. However, this effect is already included in the analyzer's work function which was determined by using a polycrystalline silver reference sample [69]. Nevertheless, the presence of the silver nanoparticles leads to field inhomogeneities and an increased electric field in the cluster vicinity. Figure 4.25a shows an electrostatic simulation based

on the numerical solution of the three dimensional Poisson equation conducted by Sven Kraft[6] for a metallic sphere with 10 nm diameter deposited on a conductive substrate. Like in the PEEM geometry an extractor being at 12 kV potential is located 1.8 mm away from the surface. The line profiles of the two dashed black lines are shown in b) while the electric field along these profiles is plotted in c). At $x = 40$ nm, sufficiently away from the particle, the potential is undisturbed being just linear with a homogeneous electric field. However, the presence of the cluster disturbs the potential leading to an enhanced electric field in the vicinity of the nanoparticle (see red line in Figure 4.25c)).

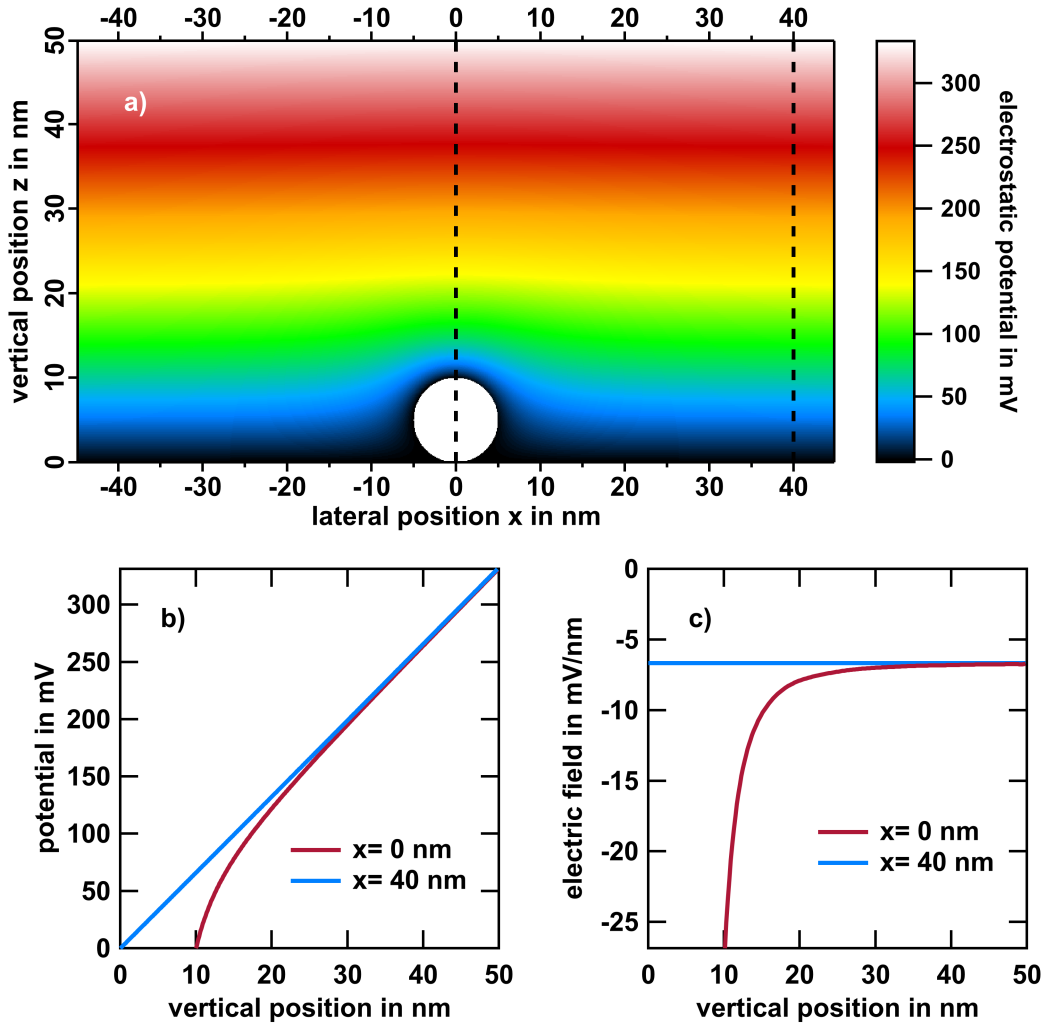

Figure 4.25: a) Map of the electrostatic potential in the vicinity of a metallic nanoparticle with 10 nm diameter in contact with a conducting surface (at $z = 0$) being 1.8 mm away from the PEEM extractor lens at a voltage of 12 kV. The presence of the cluster disturbs the homogeneous electric field distribution. The dashed lines indicate the position of the profiles of the electrostatic potentials (b) and the resulting electric fields (c). The red profiles correspond to the cluster position while the blue ones are 40 nm away.

6 University of Rostock, Institute of Physics, Physics of Surfaces and Interfaces, Albert-Einstein-Str. 23, 18059 Rostock, Germany

By estimating the cluster potential within Woods-Saxon approximation and superimposing with the extractor potential we can visualize the electron energy as a function of the distance to the surface as shown in Figure 4.26a. The black arrow indicates a possible tunneling channel. Under the assumption of a free electron and the approximation of a trapezoidal barrier as indicated in Figure 4.26b [164] we can roughly estimate the change in the tunneling probability by applying the Fowler-Nordheim equation [164]:

$$\exp\left(\frac{2\sqrt{2m_e}}{2\hbar q_0 F_{ox}}(\phi_1 - E_0)^{\frac{3}{2}}\right) \tag{4.3}$$

with m_e being the electron mass and $q_0 F_{ox} = \frac{\phi_2 - \phi_1}{x_2 - x_1}$ being the average slope of the potential in the trapezoidal barrier region and ϕ_1, ϕ_2 as sketched in Figure 4.26b. For an electron energy of $-50\,\mathrm{meV}$ relative to the vacuum level and an average electric field of $-15\,\mathrm{mV/nm}$ with the presence of the cluster and $-6.67\,\mathrm{mV/nm}$ without, the tunneling probability increases by more than two orders of magnitude. However, within this rough model the absolute probability remains still below one percent. This indicates that tunneling may occur due to the high extractor field and has a higher probability in the vicinity of the metallic nanoparticles, which in principle could lead to an apparently broader spectrum and an underestimation of the work function. Nevertheless, the states close to the vacuum energy need to be sufficiently occupied by laser excitation to make this process possible. Moreover, as mentioned before the effect of tunneling on planar surfaces has been calibrated by comparing to a known work function of a flat polycrystalline silver sample. To conclude, it is likely that tunneling due to high extractor fields occurs and broadens the kinetic energy spectrum. For a homogeneous electric field this has already been considered in the analyzer's work function. For rough structures a local field enhanced emission can occur and additionally broaden the spectrum which leads to an underestimation of the work function. Nevertheless, this effect will be extremely small compared to the instrumental energetic resolution of about 100 meV.

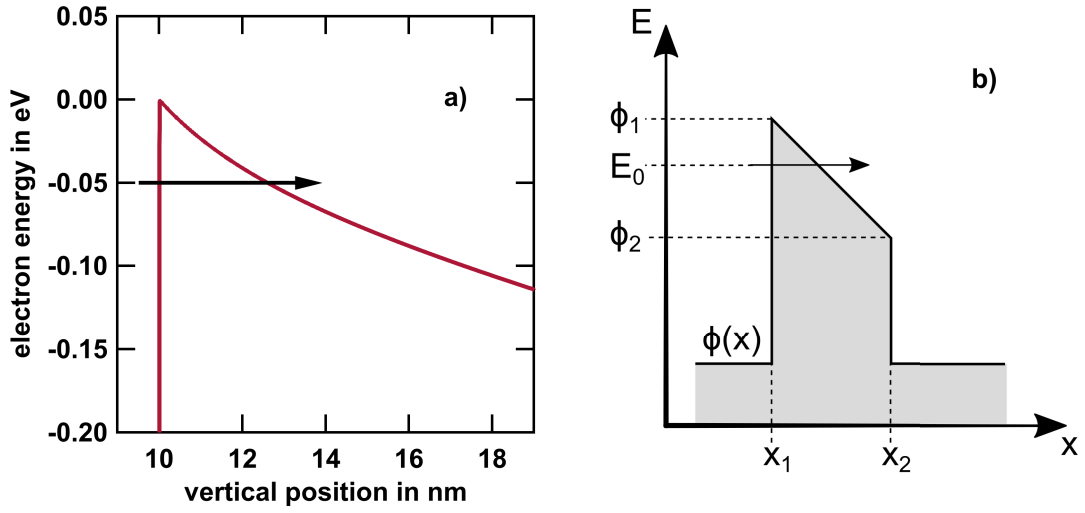

Figure 4.26: a) Superposition of the cluster potential in a Woods-Saxon approximation with a surface thickness parameter of 0.02 Å and a potential well depth of 11 eV [158] and the simulated field due to the extractor voltage at the cluster position (red line in Figure 4.25c). The black arrow indicates a possible channel for electron tunneling through the potential barrier. b) Schematic representation of a trapezoidal tunneling barrier with the nomenclature used in Equation 4.3. Adapted from [164].

Surface Photovoltage

In a photoemission experiment the absorption of photons not only results in an emission of photoelectrons, additionally the inner photoelectric effect occurs which is the excitation of a bound electron to a higher energetic level below the vacuum energy. On semiconductor surfaces exhibiting a band bending and therefore an electric field in the space charge region (SCR) at the surface (Figure 4.27a), the excited electrons in the conduction band and the remaining holes in the valence band become separated, and an additional electric field builds up in the opposite direction to the one in the SCR leading to a partial flattening of the bands (Figure 4.27b). This mechanism, known as surface photovoltage (SPV), changes the surface's potential and was first observed by Brattain in 1947 [165, 166]. At high illumination intensities the SPV can saturate, in this case the bands are completely flat and the electric field in the SCR has vanished. Therefore the generated electron-hole pairs will be no longer separated and no additional potential can build up (Figure 4.27c). For further information on SPV see [167].

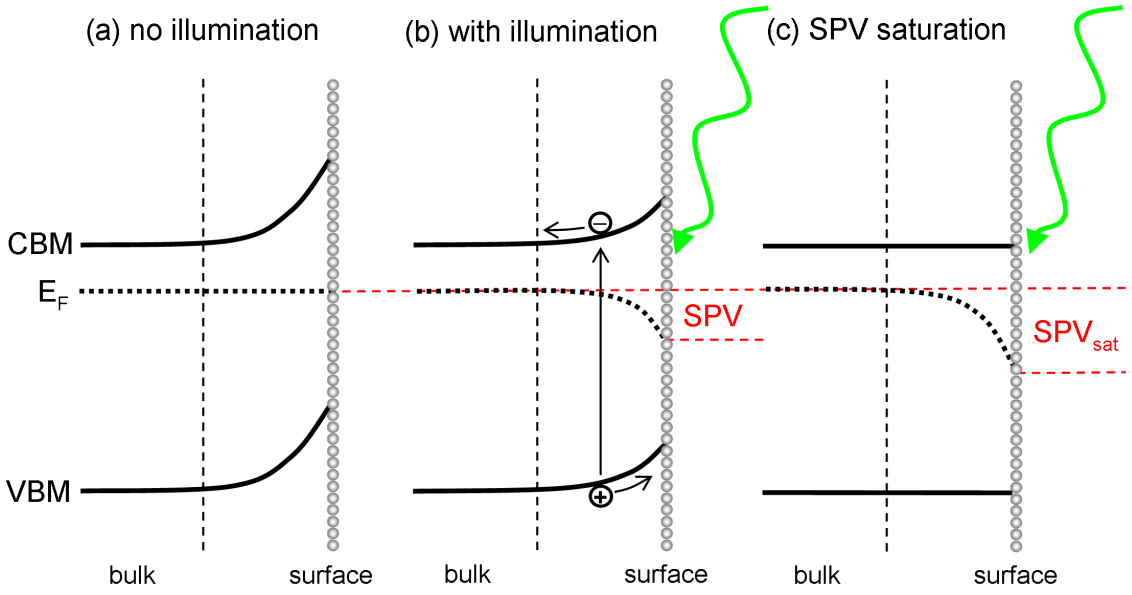

Figure 4.27: Schematic representation of the conduction band minimum (CBM), valence band maximum (VBM), and E_F development of a semiconductor from bulk to the surface a) without illumination b) with moderate illumination c) with high illumination intensity in saturation. The bands are plotted for an n-type semiconductor as used in this work. Figure from [111].

As we are using silicon as a substrate the formation of a SPV is expected for excitation with photon energies above the band gap[7] of 1.14 eV [168]. The changing surface potential can be seen as a shift of the Fermi level as illustrated in Figure 4.23. With increasing laser power the Fermi edge shifts towards higher binding energies which means that the emitted photoelectrons have less kinetic energy due to the reduced upward bending of the bands leading to a positive SPV attracting the electrons as illustrated in Figure 4.27b. In Figure 4.28 the shift of the Fermi edge is plotted as a function of the average laser power P for illumination with 360 nm (a) and 420 nm (b) wavelength, respectively. In a photoemission experiment the initial band bending (without illumination) cannot be measured directly because illumination is needed for a measurement. Therefore, the shift of the Fermi edge is offset to the SPV since the position at lowest intensities (SPV_0) is

7 This condition is necessary to directly create electron hole pairs for the formation of a super-bandgap SPV. By using less photon energy the formation of a sub-bandgap SPV can occur by trap assisted excitation processes [167]. For photon energies above the direct bandgap of 3.2 eV the absorption cross-section is strongly enhanced [144].

needed as a reference and corresponds to zero shift. To obtain a value the data was fitted according to Equation 4.4, which is commonly used for the analysis of power dependent SPVs without the offset SPV_0 [111, 169–172, KO-3].

$$SPV = A \ln(1 + B \cdot P) + SPV_0 \tag{4.4}$$

The parameters A and B are discussed in detail in [111, KO-3]. SPV_0 is needed due to the fact that we can only measure the SPV as a shift of a spectrum compared to a reference spectrum. Unfortunately we can not acquire a spectrum without illumination. Therefore the offset SPV_0 corrects for the non zero reference and by knowing the offset, the initial band conditions can be approximated and the SPV is determined (right axes in Figure 4.28).

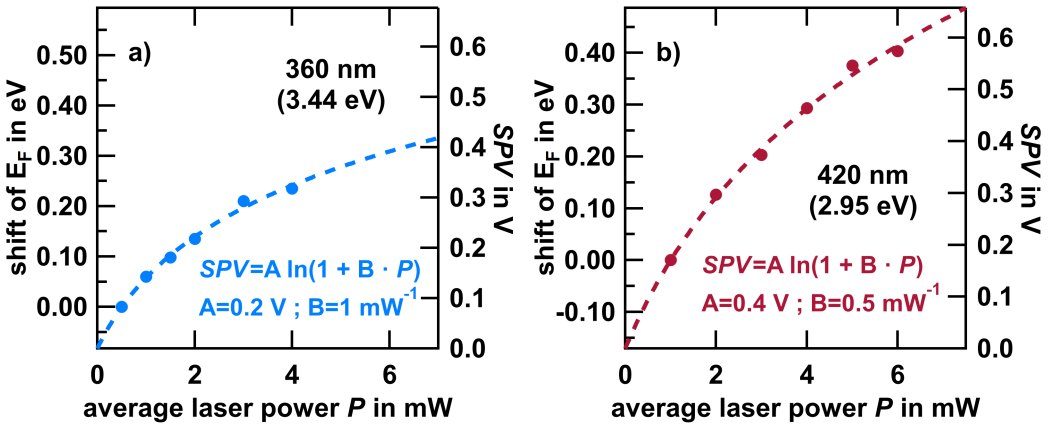

Figure 4.28: Shift of the Fermi level position (dots) as a function of the average laser power at a) 360 nm and b) 420 nm wavelength, respectively. The best fit according to Equation 4.4 is shown as dashed line and fit parameters are specified in the plots. The resulting SPV is plotted on the right axes.

The maximal SPV measured is ≈ 0.3 V for excitation with 360 nm wavelength and ≈ 0.55 V for 420 nm, respectively. A saturation is not obvious for both excitation wavelengths, therefore a comparison to literature is not straightforward since the values obtained, strongly dependent on the laser parameters such as spot size etc., which cannot be determined exactly. Nevertheless, the values are accordance with [173]. However, concerning the Fermi level pinning due to the surface states on Si(111)-(7x7) in between the bandgap a SPV of 0.6 V is reasonable as well.

To qualitatively explain the different evolution of the SPV for the two excitation wavelengths, we will have a look at the involved quantities. At any time we measure a temporal constant SPV we have a dynamic equilibrium between the photon induced generation of electron hole pairs G in the SCR[8] and their depletion R due to several effects, e. g. recombination, thermionic emission or tunneling, which can be expressed in a rate equation [167]

$$0 \stackrel{!}{=} \frac{\delta \Delta n}{\delta t} = G - R \tag{4.5}$$

with Δn being the density of electron-hole pairs. The generation rate $G'(z)$ at the distance z from the surface is

$$G'(z) = J_{Ph} \alpha e^{-\alpha z} \tag{4.6}$$

8 This is true as long as the system is not in saturation, since the charge carriers will no longer be separated.

with the J_{Ph} being the photon flux on the surface and the absorption coefficient α [167]. Therefore the number of generated electron-hole pairs in the SCR, which is approximately the Debye length z_D, can be expressed to be

$$G(z_D) = \int_0^{z_D} G'(z)\mathrm{d}z = J_{Ph}\left(1 - e^{-\alpha z_D}\right). \tag{4.7}$$

If we compare the properties of silicon for 360 nm with those at 420 nm the major difference is the absorption coefficient of $\alpha_{360\,nm} = 10.4 \cdot 10^5\,\mathrm{cm}^{-1}$ and $\alpha_{420\,nm} = 0.5 \cdot 10^5\,\mathrm{cm}^{-1}$ [113], respectively, due to the direct bandgap which can be excited below 385 nm wavelength [144] as schematically shown in Figure 4.29. Therefore the penetration depths α^{-1} are $\alpha^{-1}_{360\,nm} = 10\,\mathrm{nm}$ and $\alpha^{-1}_{420\,nm} = 190\,\mathrm{nm}$, respectively. The sample with a specific resistance of 0.01 Ωcm has a dopant concentration of $\rho_0 \approx 4 \cdot 10^{18}\,\mathrm{cm}^{-3}$. Using an approximative relation [174]

$$z_D \approx \sqrt{\frac{\epsilon_0 \epsilon_r k_b T}{e^2 \rho_0}} \tag{4.8}$$

the Debye length can be estimated to be $\approx 2\,\mathrm{nm}$. Hence, according to Equation 4.7, the amount of generated electron hole-pairs in the SCR is about 19 % (360 nm) and 1 % (420 nm) of the incoming photons J_{Ph}, respectively. Concerning the higher photon flux at larger wavelength at the same power and the different reflectivities due to the non-constant $\varepsilon(\lambda)$ in the wavelength regime, we obtain roughly 11 times more electron-hole pairs generated when exciting with 360 nm. Since the SPV depends on the electron-hole pair density we need to analyze both generation and recombination rates of charge carriers. We can divide the total recombination rate R into subprocesses R_i depending on the mechanisms of the recombination

$$R = \sum_i R_i = \sum_i \frac{\Delta n}{\tau_i} \tag{4.9}$$

with the lifetimes τ_i. The minority carrier lifetime for n-type silicon at room temperature with a doping concentration of $4 \cdot 10^{18}\,\mathrm{cm}^{-3}$ has been measured to be $\approx 0.2\,\mu\mathrm{s}$ [175]. However, this quantity has been obtained by exciting the electron just above the indirect bandgap (cf. Figure 4.29) hence a radiative recombination is forbidden due to momentum mismatch. For direct semiconductors the lifetime is orders of magnitude lower being typical in the ns regime [174], because of the additional radiative decay channel. By illuminating with 360 nm wavelength we start to excite the direct bandgap even in silicon, therefore radiative recombinations become possible in principle. Due to Equation 4.9 this additional decay channel would have a major influence which could explain the obtained measurement of SPV. In this case the increased absorption due to the excitation of the direct bandgap would be overcompensated by the reduced lifetime of the created electron-hole pairs leading to an effective reduction of the electron-hole pair density in the SCR and thus a lowered SPV.

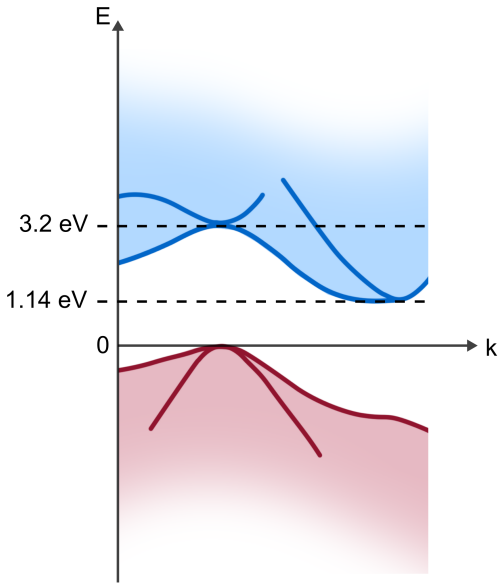

Figure 4.29: Simplified scheme of the silicon bulk band structure. Valence (red) and conduction (blue) bands are separated by an indirect band gap of 1.14 eV, the direct gap can be excited above 3.2 eV at the Γ point. Figure adapted from [144, 176].

Power Dependence

The development of a SPV has some consequences on the analysis of power dependent data as it was done in Figure 4.22. For the integrated evaluation of the order of the photoemission process as done in Figure 4.22a the shift of the spectra has no influence until they remain in the measured time-of-flight slot. Therefore the order $n = 2.07$ stays correct, implying that 2PPE is the dominant process. Figure 4.30a shows the SPV corrected data of those presented in Figure 4.22b. The dip at the Fermi edge disappears; instead, the order of the process approaches to $n = 3$ above the Fermi level. Below also a slightly increased value above $n = 2$ is noticeable. Approaching the secondary electron cutoff the value decreases marginally below $n = 2$ at the peak of the spectrum and spikes directly at the cutoff to a vale of $n = 3$.

To explain this behavior we have a look at Figure 4.30b where the photoelectron yield for excitation with 420 nm wavelength is shown as a function of E_{bin} and kinetic energy E_{kin} on a logarithmic scale. We can clearly identify the main spectrum originating from a 2PPE process as we have seen in Figure 4.22a in a kinetic energy range below ≈ 1.7 eV indicated with 2PPE ending at E_F(2PPE). While the binding energy axes is only valid for 2PPE processes, the kinetic energy is correct for arbitrary orders. On the logarithmic scale we can recognize electrons having higher kinetic energies which can be attributed to a 3PPE process as also observed in other studies [101, 177]. The additional kink at ≈ 5 eV, assigned to the Fermi edge of the 3PPE process, gives another piece of evidence for the appearance of this above threshold ionization (ATI). Moreover, the existence of this additional Fermi edge shifted by one photon energy is an indicator of the existence of a coherent triple excited surface plasmon as discussed on page 45 in the framework of the spectral shapes, and also been observed earlier [101, 177].[9]

To get a deeper insight of understanding the blue curve in Figure 4.30a we again split the signals into cluster and silicon signal. Figure 4.31 shows the spectra of the cluster (a)

9 To proof this statement one has to make sure that at least a part of these electrons originate from the nanoparticles which cannot be safely shown due to the high noise level in this range of the spectra.

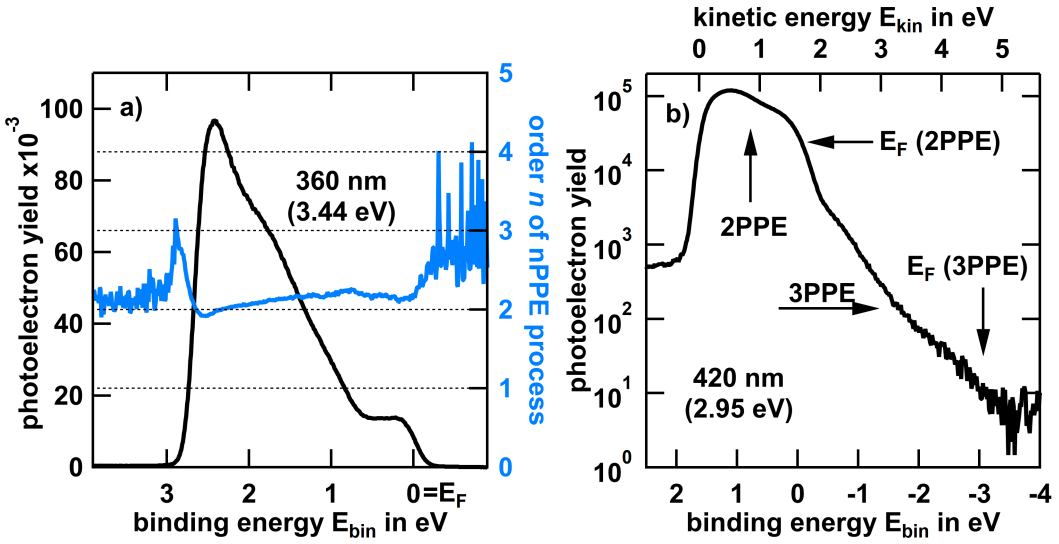

Figure 4.30: a) Same as in Figure 4.22 for the SPV corrected data. The blue curve, giving the order n of the nPPE process as a function of E_{bin}, shows a changed behavior especially at the edges of the spectra illustrated by the black curve. b) Representative photoelectron spectrum as a function of E_{bin} and E_{kin} for 420 nm excitation wavelength on a logarithmic scale with a specification of important regimes.

and the silicon signal (b) at an excitation wavelength of 360 nm with a laser power of 0.5 mW (black curve) and 4.0 mW (yellow curve), respectively. The photoelectron yields are normalized according to a 2PPE process. This means that for 3PPE the yellow curve is above the black and vice versa for one-photon photoemission (1PPE). The cluster signal shows a perfect agreement in the region of the Fermi edge where the photoelectrons were assigned to a simultaneous excitation due to the coherent decay of a doubly excited plasmon (see page 45). The secondary electron peak originating from sequential excitations through an intermediate state shows strong deviations from this conventional 2PPE behavior. In contrast, the silicon signal is in a good agreement over the whole spectral range with a tentatively increased 3PPE signal around $E_{\mathrm{bin}} \approx 1$ eV. Figure 4.32 shows the same for an excitation wavelength of 420 nm. The cluster signal has the same trend while for the silicon a clear enhancement around $E_{\mathrm{bin}} \approx 1$ eV is visible. This signal can be attributed to a 3PPE process from higher bound states which are available in the band structure [144]. For the nanoparticles the situation is not that clear. The normalized photoelectron yield indicates a process below 2nd order. For a conventional 1PPE the photon energy is not sufficient, therefore power dependent differences in the sequential 2PPE process are the most prominent candidates. In my opinion, the most probable scenario would be the following. Let us split the 2PPE process into a pump and a probe part. The latter just extracts photoelectrons out of the intermediate state, populated by the pump photons, with a certain kinetic energy distribution. If we consider the intermediate state population having the identical energy distribution for both excitation powers we would end at the same photoelectron spectrum as probed by the pump pulse disregarding the yield scaling with P^2. Since the intermediate state undergoes relaxation processes this would be the case if the mean energy loss per electron stays the same independent of the laser power. As we know that electron-electron scattering is a major decay mechanism the probability for a collision increases with the amount of excited electrons in the intermediate state. Hence, the average energy loss per electron increases with the laser power shifting the energy distribution in the intermediate state towards higher binding energies. As a consequence a slightly larger part of these hot electrons will not be detected since they cannot overcome the work function barrier. Another possibility

would be a saturation of the intermediate state which is considered to be highly unlikely since in other experiments having orders of magnitude higher photon flux a saturation was not observed [177].

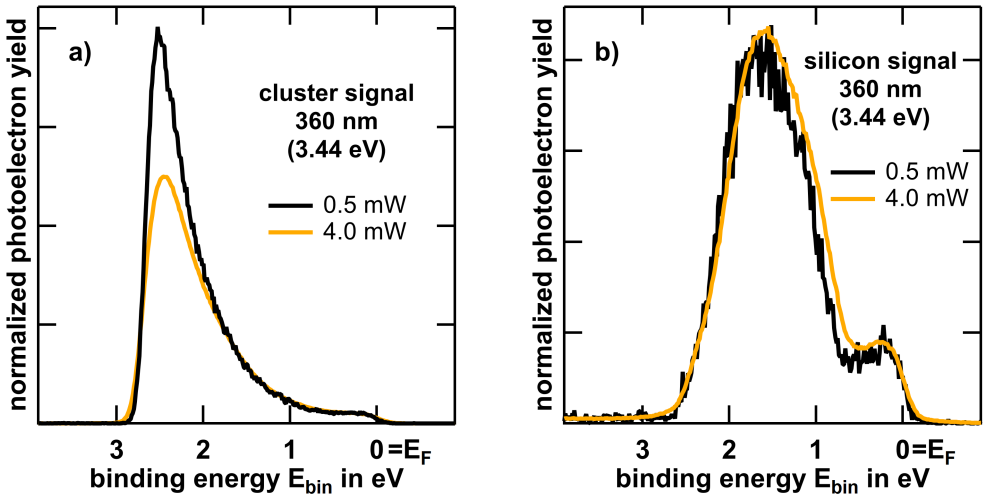

Figure 4.31: Photoelectron yield of a) the cluster signal and b) the silicon signal as a function of E_{bin} for 0.5 (black) and 4.0 mW (yellow) at 360 nm excitation wavelength. Spectra were normalized according to a 2PPE process. The cluster signal in a) shows clear deviations from the quadratic power dependence at higher binding energies while for the silicon signal differences are less obvious.

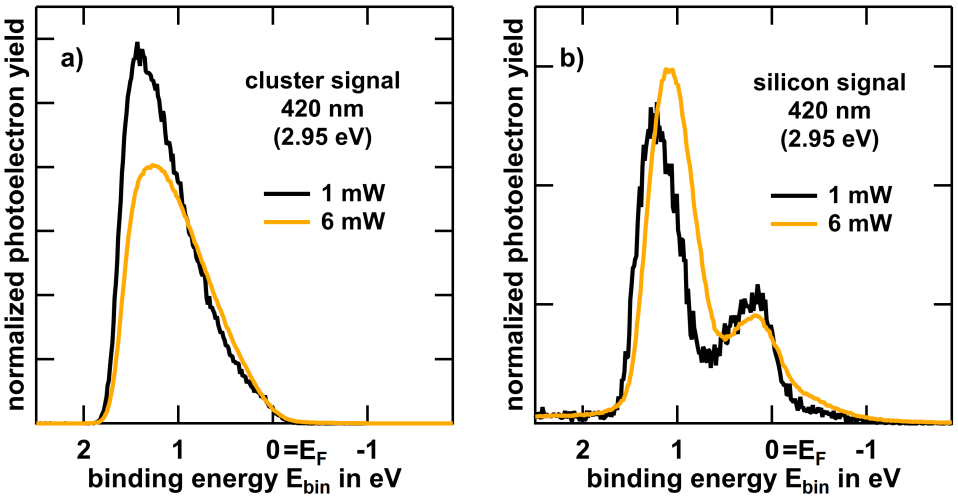

Figure 4.32: Same as Figure 4.31 for 1 (black) and 6 mW (yellow) at 420 nm excitation wavelength. The cluster signal in a) is similar to the one shown in Figure 4.31a), while for the silicon signal in b) pronounced deviations from the power law occur.

4.3 DISTRIBUTION OF ELECTRON EMISSION ANGLES

For all measurements so far, the PEEM was used in the spatially resolving mode. In addition, one can switch to an angular resolving mode, so called k-space mode. In this setup any spatial information in the FoV is dropped for the benefit of getting the angular distribution of the emitted photoelectrons, which is comparable to angle-resolved photoemission spectroscopy (ARPES). The result is a three dimensional dataset with the momenta k_x, k_y, and the kinetic energy E_{kin} for each electron. The collectivity of photoemitted electrons form a paraboloid where certain cuts can be analyzed.

Due to the size restrictions in this work a part of the measurements is shown in the Appendix A.7. Some interesting features are visible which could be connected to real space by comparing the spectra obtained in both k- and real space measurements. Furthermore, a limited spatial resolution can be reached using an aperture to restrict electron emission to a certain location which can be selected in spatially resolved mode. Especially the Fermi surfaces show that the preferred emission direction can be controlled by the polarization of the excitation source.

4.4 CONCLUSION

In this chapter the impact of the local environment on the optically excited plasmon resonance of single silver nanoparticles was studied. Clean silver nanoparticles without organic ligands are produced in a gas aggregation cluster source, subsequently size-selected and soft landed onto silicon with a native oxide layer and onto atomically well-defined Si(111)-(7x7), respectively. Plasmon resonance spectra of a large number of individual particles down to about 10 nm in height are obtained using excitation spectroscopy in a 2PPE-PEEM experiment. A wide range of different resonance energies between 2.7 eV and 3.4 eV were observed which is only partly due to size variations as concluded from correlative AFM measurements. Despite the large scattering of individual plasmon energies this data are compatible with the size-dependent trend predicted by classical Mie theory. While on oxidized silicon a single well-defined peak is measured, it splits into two clearly distinguishable resonances on pristine silicon. Generalized Mie Calculations performed by our collaboration partner Jean Lermé revealed that such mode splitting is a consequence of strong coupling to the silicon substrate, giving rise to the formation of image dipoles and hence quadrupole moment excitations due to the large relative permittivity of pristine silicon which allows strong field inhomogeneities to develop near the surface. This scenario is supported by statistical analyses of many single-object spectra revealing that the variation of plasmon energies is even increasing on Si(111)-(7x7) compared to the oxidized sample (A).

The results demonstrate that plasmonic properties of small nanoparticles in the size range < 20 nm need to be addressed individually, since electronic coupling to the substrate, presumably strongly dependent on the detailed morphology and local environment, greatly affect plasmon energetics.

In principle, this opens perspectives to detect the particles' local environment on the atomic scale: the red-shift of the dipolar plasmon mode as well as the intensity ratio between quadrupole and dipole modes (see Figure 4.10a, 4.11a) are highly sensitive on the effective coupling distance between particle and polarizable substrate [34, 114], such that variations of the order of one Ångström can be easily detected. Provided that particle preparation and deposition may be highly controlled in future (e.g. by self-assembly approaches), or that plasmonic scanning tips can be employed, the findings open the perspective of efficient detection of the dielectric and geometric configuration at particle-substrate interfaces with high spatial resolution. One example is the development of

ultraprecise plasmonic rulers for characterizing thin spacer layers such as those employed in the semiconductor industry.

By utilizing electron spectroscopy by means of ToF-PEEM more fundamental mechanisms can be addressed. We have seen that the dominant emission process from the silver nanoparticles is via a relaxated plasmonic intermediate state leading to the main emission peak always located at the secondary electron cutoff. However, also the decay of a coherent multi-exciton states was shown which demonstrates the presence of an efficient Landau damping of the collective mode.

In addition, the possibility of utilizing the PEEM to measure SPVs was shown. Recently, spatially resolved SPV measurements were performed by Katharina Engster. First results unraveled a local enhancement of the photovoltage in the direct vicinity of silver nanoparticles on a semiconducting Si(100)-p(2x1) surface [MT-3, KO-5].

TETRACENE AND SILVER NANOPARTICLE HYBRID SYSTEM

5

In the previous chapter we investigated the optical properties of supported silver nanoparticles. Amongst others, plasmon resonances have been characterized and the local field enhancement in the vicinity of the clusters was determined. With this knowledge we can now utilize the nanoparticles' properties to locally create excitons in organic semiconductors. For this purpose, tetracene is a promising candidate. Light absorption around the wavelengths of typical silver nanoparticle plasmon resonances leads to an efficient singlet fission [9, 10]. Hence, a high triplet exciton density could possibly be generated. In contrast to singlet excitons, having a shorter lifetime but a higher diffusion constant, there is no fundamental physical limit for the diffusion lengths of triplet excitons, since both quantities can be varied independently [62]. Exciton migration was already observed in macroscopic crystals as well as thin films over several hundred nanometers [9].

First studies on the morphology and fluorescence of vacuum evaporated tetracene have been done in the framework of the master's thesis by Christian Völkner [MT-2]. Part of these results will be presented in the first section of this chapter. In the second part we will mainly focus on PEEM studies of the hybrid system of size selected silver nanoparticles on a tetracene film evaporated onto a silicon substrate. Here, population blinking as well as a coupling between cluster and molecules was observed and excited state lifetimes were determined in a pump-probe experiment. To gain knowledge on the involved states optical measurements by means of FLIM were performed on larger tetracene crystals prepared by drop casting. Afterwards the results will be discussed.

5.1 MORPHOLOGY OF EVAPORATED TETRACENE

Attaining detailed information about the morphology of the evaporated tetracene films is not only crucial for optimizing and understanding the deposition parameters. Moreover, the electronic and exciton transport properties essentially depend on the nanoscale morphology [9]. Therefore, we initially characterize the tetracene structures obtained on silicon after evaporation.

For preparing tetracene films the home-built vacuum evaporator described in Section 3.2.3 was used. Figure 5.1 shows two ex-situ AFM images of a sample directly after the deposition of tetracene for 29 min at an evaporator temperature of 400 K on natively oxidized silicon at room temperature. The $40 \times 40\,\mu m^2$ overview image (Figure 5.1a) shows aggregates forming dendritic structures with lateral dimensions of $\approx 10\,\mu m$ and heights of $5 - 20\,nm$. The outer bounds of the dendritic structures are often terminated by higher dot like ends of the individual branches. The isolated aggregate in the center of the image has a height of $\approx 10\,nm$ and is shown in Figure 5.1b in more detail. Beside this, dendritic structures up to 10 nm high islands are visible with lateral dimensions of several μm^2. On top of these islands as well as on the underlying structure are dot like arrangements with diameters of some 10 nm and heights of $1 - 5\,nm$.

For PEEM measurements a sample was prepared by the same procedure and checked in optical as well as fluorescence microscopy. A similar morphology was observed. Figure 5.2 shows an AFM image (a) together with a line profile (b) subsequent to the comprehensive PEEM measurements. Neither dendritic structures nor islands were visible. Instead, dot-like structures are arranged in chains enclosing areas of several μm^2. In the center a hole in the otherwise closed layer was found. The white dashed line marks the origin of the line profile shown in b) indicating a depth of around 1 nm.

Reasons for this obvious change of morphology will be discussed in Section 5.4.

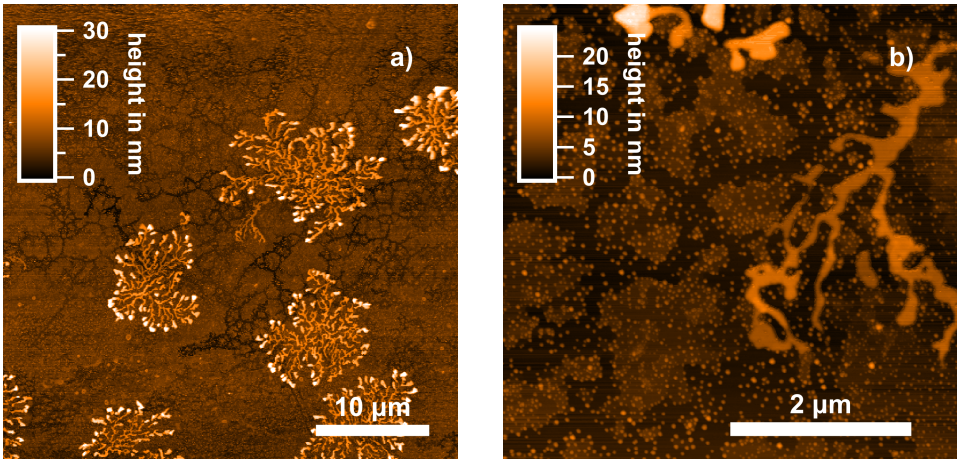

Figure 5.1: AFM images of vacuum evaporated tetracene on natively oxidized silicon. Dendritic structures were formed as observed in a). The region in between those arrangements is shown in b).

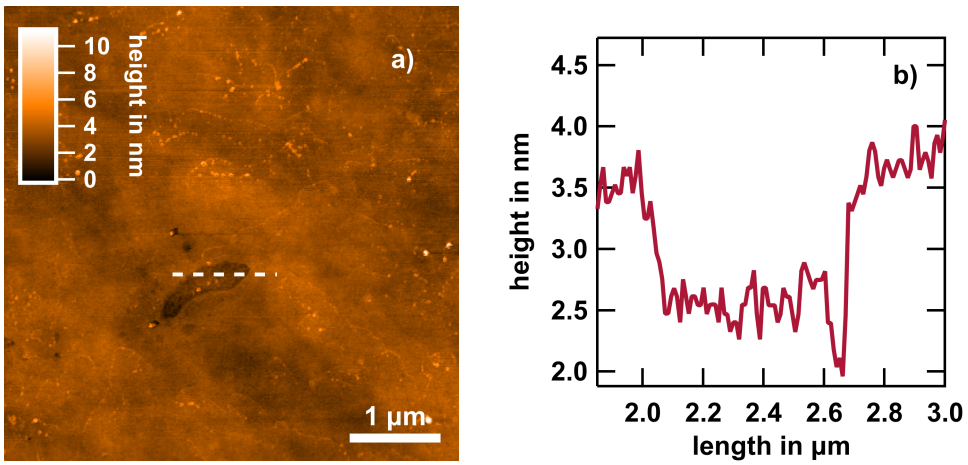

Figure 5.2: AFM image of a tetracene sample subsequent to the PEEM measurements. Some few nanometers high spheres arranged in chains were observed. In addition, a hole in the otherwise flat surface was found. The dashed white line marks the line profile position shown in b) indicating an indentation of around 1 nm.

Fluorescence

The fluorescence of a freshly evaporated film can be seen by naked eye as a greenish shimmer on the sample. Figure 5.3 shows a part of a fluorescence image of the sample shown in Figure 5.1. One clearly recognizes the dendritic structures having an increased signal compared to the background. The fluorescence yield of the dendrites is enhanced at the border of the structures.

Fluorescence of the sample used for PEEM measurements was similar prior to those investigations and was as well visible by naked eye. Subsequent to the studies no luminescence was detectable anymore.

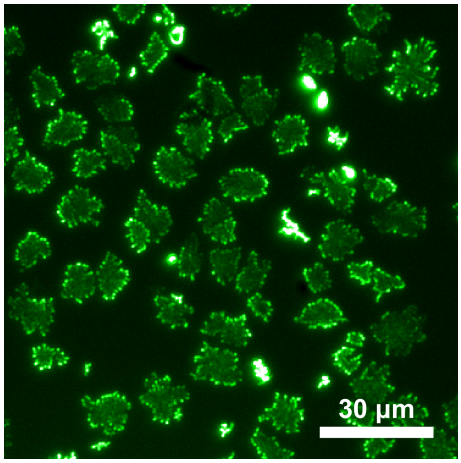

Figure 5.3: Part of a fluorescence image showing dendritic tetracene islands. The green colorscale was used to pronounce the detected fluorescence which has a wavelength above 515 nm due to the used GFP filtercube. The measurement was done on the same sample as shown in Figure 5.1.

5.2 SILVER NANOPARTICLES ON TETRACENE FILMS

We now focus on the excitations in tetracene after illumination with light either from the far-field of a laser or the plasmonically enhanced near-field from silver nanoparticles. For discrimination of different excitations and their spatial as well as temporal evolution, PEEM is a promising tool as it combines optical excitations with the advantages of electron microscopy, i. e. a high spatial resolution and the ability of probing non-radiating states.

For these investigations a tetracene sample on natively oxidized silicon was prepared as described in Section 5.1. After evaporation and control measurements in a fluorescence microscope the sample was transferred through air into the PEEM chamber. Here, mass selected silver clusters were deposited at a quadrupole voltage of 1.5 kV leading to an average cluster height of ≈ 15 nm as verified by AFM subsequent to PEEM measurements. The nanoparticle density is around $0.07\,\mu m^{-2}$. Investigations on this sample will give information for both the tetracene film on silicon and the hybrid system consisting of silver nanoparticles on this film assuming that a possible coupling disappears after some micrometer distance which could be easily resolved.

To access the energetics of the system we will start to illuminate the sample at different wavelengths while the dynamics will be primarily studied by using pulsed laser sources. Under certain excitations a temporal fluctuating photoemission yield is observed which will be addressed in Section 5.2.3, followed by a detailed study of the coupling between nanoparticles and tetracene investigated by a multi laser excitation approach. To access lifetimes of the involved molecular states pump-probe measurements have been done which are presented at the end of this section.

5.2.1 APPEARANCE AT DIFFERENT WAVELENGTHS

Figure 5.4a shows a total photoelectron yield PEEM image under cw illumination with a wavelength of 266 nm (4.66 eV). Bright dots are visible which are attributed to the silver nanoparticles all of them having a comparable intensity. The background shows a relative homogeneous photoemission intensity with cloudy structures as we have seen in AFM (Figure 5.1) and Fluorescence Microscopy (Figure 5.3) of tetracene as well. By changing the illumination intensity the order n of the photoemission process was determined to be equal to 1. Also the spatially resolved map of n (see Appendix A.6) shows no significant variations. In Figure 5.4b exactly the same sample position is shown under cw excitation with 405 nm wavelength (3.06 eV). Now the tetracene film appears grainy while the nanoparticles disappear completely. Please note that the bright dots do not correspond to the cluster positions, hence these are attributed to the tetracene. Concerning the order n of the photoemission process an averaged value of 1.8 is observed. The map (see Appendix A.6) shows highly fluctuating regions changing between 1PPE, 2PPE and even 3PPE with typical feature sizes on the order of those of the bright dots.

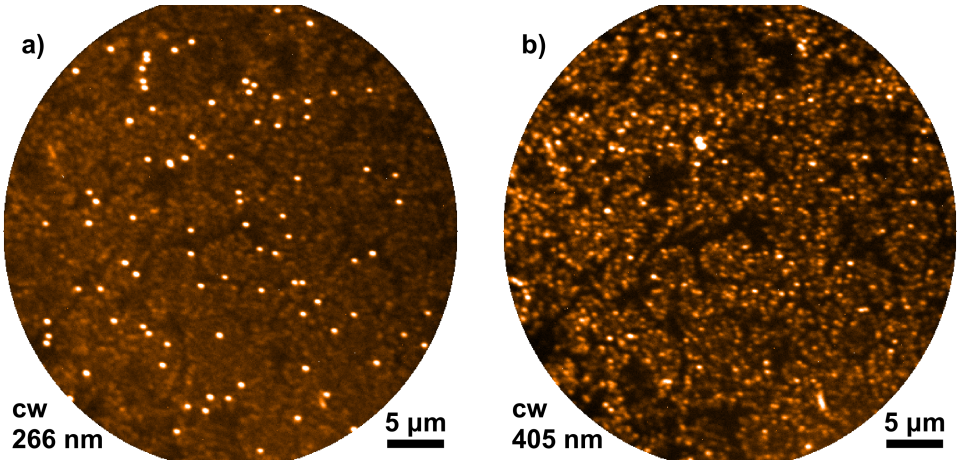

Figure 5.4: PEEM images (field of view: 40 µm) of evaporated tetracene on natively oxidized silicon with silver nanoparticles deposited subsequently in vacuum. In a) illumination was done with a cw laser at 266 nm wavelength. The bright dots are attributed to the nanoparticles. The same area under cw 405 nm illumination is shown in b), where clusters are invisible. Brighter colors correspond to higher photoelectron yield. See text for details.

We can now compare the cw illumination with pulsed fs laser excitation at similar wavelengths as shown in Figure 5.5. Using 266 nm wavelength (4.66 eV) (a) the tetracene appears more homogeneous compared to cw illumination while the nanoparticles are still visible. The averaged photoemission order was determined to be $n = 0.76$ indicating that 1PPE is still the dominating process. Deviations will be discussed in Section 5.4. For fs excitation at 400 nm wavelength (3.1 eV) (b) the grainy tetracene film at cw illumination appears homogeneous. Moreover, the invisible nanoparticles are clearly visible under fs illumination showing varying photoemission yield which is attributed to differences of the plasmon resonances as discussed in Chapter 4.1. The order n is found be 2.3, therefore 2PPE processes are dominating.

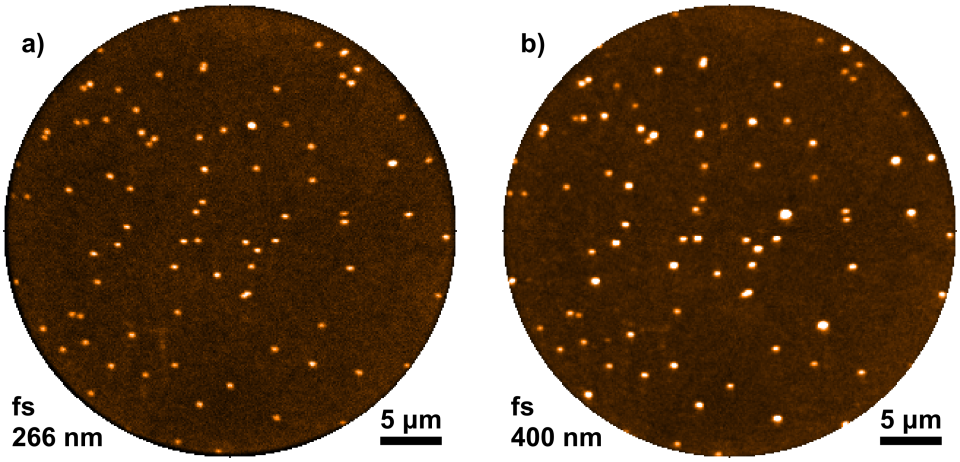

Figure 5.5: PEEM images (field of view: 37 µm) of the same area using fs laser illumination with a) 266 nm and b) 400 nm wavelength, respectively.

5.2.2 ELECTRON SPECTRA

In addition to the properties derived from the photoemission contrast in the total yield PEEM images, the ToF spectra contain valuable information as well. Figure 5.6 shows the photoelectron yield (black curves) as a function of E_{kin} and E_{bin} for illumination with 266 nm wavelength (4.66 eV) (a) and 400 nm (3.1 eV) (b). By selecting certain areas in the spatially resolved spectra, the tetracene signal (red curves) was distinguished from the cluster signal (blue curves). In the case of excitation with 266 nm wavelength we observe a main peak at low kinetic energies followed by the 1PPE Fermi edge, which is used as zero reference for the binding energy. At higher kinetic energies further distributions from higher order processes are visible. Differences between cluster and tetracene spectra are slightly visible in the shape of the main peak and the position of the high energy cutoff. At illumination with 400 nm wavelength (Figure 5.6b) the spectra primarily consist of one peak which is attributed to the 2PPE signal and is broader compared to the main peak in a). Again the shape of the spectra differs from the cluster compared to the tetracene signal. The spectra will be discussed in detail on Page 72, including an assignment of the involved states.

5.2.3 BLINKING & BLEACHING

When acquiring two PEEM images under identical experimental conditions, one usually expects two indistinguishable data sets apart from minor statistical fluctuations. Especially in photoluminescence experiments with fluorophores or colloidal quantum dots exceptions are well known, such as blinking and bleaching. Blinking describes a fluctuation of the fluorescence signal where the decay channels switch between radiative and non-radiative pathways in a non-ergodic behavior [178, 179]. Whereas bleaching is usually referred to be a chemical change leading to a lowered fluorescence yield. Here, similar behaviors compared to blinking are observed in photoemission using cw illumination with a wavelength of 405 nm. Figure 5.7 shows the evolution of the total photoelectron yield for a FoV of 28.2 µm for 200 measurements with an exposure time of 30 s for each one. During this survey the laser was continuously focused on the sample and was not blocked or deactivated in between two measurements. A decrease of the photoelectron yield over time is visible while its slope is steeper in the first twenty minutes compared to the latter decrease. After protecting the sample from the laser

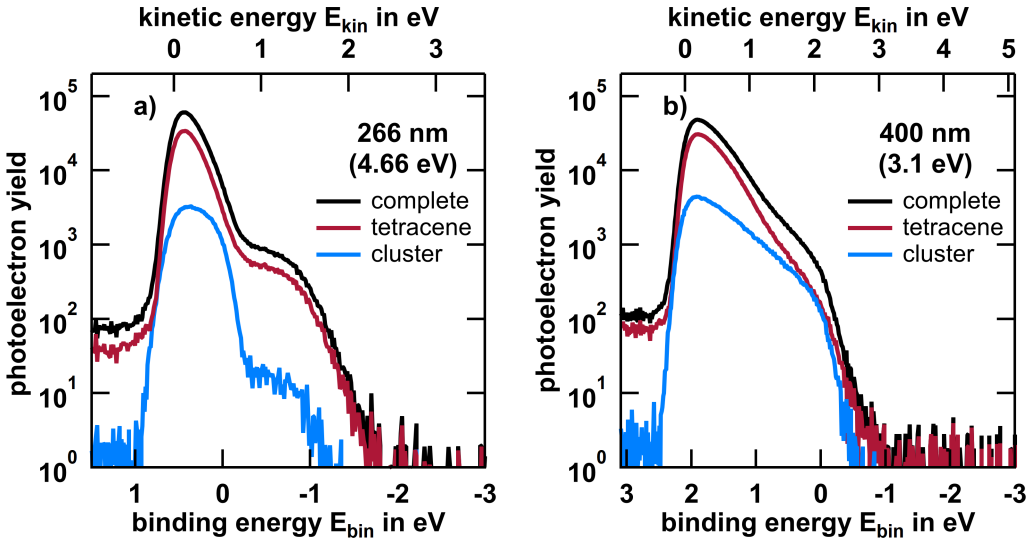

Figure 5.6: Photoelectron yield as function of E_{bin} and E_{kin} for a) fs 266 nm wavelength and b) fs 400 nm illumination, respectively. The black curves show the integrated yields over the images shown in Figure 5.5 while the other curves are integrated only over areas without clusters (red) and with clusters (blue).

radiation the original photoelectron yield will recover within several minutes. Hence, measurement series are not severely affected by this effect because the laser was always blocked between acquisition of two images. In addition to the global trend of a decrease in photoelectron yield, minor fluctuations are visible which partly could be statistical, but the spatially resolved analysis shown in Figure 5.8 reveals another origin.

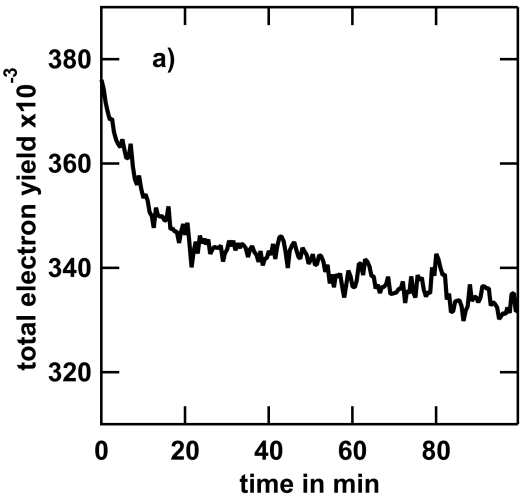

Figure 5.7: Time trace of the total electron yield at illumination with a 405 nm cw laser at constant laser intensity.

In a) the time averaged PEEM image is displayed showing the grainy tetracene structure already noticed in Figure 5.4b. By taking a closer look on the 200 individual images one will recognize sudden changes in intensity at certain positions. The time traces of the exemplarily selected areas are shown in b). The blue curve reveals a single strong spike in the photoelectron yield while the area is "dark" for the most time. In contrast, the yellow curve shows a permanent medium yield leading to a strong signal in the averaged image a). The green trace shows two short, consecutive electron pulses while the red one exhibits broader pulses with less photoelectron yield.

These observations are similar to fluorescence bleaching and blinking but the physical origin of the obtained signal must be different. Hence, the measurements can not be directly compared and will be discussed in more detail on Page 74.

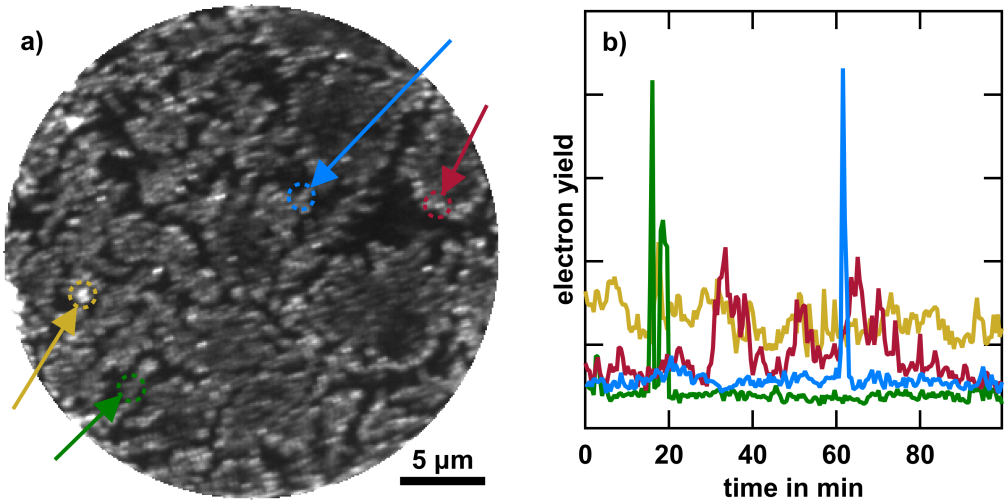

Figure 5.8: a) Averaged PEEM image (FoV: 28.2 µm) at illumination with a 405 nm cw laser over a time of 100 min. The colored arrows indicate the positions of areas where the time traces are shown in b).

5.2.4 COUPLING ENHANCEMENT

To access possible coupling phenomena between molecular aggregates and a nanoparticle's near-field, we try to separate the plasmonic excitation from the detection via photoemission by using a second laser simultaneously. After acquisition of an image with cw illumination at 405 nm or fs excitation with 266 nm wavelength, the total photoelectron yields Y_{cw405} and Y_{fs266} are obtained. Illuminating the sample with both lasers simultaneously gives $Y_{\mathrm{fs266\&cw405}}$. For all performed measurements $Y_{\mathrm{fs266\&cw405}}$ was always larger than the sum of Y_{cw405} and Y_{fs266}. This even holds if $Y_{\mathrm{cw405}} = 0$ for a low but finite laser power P_{cw405}. Therefore an additional photoelectron yield ΔY is defined as follows

$$\Delta Y = Y_{\mathrm{fs266\&cw405}} - (Y_{\mathrm{cw405}} + Y_{\mathrm{fs266}}) \quad . \tag{5.1}$$

To characterize the influence on populating a state or just probing the sample of the individual lasers the power dependence of ΔY is analyzed by holding one laser constant and varying the power of the second one and vice versa. The results are summarized in Figure 5.9. For $P_{\mathrm{cw405}} = 0.33\,\mathrm{mW} = const$ we obtain an exponent of $n_{\mathrm{fs266}} = 0.91$ in the $\Delta Y \propto {P_{\mathrm{fs266}}}^{n_{\mathrm{fs266}}}$ power law (see Figure 5.9a), and for $P_{\mathrm{fs266}} = 0.2\,\mathrm{mW} = const$ we obtain an exponent of $n_{\mathrm{cw405}} = 0.5$ (see Figure 5.9b), respectively. The meaning of these exponents will be discussed later in context of the triplet state population.

We can now take a deeper look into the spatial and energetic properties. Figure 5.10a shows a total electron yield PEEM image under simultaneous illumination with fs laser at 266 nm wavelength (4.66 eV) and cw at 405 nm (3.06 eV). The ratio of the laser intensities is adjusted in a way that the majority of electrons are photoemitted by absorbing a 4.66 eV photon from the femtosecond pulse. This can be seen as well in b) where the total photoelectron yield is plotted on a logarithmic scale versus E_{kin}. The green curve represents the yield observed for cw 405 nm illumination only. Due to the continuously arriving photons, a constant yield over time and therefore an apparently flat spectrum is obtained. In contrast, the amount of photoelectrons detected by illuminating solely

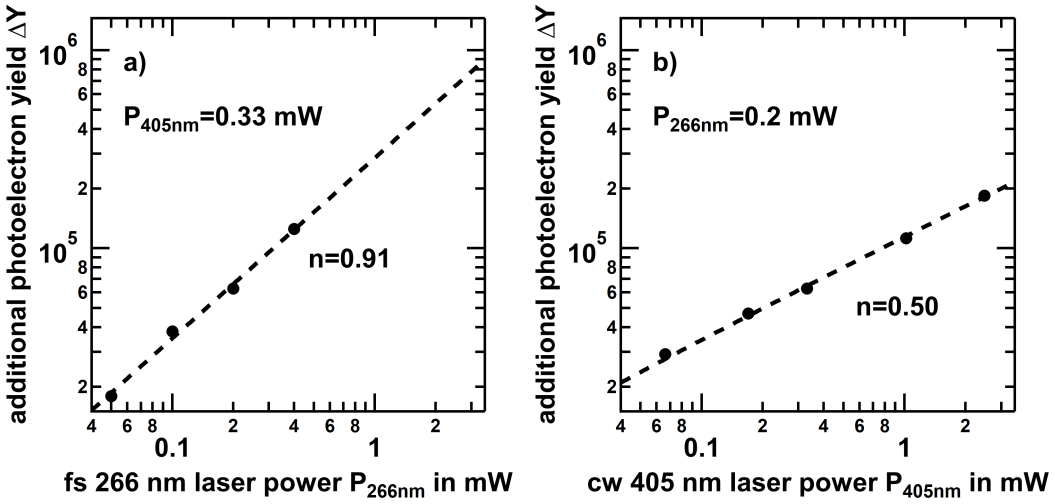

Figure 5.9: Additional photoelectron yield ΔY as a function of a) P_{266nm} at constant P_{405nm} and b) P_{405nm} at constant P_{266nm} on a double logarithmic scale. The different orders n of the photoemission give further information on the nature of the process. See text for details.

with fs pulses at 266 nm is much higher and shows a clear signature (red curve) as we already have seen in Figure 5.6a. The black curve in Figure 5.10b representing the the total photoelectron yield at simultaneous illumination with both lasers clearly shows that the additional counts ΔY are not equally distributed in energy, instead they show a peak around 0.5 eV as also shown in d) on a linear scale. The spatial distribution of ΔY is shown in c) where blue color represents additional measured electrons at simultaneous illumination while red means less counts compared to the sum of the individual excitations. We observe a homogeneous bluish background with some dot like areas with more intensity at the cluster positions observed in a). In addition, the bright spot in a) shows a red signature in the ΔY image.

All in all, we can conclude that the simultaneous illumination leads to additional photoelectrons all over the tetracene. In the vicinity of the silver nanoparticles this yield seems to be increased or not affected for most cases. In rare exceptions the number of photoelectrons might be decreased.

5.2.5 EXCITON LIFETIMES

In the last section we analyzed ΔY using both a cw and a pulsed fs laser thus we only observed long-term averaged information on the temporal evolution. To access the short-term dynamics we now want to investigate this time dependence in a pump probe like setup. Since ΔY has only been obtained by using 405 nm wavelength for excitation we need to use this photon energy in a pulsed way. However, using fs laser pulses at this wavelength will crucially change the photoemission process as we have seen in Figure 5.5b compared to 5.4b. Hence, an electronically pulsed diode laser will be used. In a first benchmark experiment the time range of interest will be determined. Therefore a cw laser with 266 nm wavelength will continuously probe the sample which will be observed temporally resolved with the DLD in a maximum time frame of 40 µs. In addition, the pulsed 405 nm diode will be operated with pulse lengths of 300 ns and a repetition rate of 1 MHz and below. The observed yield showed a significant amount of ΔY even after several µs. Nevertheless, this direct recording of the decay using the DLD as "movie camera" seems not to be sufficient for estimating quantitative lifetimes since

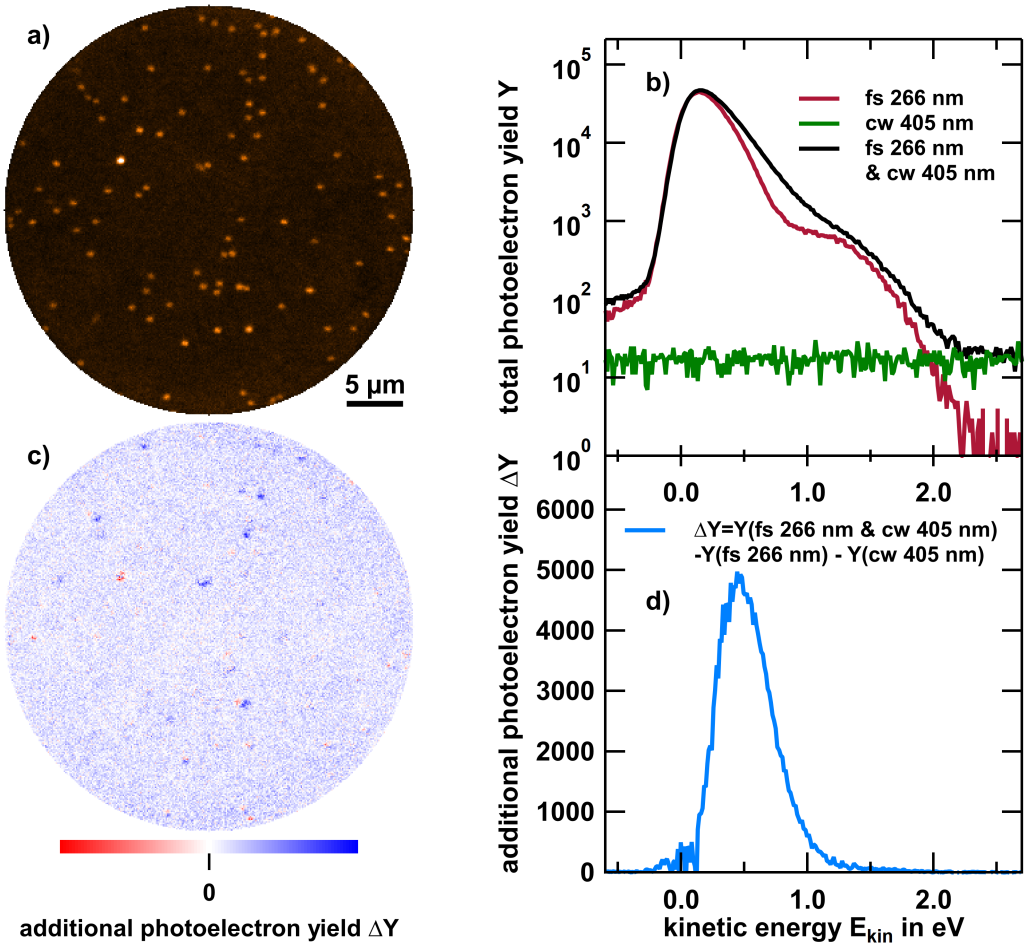

Figure 5.10: a) PEEM image (FoV: 37 µm) at illumination with a 266 nm fs laser for identification of cluster positions on tetracene. b) Photoelectron yield as a function of E_{kin} integrated over the area shown in a) on a logarithmic scale. The red curve represents the electrons acquired with fs 266 nm illumination only, while for cw laser excitation at 405 nm a constant signal, illustrated by the green curve, was measured. The black curve represents a simultaneous measurement with both lasers. c) Spatially resolved additional photoelectron yield ΔY, which is the difference of the simultaneous measurement with both lasers and the sum of two separate acquisitions. Additional counts are blue while missing counts in the simultaneous measurement are plotted red. d) ΔY as a function of E_{kin} showing a peak rising at the simultaneous illumination.

the detection and excitation are not independent for tetracene. Hence, the continuous probing distorts the determination of lifetimes. Therefore, the probing has also been done with pulses at certain delays to stroboscopically determine the temporal evolution of ΔY. For a detailed description of the used pump probe setup and the extraction of ΔY see Appendix A.8.

In Figure 5.11 the obtained temporal evolution of ΔY is plotted as a function of the delay between the two pulses. In a) a 2 µs pump pulse was used followed by a 1 µs probe pulse with a repetition rate of 10 kHz. A double exponential fit leads to lifetimes of 0.5 µs and ≈ 10 µs. For an increased time resolution both pulses were shortened to 0.1 µs at a repetition rate of 20 kHz (b). Here a triple exponential decay was necessary to fit the obtained data. In addition to 0.5 µs and a long decay time of ≈ 25 µs a much shorter lifetime of 0.1 µs was obtained. The measurements will be compared to optically obtained data by means of FLIM in the following section. The meaning of the individual decay times and the use of alternative fit functions will be discussed in section 5.4.

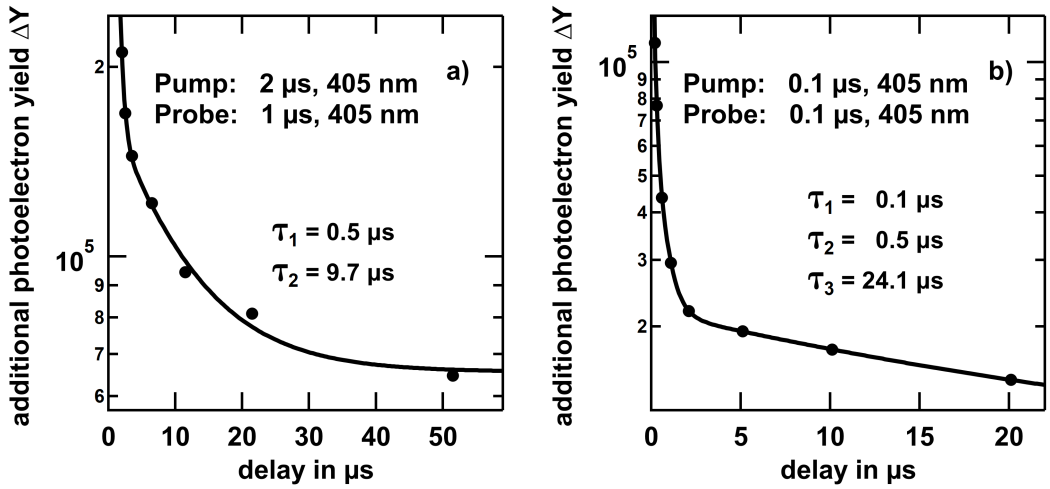

Figure 5.11: a) ΔY as a function of the pump-probe delay for illumination with an electronically pulsed diode laser with 405 nm wavelength and 2 µs pump pulse followed by a 1 µs probe pulse. Two decay times of around half and ten microseconds have been determined in a double exponential decay. b) Same as a) for 100 ns pulses. The triple exponential fit leads to ≈ 0.1, 0.5 and 25 µs decay times.

5.3 FLUORESCENCE LIFETIME IMAGING

Optically studied fluorescence lifetimes have shown to give complementary information with part of the excited state dynamics observed in PEEM due to the radiative population decay [KO-2]. To access possible dynamics on a ps time scale, a new sample with larger crystals was analyzed by FLIM in collaboration with Chris Rehhagen[1] using a PicoQuant MicroTime200 at an excitation wavelength of 445 nm. The sample was prepared by dropcasting a 5 µl droplet of a $9 \cdot 10^{-4}$ M solution of tetracene dissolved in toluene on a Menzelglass microscope slide. Aggregates with a lateral dimension of several tens micrometer as well as smaller aggregates were formed as can be seen in the FLIM images in the insets of Figure 5.12. The blue marked regions show the positions used for the following measurements. The objects in the left image will be referred to as

1 University of Rostock, Institute of Physics, Dynamics of Molecular Systems, Albert-Einstein-Str. 23, 18059 Rostock, Germany

large crystal while the right image shows the region selected for the analysis of smaller aggregates consisting of needle like structures. The black curve in Figure 5.12 shows the time dependent fluorescence yield obtained at an excitation repetition rate of 1 MHz and a laser power P_{FLIM} of 0.02 µW. After a rapid decay in the first tens of nanoseconds the curve shows a continuous non-exponential decrease of the signal. Note that a typical exponential decay would be represented by a straight line in this logarithmic plot. After a microsecond the signal is indistinguishable from the background intensity.

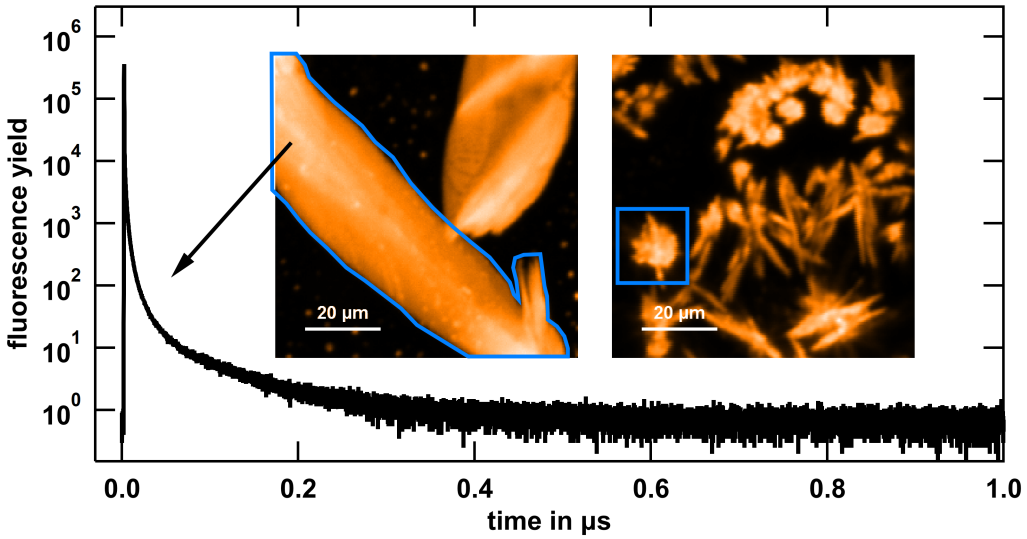

Figure 5.12: Time dependent fluorescence yield for a large tetracene crystal on glass as shown in the blue masked area in the left inset. The curve shows a fast decay in the first tens of nanoseconds followed by a continuous non-exponential decrease of the signal. At around 1 µs the fluorescence yield reaches the background intensity. The right inset shows smaller crystals of the same sample where the blue marked area is used for following investigations.

To have a more detailed look on the evolution of the signal at smaller timescales further measurements were performed at a repetition rate of 40 MHz at different laser powers as shown in Figure 5.13. All curves are normalized by dividing the yield by the laser power and the actual measurement time. For high laser intensities an OD3 filter was used in front of the detector leading to a higher noise level in the red curves. In a) the curves obtained from the large aggregate are shown for 0.0002 µW (black), 0.12 µW (blue) and 2.45 µW (red) excitation power. After the ≈ 50 ps long laser pulse at around 3 ns the fluorescence yield immediately decreased over nearly two orders of magnitude mostly independent from the excitation power. After this prompt decay with an exponential behavior[2] with a time constant of $\tau_{1;L} = 150$ ps, the yield further decreases in a non-exponential way. The higher the excitation power the steeper is the fluorescence decay. Having a closer look to times between 4 and 10 ns an oscillation of the signal becomes visible. In literature, this beating of the fluorescence yield is referred to as a production of coherent triplet pairs due to direct singlet fission [180] and will be analyzed in Figure 5.14.

In contrast to the larger crystal, the smaller aggregates show a different behavior as shown in Figure 5.13b. The prompt decay is much less compared to the larger crystal but has a comparable decay constant of $\tau_{1;S} = 170$ ps and is followed by a nearly exponential decay at lower excitation densities where the apparent lifetime is approximately in

2 The decrease of the fluorescence yield can be described by a straight line in the logarithmic plot.

between 3 and 5 ns. At higher laser power the decay becomes non-exponential with a much steeper development. A beating is not clearly visible at any intensity.

To analyze fluorescence yield oscillations of the large crystal, part of the blue curve in Figure 5.13a was fitted with a multi-exponential function. The residual of the fit represents the beating as shown in Figure 5.14a. We can clearly observe a damped oscillation with a frequency of approximately 1.07 GHz. The Fourier transform of the signal (b) shows additional peaks at 1.81 GHz and 2.99 GHz which are in accordance with the peaks observed by Burdett et al. [180]. A detailed interpretation of this data will be given in the following section on Page 78.

To study the influence of the morphology, the sample investigated in the previous chapter was analyzed by FLIM as well. After transferring the sample ex-situ to the FLIM no fluorescence signal could be detected, which will be discussed on Page 71.

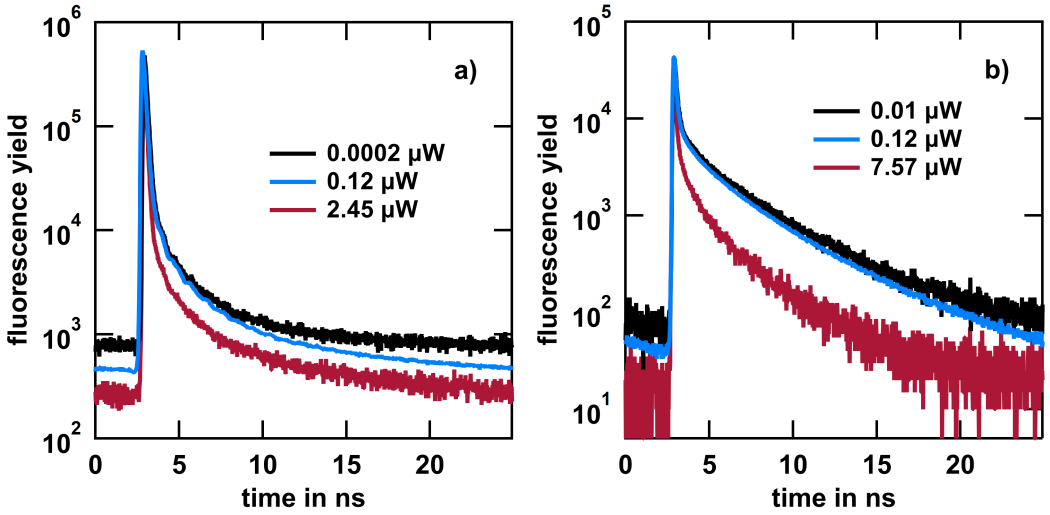

Figure 5.13: Power dependent fluorescence yield for a) a large crystal and b) smaller aggregates as shown in Figure 5.12. The curves are normalized to the same excitation power. For larger crystals a "beating" of the fluorescence yield is clearly visible around 5 ns.

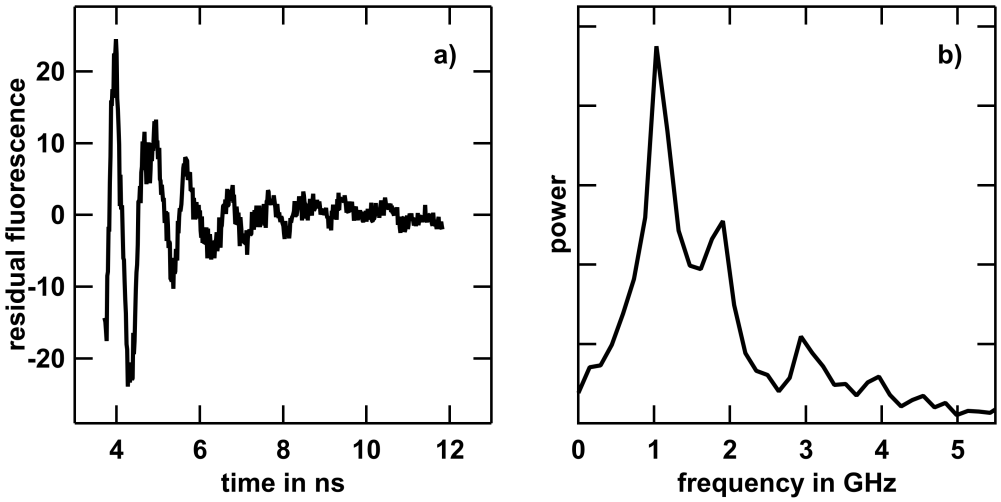

Figure 5.14: a) Fluorescence beating pattern extracted from the blue curve in Figure 5.13a and b) Fourier transform as a proof for triplet pair coherences. See text for details.

5.4 DISCUSSION

In this part we want to focus on different phenomena observed in the previous section, the results will be interpreted and discussed with respect to literature.

Disappearance of Fluorescence after PEEM measurements

The first striking observation is the vanishing fluorescence of the evaporated tetracene after PEEM measurements. Several scenarios might be possible to explain this investigation. Since the molecules are vacuum evaporated it is unlikely that the tetracene vaporized immediately after inserting in the PEEM vacuum chamber. In addition, the greenish fluorescence was clearly visible through the load lock window prior to the measurements. Hence, evaporation could just have taken place over longer timescales. In this case one would expect changes in the PEEM images over time which is not in accordance with the observations showing unaltered structures over several months.

Another supposable possibility is an evaporation of tetracene directly after the first illumination by the mercury lamp. In previous fluorescence studies it was shown that the evaporated layer is very sensitive to heat which possibly could be coupled in radiatively. Figure 5.15 shows fluorescence images of an evaporated tetracene film on silicon at room temperature ($\approx$ 20° C) before (a) and after heating to approximately 25° C for a few minutes (b). The cross was prepared after deposition by scratching with a razor knife for site identification. Before heating a dense fluorescing layer is visible having some brighter spots. When slightly heated above room temperature the fluorescence yield of the layer decreased immediately and some dot like structures were formed showing higher signal.

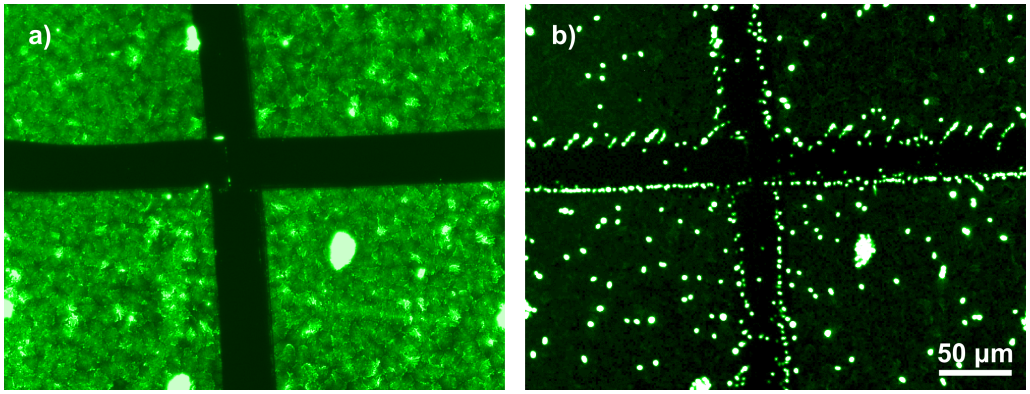

Figure 5.15: Fluorescence microscopy images under identical acquisition settings using GFP filtercube of vacuum evaporated tetracene on silicon before (a) and after heating to approximately 25° C for a few minutes (b). The cross was prepared after deposition by scratching with a razor knife.

With this knowledge it is likely that the structure of the investigated PEEM sample changed upon first illumination with the mercury lamp and reached some stable condition, which was measured afterwards. Since the fluorescence vanished this might be only a few monolayers of molecules being sufficient for detection by photoemission as can be clearly seen as grainy structure especially upon illumination with cw light sources (cf. Figure 5.4).

Image Contrast Formation & Electronic Level Scheme

For identification of the reason for different appearances depending on the employed light source (Figure 5.5) we now analyze the underlying photoemission process and derive an electronic level scheme.

Let us start with the interpretation of the image taken under cw illumination at 405 nm (Figure 5.4b) with an averaged photon order of 1.8 indicating 2PPE as the dominant process. As we use continuous illumination a two photon process is very unlikely due to the low field intensities unless a sequential 2PPE process takes place with a sufficiently long living intermediate state. For the silver nanoparticles such an intermediate state is not available for this excitation wavelength of 405 nm since the plasmon lifetime has been determined to be only a few fs (cf. Figure 4.13). Hence, the nanoparticles do not show a significant photoemission signal. In contrast, the evaporated tetracene is clearly visible indicating the presence of a long-lived state with an energetic position of at most 3.06 eV (405 nm) below the vacuum energy. The most prominent candidate is the triplet state T_1, which is described having a lifetime up to several µs [9, 66, 181, 182] and can be effectively populated by singlet fission at this excitation wavelength [9, 10]. Energetically the triplet state is known to be 1.24 eV above the S_0 [183–185]. The ionization potential described for macroscopic crystals or several 10 nm thick films is reported to be $5.4 - 5.6$ eV [183–185]. This range would be in disagreement with the actual interpretation since 4.16 eV photon energy would be required to extract an electron out of the triplet state which wouldn't be possible with the used 405 nm laser. Nevertheless, a work function of approximately 4.3 eV is observed (cf. Figure 5.6). On the one hand, this could just be observed by electrons emitted out of the silicon, but on the other hand the influence of the substrate might be strongly enhanced since we are presumably studying just a few monolayers of molecules. Hence processes like e. g. a partial charge transfer, static and induced dipole interactions could lower the work function. Considering all these possibilities it is supposed that most of the electrons under cw 405 nm excitation are emitted out of the long lived triplet state T_1 or energetically slightly distorted trap states [9, 66]. In this scenario the image shown in Figure 5.4b represents the population of long-lived intermediate states, showing a grainy distribution in this non-perfectly ordered arrangement of molecules. Hence, we can assign the grainy structure to local differences in the lifetime of the intermediate long-living state. As shown in Figure 5.8 significant blinking occurs, which is often attributed to the presence of trap states and will be discussed in the next paragraph on page 74.

Varying the wavelength to 266 nm (4.66 eV) under continuous illumination the appearance of the image switches crucially and the photon order reduces to 1.0. The bright dots can now be attributed to the silver nanoparticles emitting electrons in a 1PPE process since the silver work function of 4.26 eV [120] is lower than the photon energy. Considering that this process is not plasmonically assisted the intensity scales according to the particle's volume (for small clusters) or to the exposed surface (for larger particles) (cf. [99, 100]), apart from possible variations due to different work functions. Due to the mass selection in the deposition of the particles, the photoemission intensity is comparable for every particle.

In view of the tetracene signal, the grainy structure becomes more smoothed compared to cw excitation at 405 nm wavelength indicating that the ground state is involved which is supported by the photon order. Nevertheless, some residual structure is visible which vanishes under fs illumination as we have seen in Figure 5.5. A possibility to explain these remaining inhomogeneities of the signal might be the presence of saturated (i. e. completely excited) long living intermediate states which reduces the apparent photon order to unity. In addition, the signal could originate from an ordinary sequential 2PPE process over the T_1 or trap states which only slightly effects the photon order

observed in the measurements due to the low relative occurrence in comparison to a direct 1PPE process out of the S_0 ground state.

Switching to fs illumination the tetracene signal becomes homogeneous indicating that spatial lifetime differences do not play a crucial role in the photoemission process either due to the fast processes within a single laser pulse or the absence of participation of intermediate states or a combination of both. Utilizing the electron spectra shown in Figure 5.6 the interpretation gets additional input. Focusing on the tetracene signal (red curve) at 266 nm (4.66 eV) (Figure 5.6a) two contributions are visible in the logarithmic plot. The main peak is attributed to a direct photoemission of the HOMO S_0 under the assumption that $\approx$ 4.3 eV are sufficient to emit photoelectrons out of initial state in the tetracene aggregates as described above. The second peak with higher kinetic energies shows an enhanced photon order and is therefore attributed to the T_1 state $\approx$ 1.24 eV above S_0. The possible excitation pathways for pulsed illumination with 266 nm wavelength and the energy level alignment is schematically shown in Figure 5.16a.

For 400 nm (3.1 eV) excitation wavelength the electron spectrum (see Figure 5.6b) still contains two main contributions. Due to the second order process the width of the spectrum from the low energy cutoff to the first visible Fermi edge increases and the photon order is constant $\approx$ 2.3 in this regime. To be consistent with previous considerations the spectrum mainly consists of 2PPE contributions from the S_0 as initial state, which forms a large peak over the whole width. On top, on the low energy side of the spectrum the emission out of the T_1 state is superimposed. The processes are illustratively sketched in Figure 5.16b.

Considering the cluster signal in the two images under fs illumination (Figure 5.5) the influence of the resonant plasmonic excitation is clearly visible for 400 nm wavelength (b), where the electron yield strongly differs from particle to particle depending on the actual resonance wavelength. In contrast, the electron yield at 266 nm wavelength (a) is much more homogeneous according to the particles' volume or the exposed surface (for larger particles) (cf. [99, 100]).

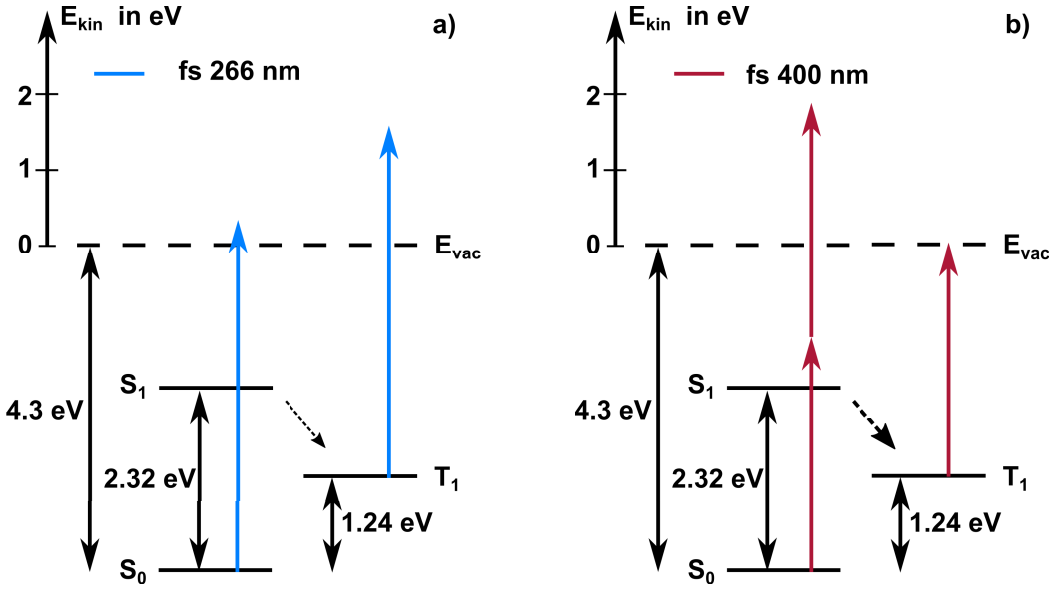

Figure 5.16: Schematic illustration of the energy levels of tetracene as observed in the experiments. Possible excitation pathways are sketched by arrows for fs 266 nm (a) and 400 nm (b).

To recapitulate, we have assigned the peaks visible in the electron spectra to electronic states of the tetracene and consistently explained the appearance of the images measured for different wavelengths. In accordance with literature the electronic structure of tetracene is characterized by the ground state S_0, a first excited triplet state T_1 1.24 eV above S_0, and a first excited singlet state S_1 2.32 eV above S_0 [183] as shown in Figure 5.16. The population of these states can be probed as described above with the necessity that ≈ 4.3 eV photon energy is sufficient to emit an electron out of the S_0 state as discussed. All following investigations will be based on the assignments of the probed states as basis for subsequent considerations.

Blinking & Bleaching

In Section 5.2.3 we have seen signatures in the PEEM signals which strongly remind us to prominent investigations of blinking and bleaching in single molecules or quantum dots for example [178, 179, 186–193]. Surprisingly, the exact physical origin of blinking is not completely understood though it was in the focus of research for at least two decades. A lot of models failed to explain the characteristic power-law distribution of on and off times[3] [179, 194]. In first approximation blinking is believed to originate from a light induced charging of molecules or quantum dots [194], where the radiative dissipation channel for excitations is blocked due to the presence of a long living exciton. During the lifetime of this, often trapped, excitation all further excitations will decay in a fast, non-radiative mechanism called Auger recombination [194]. In addition to this simple approach diffusion based models have been developed which are able to explain a power law coefficient of $\approx -3/2$ as observed in many experiments on quantum dots and any kind of single quantum emitters embedded in a disordered medium including organic molecules [179].

On the other hand, bleaching usually means an irreversible chemical reactions rendering the molecules to become non-fluorescent. In contrast, here we observe a reversible "bleaching" which fully recovers the photoemission signal within several minutes.

Apart from all benefits and physical insights both effects, blinking and bleaching, might give, a lot of effort was done to reduce the effects due to the restrictions they induce to the experiments. On the one hand, the occurrence of blinking masks spatially resolved intensity analysis. Due to the power law behavior it is not even possible to average measurements of a single emitter since its statistics is governed by non-ergodicity, and the average on and off times diverge which means such systems do not have a characteristic time scale [179]. On the other hand, bleaching obviously changes the system and the emission intensities hindering time dependent analysis. Approaches to restrain blinking are either focusing on the elimination of trap states or on decreasing non-radiative de-excitation channels or a combination of both [190].

Especially trap states or extremely long living triplet states are prominent candidates to play a crucial role in the investigated tetracene system. Nevertheless, the physical observable under investigation, namely the photoelectron yield, stays in contrast to the fluorescence signal usually used. This means that known concepts of blinking cannot be transfered directly and the physical origin of the signals must been taken into account. To the best of my knowledge this is the first study reporting on blinking in a photoemission spectroscopy experiment while related phenomena were observed with scanning photoionization imaging microscopy [195]. In detail the photoelectron yield represents the population of a certain state in combination with the photoemission probability which can be interpreted in terms of the three-step-model [135, 196].

Here, blinking was only observed under continuous excitation at a laser wavelength of 405 nm. As discussed above, only electrons from the lowest triplet state or energetically

3 Here, on and off times describe the radiative and non-radiative decay channels, respectively.

similar states with a sufficiently long lifetime are supposed to be emitted. Therefore trap states [9, 66, 197] can also be involved being typical for fluorescence blinking [190]. The trap state density is assumed to be increased at the border of dendritic structures or islands [9, 198, 199], which is in accordance with the observed spatial distribution of blinking areas. Since the photoelectrons' kinetic energies are close to zero the initial state binding energy must be just below the work function such that emission becomes possible. Considering the conventional picture of luminescence blinking where a molecule is excited but the exciton is trapped and hinders the radiative decay of an additional excitation, we can assume that the trapped excitations also slightly modifies the local work function or energetic position of the electronic states. This could result in a threshold effect due to a trap state induced work function change. To put it in a nutshell the photoemission could be activated or deactivated due to the presence of a trapped excitation in analogy to the switching between radiative and non-radiative de-excitation channels in fluorescence blinking induced by trapped excitons.

The described scenario would also be in accordance with the observed reversible photobleaching which could correspond to the population of trap states.

For further studies the proof of the power-law distribution of on and off times would be an interesting step in combination with energetically resolved measurements in a retarding field setup or with a hemispherical analyzer to detect the supposed energetic shift of the involved states or the local work function.

Exciton-Exciton Annihilation

In Section 5.2.4 we have defined an additional photoelectron yield ΔY describing the amount of excess photoelectrons detected when using cw 405 nm and fs 266 nm illumination simultaneously compared to the sum of the individual observed signals. Since the number of photoelectrons emitted by illumination with the cw laser is negligible compared to the fs laser (cf. Figure 5.10), one can assume in a good approximation that the cw laser just affects the population of involved states while the fs laser additionally probes those energy levels. In accordance with the previous considerations, we assume that the triplet state T_1 is efficiently pumped by singlet fission under cw illumination with 405 nm. This equilibrium population gives an additional contribution to the fs photoemission leading to ΔY due to this synergistic effect when illuminating with both lasers simultaneously. A schematic overview of the involved processes is shown in Figure 5.17.

We can conclude that ΔY is a measure for the population of the T_1 state or energetically close trap states which can be populated as well. A linear dependence of ΔY on $P_{266\text{nm}}$ would indicate a pure probing characteristic. The observed exponent of $n_{266} = 0.91$ shows that this is nearly the case. This sublinear slope implies that the pulse does not purely probe the triplet state instead the state is additionally populated during the pulse. This leads to an effect which is clearly visible in the power dependence on $P_{405\text{nm}}$ in Figure 5.9b. Here a sublinear behavior is observed with an exponent of $n_{405} = 0.50$. In general, a sublinear exponent shows that it becomes more difficult to excite a state the higher its population is. Typical scenarios are ground state depletion and annihilation processes [200]. Latter ones are well known for tetracene and are mainly observed via power dependent fluorescence measurements [66]. To understand the slope in the power dependence we have a look on the population of the triplet state N_{T1} which is proportional to ΔY in good approximation. Within a simple rate model, the temporal evolution of N_{T1} is given by [201–204]

$$\frac{dN_{T1}}{dt} = G(t) - kN_{T1} - \gamma {N_{T1}}^2 \tag{5.2}$$

where $G(t)$ is the triplet generation rate, k the intramolecular decay rate, and γ the exciton-exciton annihilation (EEA) rate. Since we are using cw illumination to build up

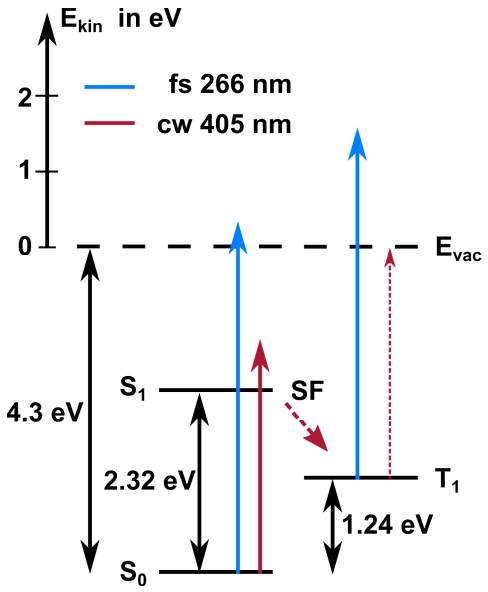

Figure 5.17: Schematic illustration of the energy levels of tetracene with possible excitation pathways under simultaneous illumination with fs 266 nm and cw 405 nm lasers. The cw laser mainly populates the T_1 state by singlet fission (SF) which is probed by the fs laser pulse. The emission of the cw laser (thin red dashed arrow) is negligible.

a population which is then probed by the fs laser pulse, an equilibrium population is established and we can solve the Equation 5.2 for $\frac{dN_{T1}}{dt} \stackrel{!}{=} 0$ and $G(t) = G = \text{const}$, which gives

$$N_{T1} = -\frac{k}{\gamma} \pm \sqrt{\frac{k^2}{\gamma^2} + \frac{G}{\gamma}}. \tag{5.3}$$

Since $G = G(P) \propto P$ in absence of saturation we obtain a power law exponent of $1/2$ as observed for ΔY. This dependence is typical for two and three dimensional systems while for one dimensional exciton diffusion a value of $1/3$ is reported due to a more confined diffusion [200, 205].

To conclude, we have shown that EEA plays a significant role in the dynamic of the system. The exponent of $1/2$ implies a multidimensional exciton diffusion. To analyze the role of the silver nanoparticles we have to analyze spatially resolved triplet population.

Near-Field Enhanced Exciton Generation

Figure 5.10c shows a spatially resolved map of ΔY where blue colors correspond to additional counts during simultaneous illumination with fs 266 nm and cw 405 nm laser. Beside the homogeneous background, the image clearly shows regions of increased signal. By comparing the positions to the cluster locations in Figure 5.10a we can assign each spot of enhanced ΔY to a specific cluster location. This implies that either simultaneous illumination promotes electron emission from clusters or the presence of clusters can enhance the population of the triplet state. By looking on the spectral signature of ΔY (Figure 5.10d) we obtain a single peak. This, however, seems to be unlikely when both cluster and molecules (as clearly seen in the map) benefit from simultaneous illumination, since for the cluster either a peak at higher kinetic energies would be expected or a spectrum dominated by secondary electrons with a low energy cutoff at zero kinetic energy which is not the case. Therefore, a coupling between silver nanoparticles and tetracene molecules seem to be very likely. A possible scenario would be the excitation of the molecules within the enhanced near-field of the particle plasmons. For this, the

resonance of the particles must be around 405 nm which should be the case for at least few of the particles, particularly in view of the relatively broad resonances (cf. Section 4.1). In addition, also the geometrical arrangement needs to fit requirements for the near-field assisted exciton generation [206, 207]. Considering these geometrical and plasmonic restrictions it is not surprising that not every particle enhances the excitation of the molecules.

The attentive reader may already have noticed that the spectral signature of ΔY (Figure 5.10d) does not exactly fit to the model shown in Figure 5.17 where the emission out of T_1 after absorption of a 266 nm photon would be expected around 1.5 eV kinetic energy. However, in contrast to a pure optical excitation the electron gets separated from the hole during photoemission process which is bound with approximately $E_{\mathrm{Exc;bin}} = 0.81\,\mathrm{eV}$ [208]. Depending on the screening of this Coulomb potential the electron loses up to $E_{\mathrm{Exc;bin}}$ during emission. The exact screening can vary depending on the dynamics, the dielectric properties of the system, and the residence time of the electron in the vicinity of the photo hole, i. e. its kinetic energy, due to the dynamic final state effect [209]. In the extreme case of an electron escaping immediately (high kinetic energy) the charge carriers have no time to shield the hole potential and the electron loses the complete $E_{\mathrm{Exc;bin}}$.

Excited State Lifetimes

After focusing on synergistic effects to populate the T_1 triplet state, we now study its dynamics. Therefore, we will first have a look on possible decay processes after excitation with a cw 405 nm in vibronically excited S_1 states. After excitation of the singlet it can either decay via prompt fluorescence (Figure 5.18a) or undergo a singlet fission process creating two triplet excitons in the T_1 state. From there again two scenarios are possible. The two triplets can annihilate by triplet fusion building one excited singlet exciton in the S_1 state which then again can decay radiatively by delayed fluorescence (Figure 5.18b) or the triplets can decay individually (Figure 5.18c).

Prompt fluorescence (Figure 5.18a) is well studied in literature and decay times of the S_1 states are between $\approx$ 80 ps (polycrystalline films) [66, 197, 210] and $\approx$ 260 ps (single crystals) [9]. This decay was not observable within this specific PEEM experiment since only the triplet state population was probed here. The detailed process of singlet fission leading to the population of the triplet state is still subject to ongoing research and different intermediate states with multi excitonic or charge transfer character are discussed [183, 197, 211, 212].

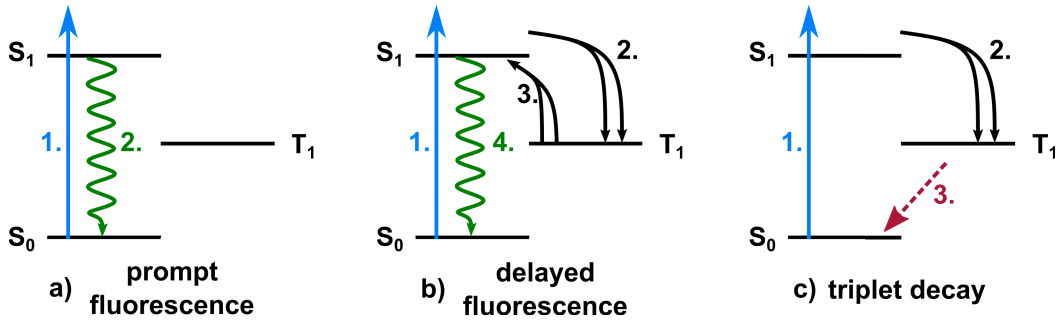

Figure 5.18: Schematic representation of possible decay processes after excitation into a vibronically excited S_1 state. The excited S_1 can either decay via prompt fluorescence (a) or undergo a singlet fission process exciting two triplet excitons. These triplets can either fuse to a singlet resulting in delayed fluorescence (b) or decay individually (c).

By directly observing the triplet population lifetimes of all decay processes, radiative and non-radiative, are in principle accessible. Literature on optical studies is restricted to delayed fluorescence giving an indirect measure for the triplet lifetime. Depending on the morphology and the data interpretation, reported lifetimes of delayed fluorescence vary from a few ten ns to several µs [9, 66, 181, 182]. Note that the statement of a typical lifetime appears questionable since the decay due to EEA is non-exponential and described by the EEA rate γ (see Equation 5.2). To describe the temporal evolution after an initial excitation via a pump pulse we can set the generation rate $G(t) = 0$ and obtain

$$\frac{dN_{T1}}{dt} = -kN_{T1} - \gamma {N_{T1}}^2 \tag{5.4}$$

with the solution

$$N_{T1}(t) = \frac{kn_0}{\gamma n_0 \left(e^{kt} - 1\right) + ke^{kt}} \tag{5.5}$$

with $n_0 = N_{T1}(0)$. When fitting the measured data shown in Figure 5.11 with this equation the decay can be described only with three[4] free fit parameters instead of seven in a triple exponential fit. The fit is mainly affected by the EEA rate γ since the observed intrinsic triplet lifetime $\tau_T = k^{-1}$ is in the range of the highest reached delay times which minimizes the influence on the curve. Therefore only a lower limit of $\tau_T > 10\,\mu s$ can be deduced. Furthermore, it must be pointed out that the experiment itself may show systematic errors for larger delay times since the time between two pump pulses is only twice as long as the highest delay time measured. Therefore the system won't find the ground state between two measurements and the probe pulse will have significant influence on the population as well.

To conclude, the decay times in the PEEM pump probe experiments can be attributed to EEA and the intrinsic decay of a triplet exciton.

A spatially resolved analysis of the decay times was not possible due to the appearance of blinking (cf. Section 5.2.3).

Fluorescence Lifetime Imaging

To obtain the short-term dynamics and validate the observed decay times FLIM measurements were performed. In contrast to PEEM, we expect to see the prompt fluorescence in addition to the delayed fluorescence, as a consequence of the EEA, while the intrinsic triplet decay is not directly accessible in this setup but can be detected indirectly since it affects the triplet population and therefore the delayed fluorescence.

The power dependence (Figure 5.13) shows a faster decay with increasing excitation power, which is a typical signature of EEA [202, 213]: the more excitons are created the higher is the probability to find an annihilation partner, hence the steeper is the decay. This behavior is visible for both large (a) and small (b) crystals. Nevertheless EEA appears to be much less present in smaller aggregates. From the FLIM image shown in Figure 5.12 we can assume that the smaller crystals might be less ordered, which would lead to a slower diffusion constant of the excitons which is proportional to the EEA rate γ explaining the differences in the power dependence.

Focusing on the time evolution, we can detect a first exponential part of the prompt fluorescence (best visible in Figure 5.13b) followed by a non-exponential part due to delayed fluorescence. Where the trend is continued until the background noise level is reached after $\approx 1\,\mu s$ (cf. Figure 5.12). For the large crystals an oscillation of the signal is observed a few ns after excitation. This behavior was previously attributed to geminated EEA [180, 214]. After the singlet fission, a coherent superposition of three triplet pair states is generated. The projection of this state onto the singlet state, giving

4 In addition to k and γ an offset was used for experimental reasons.

the probability for the recombination, is oscillating. The frequencies of this oscillation is given by the possible energy differences of the triplet manifold and is in accordance with literature [180]. For further information on this process see [180]. Interestingly, the oscillation amplitude is decreasing with increasing laser power (Figure 5.13a). A possible explanation would be a disturbance of the coherence due to diffusing excitons. However, for small aggregates an oscillation was not observable. This observation is in accordance with literature where the amplitude decreased with the disorder of the aggregates [180]. Although the precise reason remains unclear, a strong local heating in single crystals plays a role since the coherent evolution of the triplet pair state is highly temperature dependent with the unintuitive tendency to disappear at lower temperatures [180].

After a few ns coherence is lost mainly due to dephasing and two free triplet excitons are formed showing non-geminated delayed fluorescence.

An analytically fit function is not available including all involved processes. To obtain such a fit function the highly coupled rate equations for the singlet and triplet system must be solved. Especially the transition from geminated to non-geminated EEA needs further considerations of specific diffusion models leading to a time dependent annihilation rate $\gamma = \gamma(t)$ [202–204], which exceeds the focus of this work. Therefore, lifetimes are determined by piecewise fitting of the obtained curves.

The prompt fluorescence was observed to have a decay time of 150 ps for the large crystal and 170 ps for the small aggregate, respectively. This is in between the values of the literature [9, 66, 197, 210], although better order (as expected for the larger crystals) is known to increase the lifetime of the prompt fluorescence. For obtaining lifetimes of the delayed fluorescence an established method is to exponentially fit the latest part ($> 0.8\,\mu s$) of the decay curve which leads to a lifetime of $\approx 4\,\mu s$ being compatible to the literature (e. g. 1.37 µs, see [9]). Nevertheless, this method is questionable since the delayed fluorescence cannot be described by a single decay time.

To analytically describe the temporal behavior observed in Figure 5.12, we start again with the rate equation 5.4. This formula describes the evolution of the triplet population under the assumption of a spatially homogeneous triplet exciton distribution, which is assumed to be the case when non-geminated EEA dominates the signal. In case of geminated EEA the quadratic dependence on the triplet density is questionable since the exciton pairs are born side by side and do not have to find each other. Therefore, this can not be treated as an usual two particle process. However, Equation 5.5 gives the triplet population after geminated EEA has happened. In FLIM we are not sensitive to the population as in PEEM, therefore we cannot take this equation directly to fit our data. Instead we need to connect the triplet population to the delayed fluorescence being the observable. For simplification we assume that all fused triplet excitons will undergo delayed fluorescence and not do a fission again. The temporal structure of the fluorescence of the singlet state after population by fusion can be neglected as it is very fast compared to the timescales of fusion processes. Under these assumptions we can write the delayed fluorescence yield DF as

$$DF = \frac{dN_{S1}}{dt} = +\gamma {N_{T1}}^2 \tag{5.6}$$

where we can plug in Equation 5.5 for N_{T1} and we obtain DF being proportional to

$$DF = \frac{dN_{S1}}{dt} = +\gamma \left(\frac{k n_0}{\gamma n_0 \left(e^{kt} - 1\right) + k e^{kt}} \right)^2 \quad . \tag{5.7}$$

Using this equation[5] leads to a reasonable approximation of the measured data as shown in Figure 5.19 (green curve). The fit starts at 35 ns after excitation where geminated EEA

5 For experimental reasons an offset was added to the formula.

is assumed to be neglectable. For comparison a single exponential decay was fitted as well (red curve) showing obvious deviations in the curve form but is not completely off, leading to a lifetime of 40 ns, which can easily be misinterpreted. In contrast using Equation 5.7 as fit function shows that annihilation dominates the fluorescence and therefore no time constant for the delayed fluorescence is meaningful. An absolute determination of γ is not possible due to the unknown detection probability. Interestingly, the intrinsic lifetime $\tau_T = k^{-1}$ can be determined indirectly through the influence on the population and therefore the delayed fluorescence although the decay itself is not observable with the FLIM. Like in the PEEM data the fitting error of τ_T is large since the effect of a long lifetime on a timescales up to 1 µs is marginal. Therefore again a lower limit of $\tau_T > 10$ µs is given.

All in all, the obtained FLIM measurements are in accordance with literature as well as with the obtained PEEM measurements although the instruments are sensitive to different quantities.

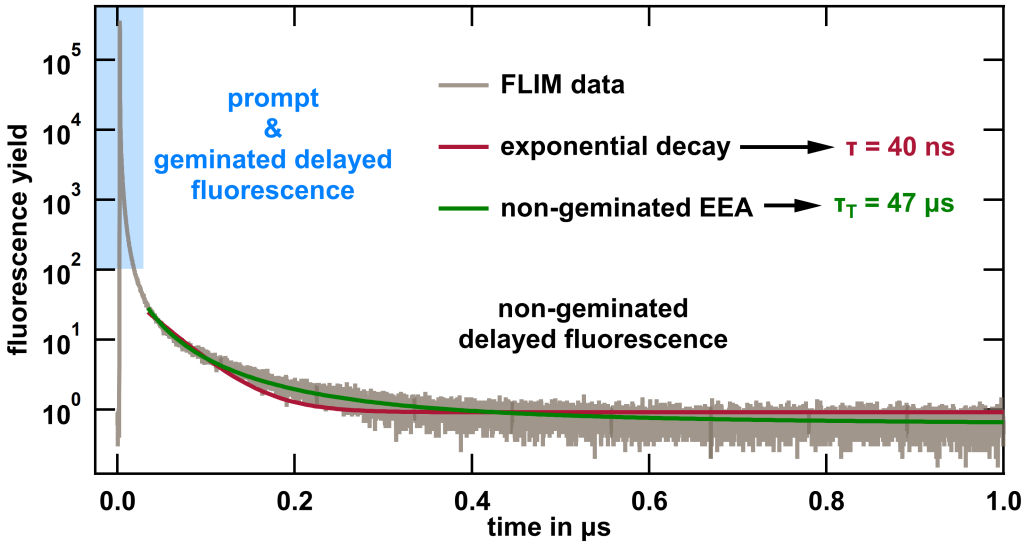

Figure 5.19: FLIM data from Figure 5.12 of a large single crystal. The detected fluorescence can be divided into three contributions. Prompt fluorescence takes place in the first ns characterized by an exponential decay with a lifetime of 150 ps (top part of blue box) and geminated delayed fluorescence occurring in the first ten ns due to the coherent excitation of a triplet manifold (lower part of the blue box). After decoherence is reached the decay can be described purely by non-geminated delayed fluorescence. This part was fitted using Equation 5.7, the best fit is shown as green curve and resulted in an intrinsic triplet lifetime of $\tau_T = 47$ µs. The error of this value is significantly high and the actual curve does not depend crucially on this value in this time range. Therefore a lower limit of $\tau_T > 10$ µs is given. For comparison a single exponential decay (red curve) was fitted in addition giving a decay constant of $\tau = 40$ ns. See text for details.

5.5 CONCLUSION

In this chapter the coupling from plasmonically excited silver nanoparticles to tetracene aggregates was investigated. Tetracene molecules have been vacuum evaporated in a home-built setup onto a silicon wafer with native oxide layer. After an ex-situ preparation control, size selected silver nanoparticles with an average height of $\approx 15\,\mathrm{nm}$ were soft landed on top. By selecting various excitation sources the sample was characterized by means of PEEM and an energetic level scheme was derived which is in accordance with all observations and literature. Under illumination with $\approx 400\,\mathrm{nm}$ wavelength triplets can be populated efficiently due to singlet fission. Within the vicinity of the nanoparticles an increased triplet population was detectable in most cases. Within a two color experiment clear signatures of triplet-triplet-fusions are visible. To study this process in more detail the excited state lifetime was measured in a pump-probe setup in PEEM. It turned out that the decay is described by a fast decay of some hundred ns and a slow decay with several ten µs lifetime. The long time is attributed to a non-radiative decay which is directly observable in PEEM via the population of the triplet state itself. As a reference experiment fluorescence lifetimes of drop-casted tetracene aggregates were determined by FLIM. The short lifetimes were directly observed and can be attributed to geminated delayed fluorescence. Although the lifetime of the non-radiative decay can not be directly observed, its lifetime was confirmed by modeling its influence on the observable decays due to a reduced triplet state population. In addition to the lifetimes clear signatures of a coherent excitation of geminated triplet pairs were observed.

These investigations have shown that it is possible to locally excite Frenkel excitons in tetracene aggregates by using plasmonic silver nanoparticles as far-field near-field couplers. In addition, the observed lifetimes are long enough to render long range exciton migration processes possible making this promising for imaging exciton propagation. Since such migration was observed elsewhere [9] a possible pathway could be an improvement of the sample morphology for longer exciton migration length.

COPPER PORPHYRIN AND SILVER NANOPARTICLE HYBRID SYSTEM

6

In the previous chapter we used silver nanoparticles to locally excite triplet excitons in tetracene aggregates by using the plasmonic field enhancement leading to an enhanced singlet fission in the nanoparticles' vicinity. However, the excitons have not shown a noticeable migration which presumably is caused by a highly disordered arrangement of the molecular aggregates, as suggested in the literature [9]. Therefore, we extend our studies to CuTUP, where aggregation is known to form extended crystalline strands via drop-casting on both highly oriented pyrolytic graphite (HOPG) and natively oxidized silicon [69, KO-2]. Beside these macroscopic morphologies, self assembled monolayers have been intensively investigated by scanning tunneling microscopy (STM) [68, 215]. In addition, CuTUP is a promising candidate due to its strong absorbing Soret band around 400 nm matching the silver plasmon resonance. Upon absorption long-living triplet excitons are formed being a key requirement for long range triplet migration [62]. Furthermore, a plasmon-exciton hybridization of individual silver clusters covered by a thin zinc tetraphenylporphyrin (ZnTPP) film was observed [103] giving rise to a strong interaction in this related system.

CuTUP was synthesized as a powder by J.A.A.W. Elemans[1]. For sample preparation 1 µl of a $2 \cdot 10^{-4}$ M solution was drop-casted onto a piece of a Si(111) wafer with native oxide layer (n-type (As), $< 0.01\,\Omega$cm, CrysTec GmbH). After evaporation of the solvent (n-heptane) the sample was transferred into the PEEM chamber for cluster deposition. The electrostatic quadrupole was set to 1.5 kV during deposition at a gas flux of around 59 sccm argon and 3 sccm helium. A particle density of $\approx 0.1\,\mu m^{-2}$ was chosen (deposition time: $\approx$ 10 s). After deposition all PEEM measurements were performed under UHV conditions. Afterwards, the sample was ex-situ transferred for correlative AFM measurements of the morphology.

These AFM measurements are presented in the first section since knowledge on this correlative morphology will help us to understand the observations of the second part of this chapter where we mainly focus on the results of the PEEM measurements. For the latter, different excitation light sources are used and polarization dependent measurements are performed. A significant signal enhancement from areas where clusters are on top of CuTUP strands is observed for certain excitation configurations. In addition, the spectral signatures of the photoelectrons are analyzed and it turns out that discrimination of electrons from nanoparticles and dye is possible. Finally, the results are discussed.

6.1 MORPHOLOGY AND CLUSTER ARRANGEMENT

After dropcasting a variety of different morphologies are developing which are described in detail elsewhere [69]. For the earlier defined purpose of exciton migration we have chosen a region with branching aggregates. An AFM measurement of the selected region is shown in Figure 6.1a. This overview image of 35 µm × 35 µm has a resolution of 4096 × 4096 pixel giving the possibility to identify individual nanoparticles by simply zooming into the image. For better comparison to the later shown PEEM measurements all AFM images were rotated by 90° therefore the fast scanning direction is vertical. The dashed circles mark the positions of nanoparticles which will be investigated in more detail. The branches have average heights from 10 nm for the smallest structures up to

1 Radboud University Nijmegen, Institute for Molecules and Materials, Heyendaalseweg 135, 6525 AJ Nijmegen, The Netherlands

150 nm for the highest features in this image, while most aggregates are in the range of $30 - 60$ nm. The background is flat with an average roughness well below 1 nm (rms).

At some locations flat islands are visible on the background especially in the center and top region of the image. A zoom of the area marked by a dashed white square is shown in Figure 6.1b together with a line profile (c). All islands show nearly the same height of ≈ 5.8 nm.

Some nanoparticles are exemplarily marked (Figure 6.1), e. g. the one within the blue dashed circle which is shown in Figure 6.2 in a magnified view (a), including the corresponding line profile (b). Due to the convolution with the AFM cantilever, lateral dimensions are not representing the cluster size. Nevertheless the height can be determined to be ≈ 8.2 nm. The tail around the cluster with a bright region at the upper left side is an artifact from the cantilever, as we will notice that all nanoparticles appear in exactly this way.

Figure 6.3a shows the yellow marked silver nanoparticle (see Figure 6.1a) located onto a CuTUP aggregate. The line profile (b) shows a height of ≈ 8.5 nm.

Especially for the green marked particle in Figure 6.4a we can see the importance of knowing the exact cluster position. We will see in PEEM images later on that it is not possible to decide whether the particle is in a notch like the one right of the particle or flat lying on top of the aggregate as is the case here. The height of the cluster is ≈ 10.5 nm as can be seen in Figure 6.4b.

For all analyzed particles deposited on the strands the average height is the same as for the particles on the flat regions, hence the particles are lying exposed on the aggregates without showing signatures of an indentation.

6.2 SILVER NANOPARTICLES ON COPPER-PORPHYRIN-AGGREGATES

After having verified sample preparation and having characterized the cluster deposition, we will now study optical and electronic properties by means of PEEM providing insights in possible plasmon exciton coupling or exciton migration processes.

To this end we will start with a broadband mercury lamp illumination to have the plasmon resonance included in the excitation spectrum. With these measurements we will see a signal enhancement. To determine its origin a couple of experiments follow including polarization dependent fs laser excitation at 266 nm wavelength with a spectral analysis of the kinetic electron energies to distinguish between electrons being emitted out of molecular aggregates or silver nanoparticles.

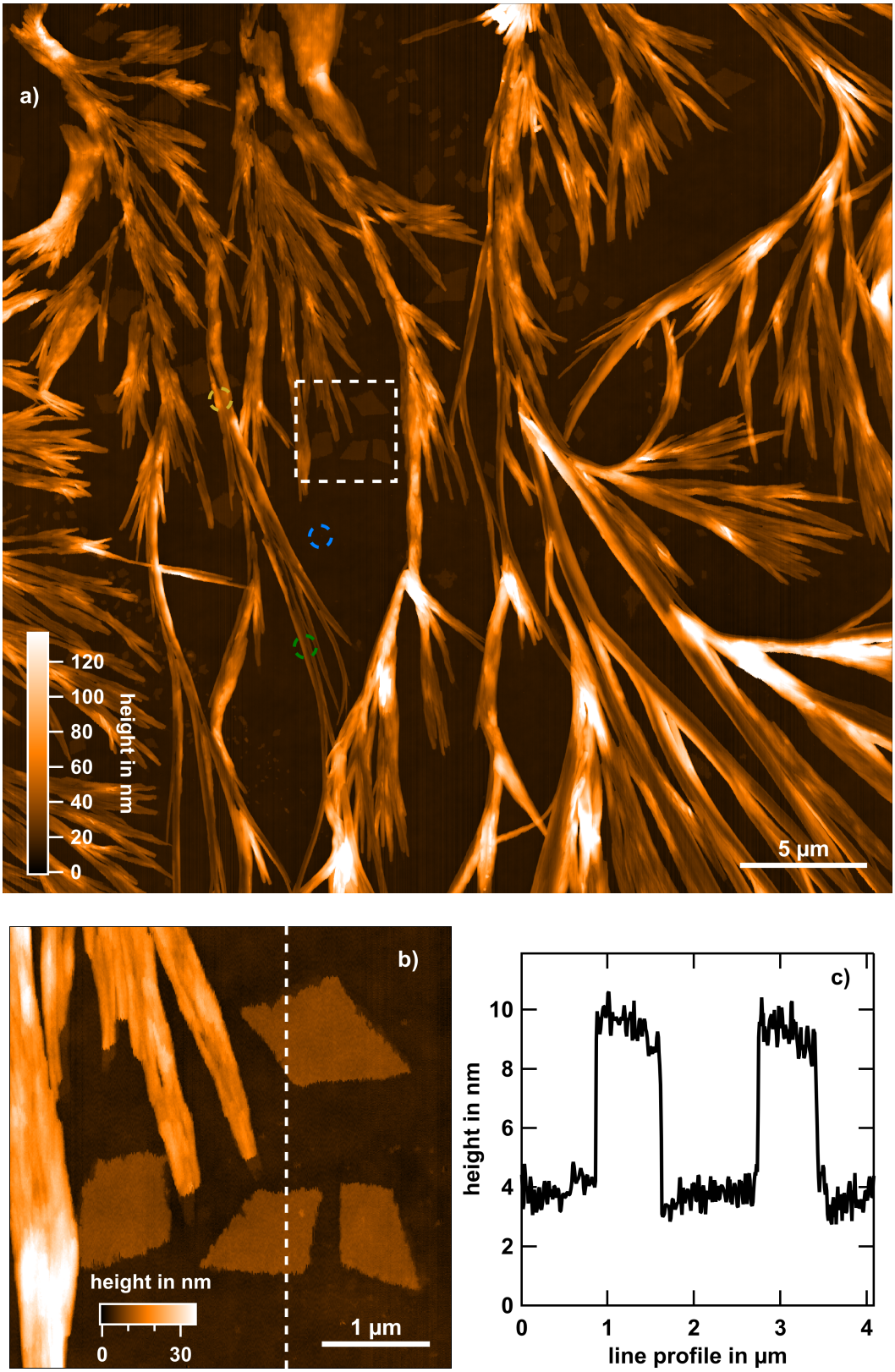

Figure 6.1: a) AFM overview image (35 µm × 35 µm) of the CuTUP sample with deposited silver nanoparticles. Three cluster positions are marked with dashed circles for further analysis. The dashed white square marks the position zoomed in b), where flat patches are visible. The line profile taken along the dashed white line in fast scanning direction is shown in c).

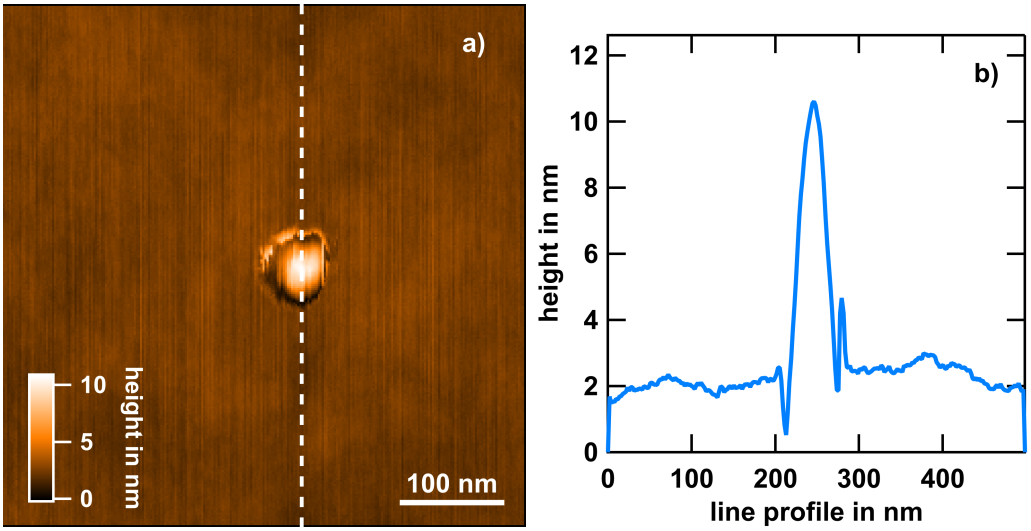

Figure 6.2: AFM image (a) together with line profile (b) along the dashed white line of the blue marked silver nanoparticle (see Figure 6.1a).

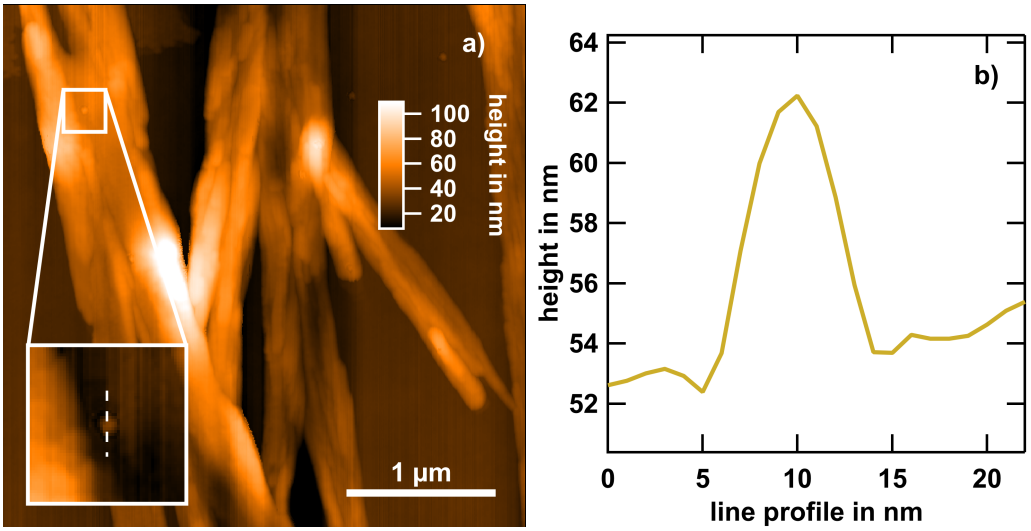

Figure 6.3: a) AFM image of the region around the yellow marked cluster (see Figure 6.1a). The inset shows a zoom on the cluster with an adapted colorscale. The line profile in b) was taken along the dashed white line.

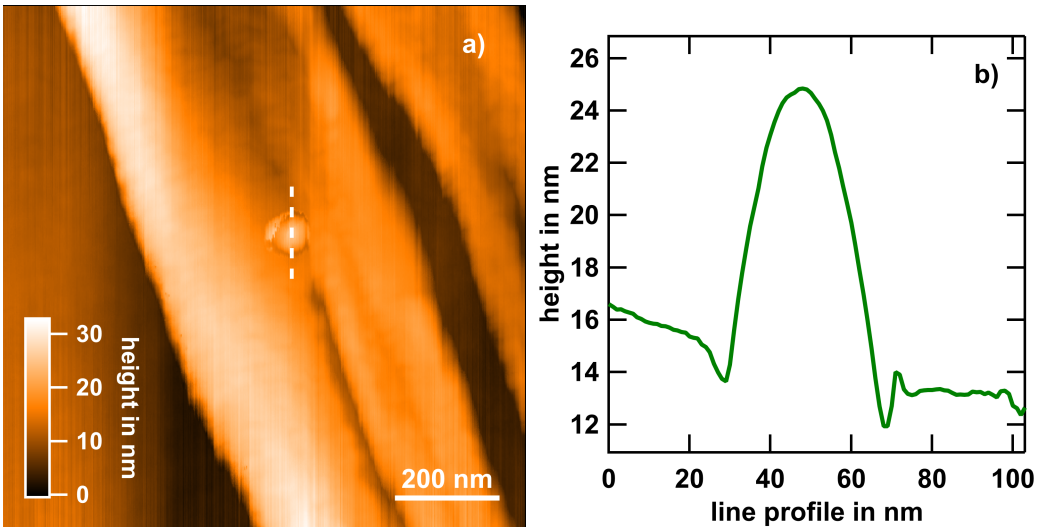

Figure 6.4: AFM image (a) together with line profile (b) taken along the dashed white line of the green marked silver nanoparticle (see Figure 6.1a).

6.2.1 BROADBAND ILLUMINATION WITH MERCURY LAMP

Figure 6.5a shows a total electron yield PEEM image (FoV: 25 µm) under broadband mercury lamp illumination from the same location as shown in the AFM image in Figure 6.1a. The CuTUP aggregates are visible as bright structures indicating a high photoelectron yield. The deposited silver nanoparticles appear as small dots which are much more pronounced in comparison to the AFM image due to their larger apparent size and the higher contrast in a PEEM measurement. The background in between the aggregates is clearly visible as well. The patches on the background (cf. Figure 6.1b) appear darker although we have measured an increased height in AFM. On closer inspection, clusters on molecular strands, are exceptionally bright compared to those on the substrate. Consequently, the signals of two exemplary chosen clusters (marked with yellow and green dashed circles, respectively) sitting on strands are compared to a reference cluster located on the background (blue dashed circle). By defining a gain

$$g = \frac{\text{"cluster on strand signal"}}{\text{"strand signal"} + \text{"reference cluster signal"}}$$

where the strand signal was taken on the same molecular aggregate in close vicinity to the respective cluster, we obtain an apparent enhancement of 1.44 (yellow) and 1.34 (green), respectively.

To proof whether plasmons are possibly causing this signal enhancement a bandpass filter was used narrowing the broadband excitation to a wavelength range from 260 to 340 nm. A PEEM image acquired under these conditions is shown in Figure 6.5b. The overall appearance is darker. In both cases brightest features are normalized to their maximum intensity. Clusters being located on the molecular aggregates are even more pronounced, which is also confirmed by the resulting apparent enhancement factors of 1.83 (yellow) and 2.64 (green), hence we can rule out a plasmonic effect. In order to acquire ToF PES pulsed excitation with a 266 nm fs laser is used in the following to analyze photoelectron spectra as well.

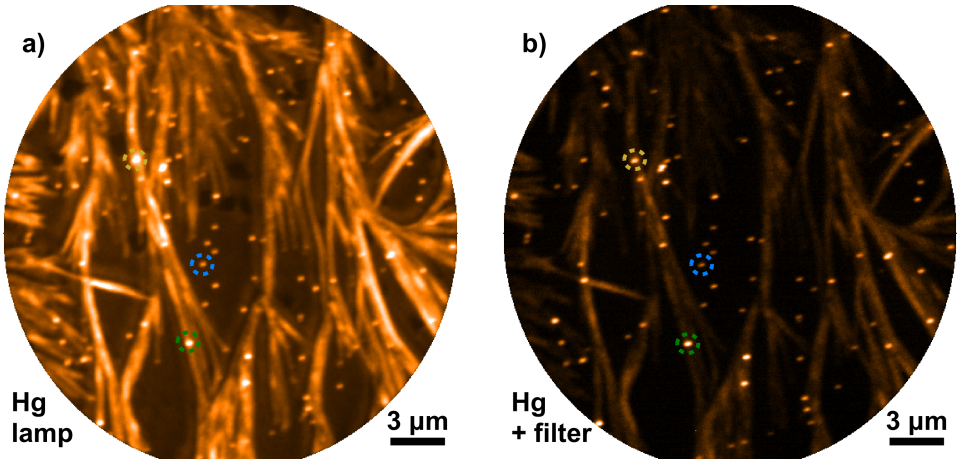

Figure 6.5: Total electron yield PEEM images (FoV: 25 µm) of CuTUP aggregates on silicon with subsequently deposited silver nanoparticles. Brighter colors correspond to higher photoelectron yield. Illumination with a) full spectrum and b) filtered light of a mercury lamp. The bright dots are attributed to the clusters while the molecules have formed strands. See text for details.

6.2.2 LASER EXCITATION WITH FS LASER PULSES

We start with p-polarized fs laser pulses at a wavelength of 266 nm to reproduce the enhancement under well defined excitation conditions. Figure 6.6a shows the respective PEEM image of the same sample location. Please note that the image is slightly rotated due to the use of the DLD. The particles under inspection have been marked in accordance to Figure 6.1a. The apparent averaged photon order is 1.02 which will be important for later discussions. At a first glance the image looks similar to the one under mercury lamp excitation (Figure 6.5a). Under closer inspection slight variations of the intensity between different particles are visible which was not present before. In addition, the particles on the molecular aggregates are no longer necessarily striking bright. Quite the contrary seems to be the case for the yellow marked silver nanoparticle for example. Analyzing this more quantitatively, the enhancement disappears for the green marked cluster with a gain of 1.03 and even inverts for the yellow marked particle with a gain of 0.36.

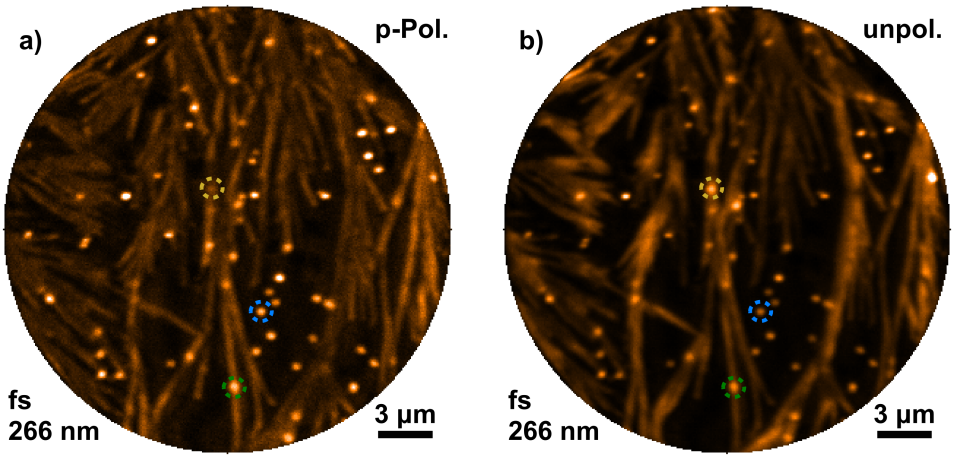

Figure 6.6: Total electron yield PEEM images (FoV: 25 µm) of the same region and the identical marked particles as shown in Figure 6.5 under fs laser illumination with 266 nm wavelength. In a) the incident light was p-polarized while in b) different polarizations were accumulated to simulate a non polarized light source. See text for details.

Let us shortly summarize what changes we made leading to the disappearance of the observed enhancement. Three properties of the excitation light have changed; we narrowed the spectrum from broadband illumination to almost a single line, we have shortened the pulse duration from infinity (cw illumination) to roughly 200 fs, and we used p-polarization instead of randomly polarized light. Since we already narrowed the excitation spectrum with a filter before (cf. Figure 6.5b) which has enhanced the effect, this seems not to be the obvious origin of its disappearance, although it can not be strictly ruled out. The influence of the pulse duration was easily checked by using a cw laser with 266 nm wavelength which has shown a very similar photoemission contrast (image not shown) compared to fs laser excitation at the same wavelength. Therefore, the presence of different polarizations in the mercury lamp illumination seems to be the most supposable candidate to reproduce the observed enhancement. To obtain an overview of the polarization properties images at six different polarization angles φ have been recorded and summed up to the image shown in Figure 6.6b[2]. The appearance of the molecular aggregates has changed since some branches became highlighted which were not that pronounced under p-polarization. This high sensitivity of the porphyrins on the polarization of the exciting light was already known from previous studies [11, 69, KO-2]. As elaborately discussed in Chapter 4 clusters on a bare silicon substrate have shown a $\cos^4$ dependence in 2PPE photoemission with the maximum yield at $\varphi = 90°$ (p-pol.). In average this is leading to a slightly darker appearance of the clusters on the background for mixed polarizations compared to pure p-polarization in Figure 6.6b. However, the enhancement can be quantified by a gain of 1.25 for both marked nanoparticles. Hence, the apparent enhancement has its origin in the polarization dependency of the sample. Before we take a closer look on the total electron yields as a function of φ, let us investigate the kinetic electron spectra to gain further information on the origin of the photoelectrons being responsible for the enhancement.

6.2.3 ELECTRON SPECTRA

Photoelectron spectra extracted from the artificial measurement including different polarizations under fs laser illumination with 266 nm wavelength (Figure 6.6b) are shown in Figure 6.7 as a function of the electrons' kinetic energies. The transformation from ToF to E_{kin} was done for the signal originating from regions where silver nanoparticles are on the flat background (blue curve) because this process is well known from the investigations in Chapter 4. Due to considerable differences in the local work functions on the sample an inhomogeneous potential landscape just above the surface is established. As a consequence, emitted photoelectrons can be affected after the emission process due to local field differences. Hence, the apparent kinetic energy extracted from ToF data is no longer necessarily equal to initial energy right after photoemission. Therefore, also negative kinetic energies can occur due to a retardation in the potential landscape. However, we can use the axis to identify different contributions to the spectra. The black curve in Figure 6.7 is averaged over the whole image showing two peaks. The low energetic peak at $\approx -0.5\,\text{eV}$ is dominating the spectrum although the second peak at $\approx 0.1\,\text{eV}$ is clearly visible. By spatially extracting spectra from different areas, contributions from isolated clusters (blue curve), CuTUP without nanoparticles (red) and the background (green) can be analyzed. Note that the intensities are not directly comparable (different areas) and do not sum up to the complete signal because some intermediate areas were not considered. The strong low energetic peak of the complete signal does overlap with the porphyrin signal showing a strong peak at those energies,

2 An exact reproduction is not possible due to the differences of the geometric alignments of the used incouple windows around the azimuthal angle of the sample.

with a wide tail until almost 2 eV leading to a similar width of the black and red spectrum. The cluster and the background signal show much narrower curves with peaks at ≈ 0.2 eV.

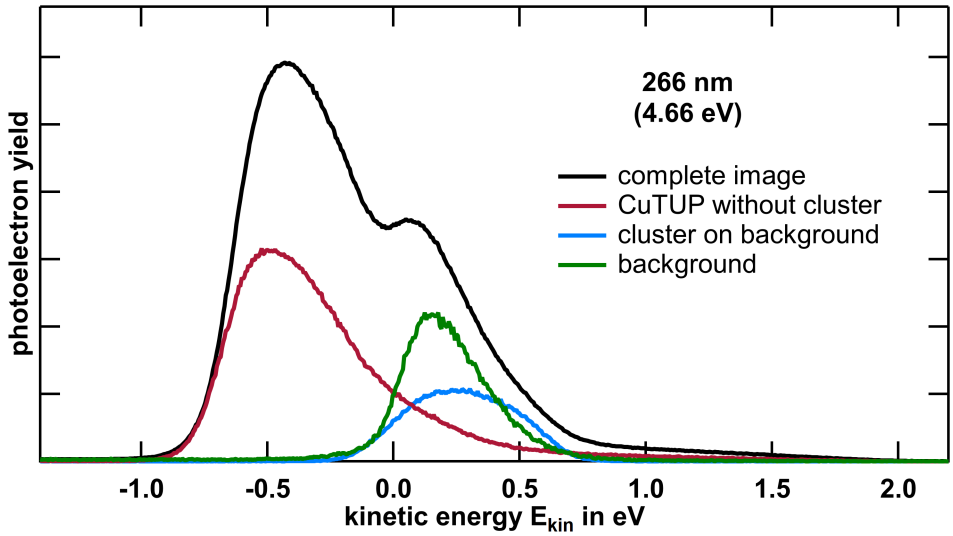

Figure 6.7: Photoelectron spectra of Figure 6.6b as a function of E_{kin}. The main contributions to the overall spectrum (black curve) are shown by spatially separate CuTUP (red) from cluster (blue) and background signal (green). Apparent negative kinetic energies are further discussed in the text.

As we have seen we can distinguish cluster from molecular signal due to different spectral shapes. We now want to utilize this finding to further analyze the apparent enhancement we observed from locations where a silver nanoparticle lies an top of a CuTUP aggregate. Therefore, we superimpose spectra of a reference cluster (blue marked in Figure 6.6b) and the CuTUP signal on the strand in direct vicinity of the clusters under investigation (green and yellow marked). Figure 6.8 shows the results of this approach. The blue curves show the signal of the reference cluster while the red ones are the respective porphyrin signals. In Figure 6.8a the photoemission yield of the yellow marked particle is shown (yellow curve) together with the best possible superposition of cluster and molecule signal (black curve). While the high peak can be reproduced well in this approach some differences occur at the higher energetic tail of the curve. For the green marked particle (green curve) shown in b) the situation is even more obvious. The combined signal can not be reproduced by a superposition of both individual signals. Here, a dip in the superposition remains which is not present in the recorded trace. Taking a look at the contribution of the cluster and the molecules to the combined signal, we can observe a strong increase by a factor of ≈ 2.6 of the molecular signal in both cases while the cluster contribution is apparently shrunken compared to the reference cluster signal to 0.25 (yellow, a) and 0.5 (green, b), respectively.

These observations will be further discussed on Page 93 where the contributions are mainly attributed to an artificial effect due to the inhomogeneous potential landscape.

After these polarization averaged investigations we now want to study the actual polarization dependence of the obtained photoemission yields especially to solve the nature of the observed enhancement.

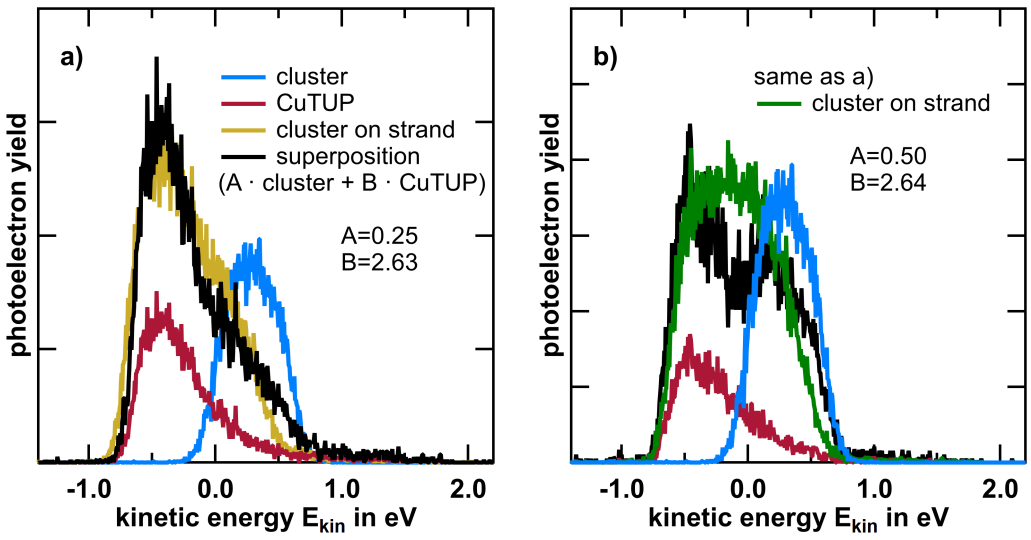

Figure 6.8: Simultaneously recorded photoelectron spectra of various spatial areas of the same sample. The yellow and green curves correspond to the respectively marked nanoparticles (see Figure 6.1a). Curves are shown together with the spectrum of the blue marked reference cluster (blue curve) and spectra obtained on the strands just beside the according nanoparticle (red curves). The black curves are weighted superpositions of cluster and CuTUP signal to best fit the combined photoelectron yield.

6.2.4 DEPENDENCE ON POLARIZATION

Before we analyze the dependence on the incident light field's polarization, we first try to get an impression how the PEEM image changes when switching from p- to s-polarized light as shown in Figure 6.9. The image acquired at p-polarized excitation (Figure 6.9a) was already shown before, for comparison it is shown again together with the measurement obtained with s-polarized illumination (b). The appearance of the image changes drastically. Most of the clusters have nearly vanished, those being visible are located on a CuTUP strand. The molecules show a more inhomogeneous intensity distribution. Some branches are highlighted while others are hardly visible. This behavior was observed in previous studies [11, 69, KO-2] and can be attributed to the exclusive presence of the in-plane (parallel to the substrate) component of the electric field, leading to an effective selection of photoemitting aggregates depending on their inner structure. Whereas the marked particles show diverse behaviors. While the yellow marked cluster is more pronounced under s-polarized illumination, the green marked one seems to emit more efficient under p-polarized excitation. Interestingly, this dependence is preserved for the underlying molecular branch, so it seems that the porphyrin emission is governed by the presence of the particle. Therefore, we want to study these particles in more detail.

Figure 6.10a shows the photoelectron yield as a function of the polarization angle φ for the reference cluster (blue), the yellow marked particle, and the CuTUP signal in close vicinity. The same for the green marked silver cluster is shown in b). The reference nanoparticle shows the well known behavior from a cluster on a bare substrate as seen in Chapter 4. Instead, the CuTUP exhibit a polarization dependence where s-polarization is preferred for the strand of the yellow marked but p-polarization for the green marked one, respectively. While in b) the combined signal follows roughly the sum of both individual contributions, the particle analyzed in a) shows a complete antagonistic behavior. Here the yield of the yellow marked cluster seems to follow the porphyrin signal in an enhanced way and is even lower than the signal of the reference cluster for p-polarized excitation.

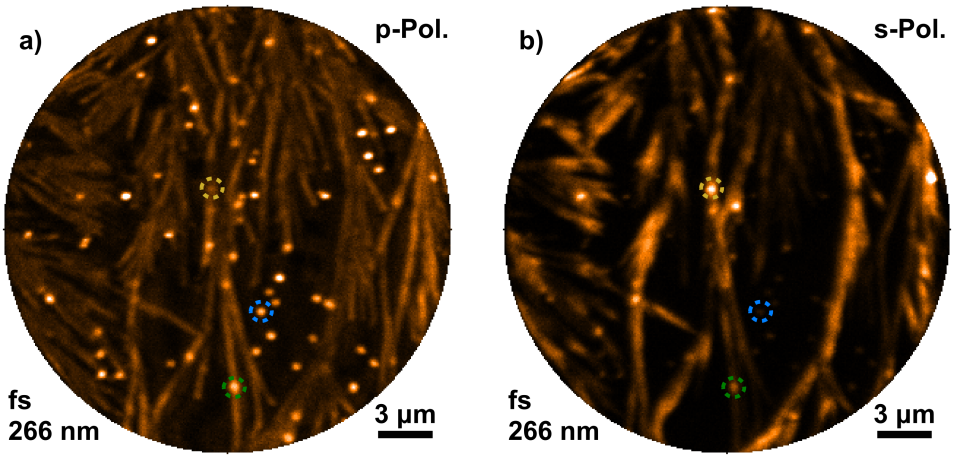

Figure 6.9: Total electron yield PEEM images (FoV: 25 µm) under fs laser illumination with 266 nm wavelength using a) p-polarized and b) s-polarized incident light, respectively. The images show the same region and the identical particles marked in Figure 6.5.

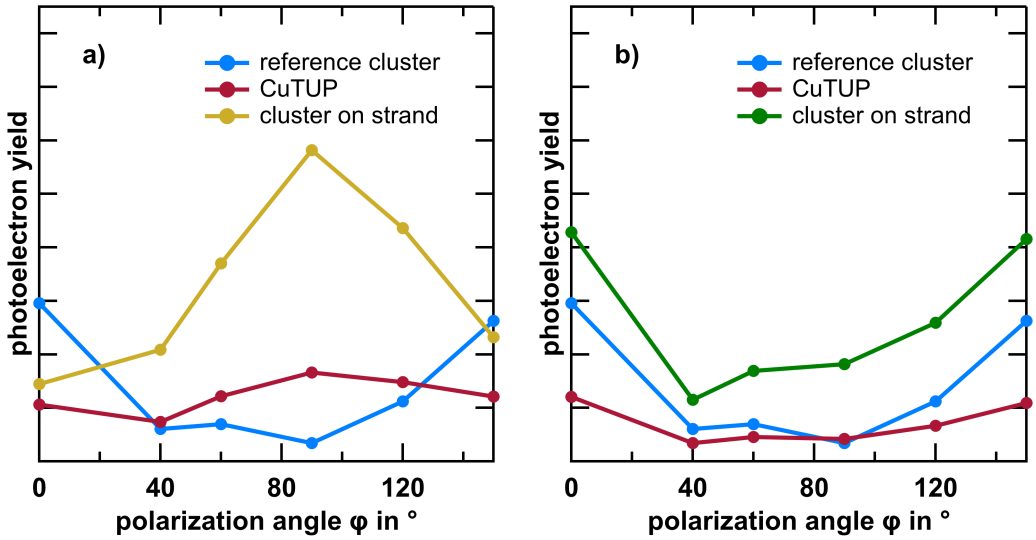

Figure 6.10: Photoelectron yield as a function of the polarization angle φ of the incident light field ($\varphi = 0\,^\circ$ corresponds to p-polarization) for the reference cluster (blue) and a) the yellow marked nanoparticle (yellow) and the CuTUP signal from the respective strand (red) b) same for the green marked nanoparticle. Lines are drawn to guide the eye.

With this data we easily can calculate the total enhancement factor as described earlier as a function of φ as shown in Figure 6.11. The enhancement for both particles under investigation is most at s-polarization and decreases monotonically to p-polarization. While for the green marked cluster the minimum gain is around 1, the enhancement of the yellow marked nanoparticle reduces significantly below 1 which means that the combined system of cluster and porphyrin emits less electrons than separately.

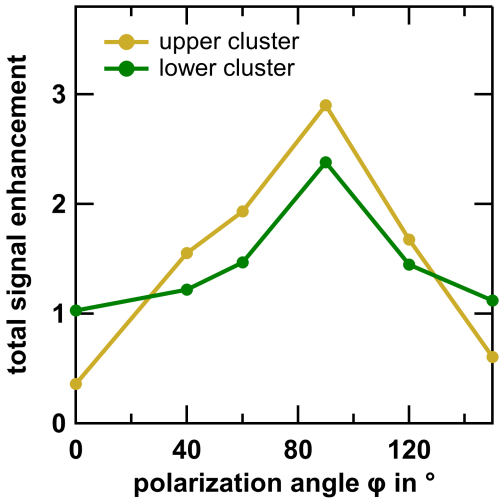

Figure 6.11: Total signal enhancement of the marked nanoparticles as a function of polarization angle φ of the incident light field ($\varphi = 0\,^\circ$ corresponds to p-polarization). Lines are drawn to guide the eye. See text for details.

6.3 DISCUSSION

We now want to classify the observations and conclude by combining the results of different measurements. Since CuTUP strands on HOPG have been extensively studied by PEEM [69, KO-2], these studies will give us important information and will allow certain inferences for the molecular system without influence of the silver nanoparticles.

Calibration of Kinetic Energies from Time-of-Flight Data for Heterogeneous Systems

In Figure 6.7 we have seen photoemission spectra as a function of E_{kin} for different contributions of the signal. Using the cluster signal for conversion of the ToF axis to the energy scale, negative kinetic energies appear for the porphyrin signal. Qualitatively this can be understood by the following considerations. The conversion from time to energy (cf. Appendix A.5) uses the sample's work function W_{sample} as an input to determine the potential difference between sample and detector, i. e. the amount of energy an emitted electron loses while traveling towards the detector. For energetically heterogeneous samples, e. g. with spatially varying work functions, the potential acting on the electrons depends on the position the electron is emitted. Therefore, this simple conversion method is leading to obviously incorrect kinetic energies. An exact description considering locally different vacuum levels, Fermi level pinnings, or charging of the sample would exceed the frame of this work. Nevertheless, the observed spectra can be used for interpretation without using absolute energetic values or directly compare signatures at different sample locations.

Superposition of Spectra

For the above mentioned reasons the ansatz of superimposing spectra from a typical cluster and CuTUP signal gives misleading results. In Section 6.2.3 it seems to be the case that electron emission from the molecules is strongly enhanced while clusters' emission is suppressed. This can simply be explained by a relative energetic shift of the cluster signal when the electrons are emitted from the potential of porphyrin locations compared to the reference where the nanoparticles are on the flat surface. As a consequence the spectra shift to lower apparent kinetic energies which is towards the maximum of the porphyrin signal leading to an apparent increase of that signal and a decrease of the cluster signal.

Energetic Level Scheme

For a better understanding of the ongoing emission processes an energetic level scheme is presented (Figure 6.12) which is mainly based on [KO-2]. Above the ground state (S_0) we have the Q- (S_1) and the strong absorbing Soret band (S_2), which can undergo an intersystem crossing into triplet states (T_1). The triplets split into radiating and non-radiation "dark" states (see [KO-2] for details). Especially the dark states are expected to saturate explaining the observed photon order of 1.02 despite an actual two-photon process. The ionization potential (IP) was measured to be $\approx 5.2\,\text{eV}$ for CuTUP on HOPG. However, here we can estimate an IP in the range of $\approx 5.5\,\text{eV}$ extracted from the width of the spectra taken at fs illumination at a wavelength of 266 nm. For this, only locations with bare CuTUP were analyzed and the energy axis was scaled to this signal. For the above mentioned reasons the potential above the surface can still be influenced by the inhomogeneous sample, resulting in a slight distortion of the value. The spectrum shows a long tail with very little signal probably originating from emissions out of the singlet system as illustrated by the narrow arrow in Figure 6.12. However, in [69] a second model for the level scheme was presented with an IP in the range of $3.5\,\text{eV} - 4.0\,\text{eV}$ which could not be ruled out completely although an IP of $\approx 5.2\,\text{eV}$ was favored in that work. The alternative model mainly based on the observation of a photon order of 1 under illumination with 266 nm wavelength, which could only result in the above shown 2PPE model when one subprocess is saturated [216]. Here we observed exactly the same for fs laser illumination, but under cw excitation with the same wavelength the apparent photon order was measured to be 1.47 (not shown) which safely rules out the alternative model at least for this system. Due to different focus settings of the measurements the intensities are not comparable but the laser power was in the same order. However, on average the cw laser seems not to saturate the intermediate state leading to this enhanced photon order.

Patches

In the PEEM image shown in Figure 6.5a some dark patches on the homogeneous emitting background were visible. This could be easily misinterpreted as a missing part of a background layer while AFM has unambiguously shown that there is additional material. This allows the conclusion that the patches are thin porphyrin layers which is confirmed by spectra taken from these regions showing a comparable signature as the CuTUP strands. From the height of the patches we can conclude that the islands consist of more than one monolayer. In contrast, the background spectrum strongly reminds of a bare silicon emission which would explain the stronger photoemission since the substrate can undergo a direct 1PPE process and the density of states should be large compared to the molecular states involved. However, this does not rule out the existence of a monolayer as it is formed on HOPG [68, 69, 215].

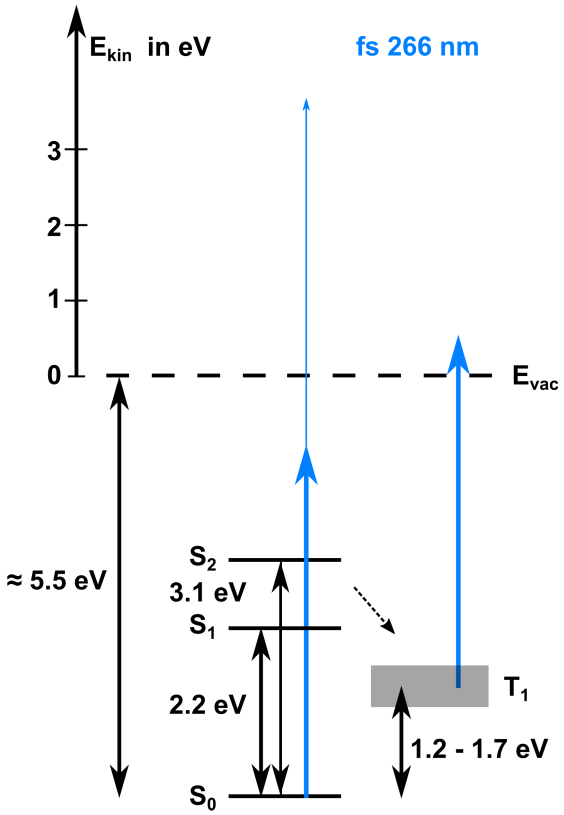

Figure 6.12: Schematic illustration of the energy levels of CuTUP with possible excitation pathways (blue arrows) with a fs 266 nm laser. Figure adapted from [69, KO-2].

Origin of the Observed Photoemission Enhancement

Finally, we discuss the observed photoemission enhancement under certain excitation conditions at positions where clusters are located on CuTUP aggregates. Several possibilities exist when the particle is exposed on top of a molecular crystal, e. g. a reduction of the porphyrin's work function, plasmonic near-field coupling, field emission scenarios, an enhanced density of trap states in the CuTUP, or just simple geometric arguments. The list could be continued with a lot of more exotic arguments or indirect higher order processes. However, the observed polarization dependence immediately rules out the work function and field emission arguments. The presence of the effect at 266 nm wavelength eliminates explanations based on particle plasmons. A higher density of trap states due to the distortion of the crystal lattice due to the presence of the nanoparticle is conceivable, however, these trap states must be assumed to have a peculiar polarization dependence. This can not be ruled out completely but is expected to be very unlikely because of the commonly anticipated disordered nature of trap states.

In contrast, simple geometric arguments are able to explain all the observations and support the apparent enhancement. Since the effect is highly polarization dependent, let us start with the used reference cluster's electron yield as a function of polarization angle (blue curves in Figure 6.10). We can see the ratio of the electron yield between p- and s-polarized illumination to be slightly below 9. This is a direct consequence of the geometry of the PEEM setup with an angle of incidence of $\theta_i = 65°$ to the surface normal. Figure 6.13 shows the square modulus of the irradiating field $|\mathbf{E}_i + \mathbf{E}_r|^2$, which is the superposition of incoming $\mathbf{E}_i$ and from the surface reflected field $\mathbf{E}_r$ for a silicon oxide surface (see Appendix A.9 for derivation within Fresnel-type considerations) as a function of the distance d to the surface. The plot shows that the waves interfere destructively just above the substrate for s-polarization while the field is much more homogeneous

for p-polarization, which is also in accordance with the appearance of the PEEM images in Figure 6.9. The ratio of both curves is plotted in Figure 6.13b, where we can observe a value of ≈ 3 for a cluster on the substrate. Since the oxide layer is only a few nm thick, we expect the bare silicon underneath to have an influence as well. Due to the higher permittivity of silicon a stronger effect is expected which is in accordance with the observation and results in a strong preference of photoemission with p-polarized excitation for the reference cluster. By increasing the distance of the nanoparticle to the surface this preference is decreased and can even flip at around 65 nm above the surface. Hence, nanoparticles lying elevated on molecular aggregates are excited by a completely different light-field, the usage of a cluster on the substrate as a reference is only meaningful in p-polarization. Here, we observed a gain of ≈ 1 for the green marked particle (cf. Figure 6.11) which is in perfect agreement with theory. Surprisingly, for the yellow marked cluster the enhancement is below one. One possible explanation lies in the detection side. For p-polarized illumination we expect the dominant electron emission to the upper right side of the images (in line with the excitation)[3]. The inset of the AFM image in Figure 6.3a shows that the aggregate becomes higher in that direction, thus hindering the electrons from reaching the detector if the initial emission direction is rather grazing[4]. For s-polarization we observe an enhancement for both particles which is in accordance with a stronger photoemission from the particles compared to the used reference particle due to their elevated position. From the AFM images we can determine the heights of the branches to be around 20 nm (green marked particle) and 35 nm (yellow marked particle), respectively. This is consistent with the stronger enhancement of the yellow marked cluster (cf. Figure 6.13a).

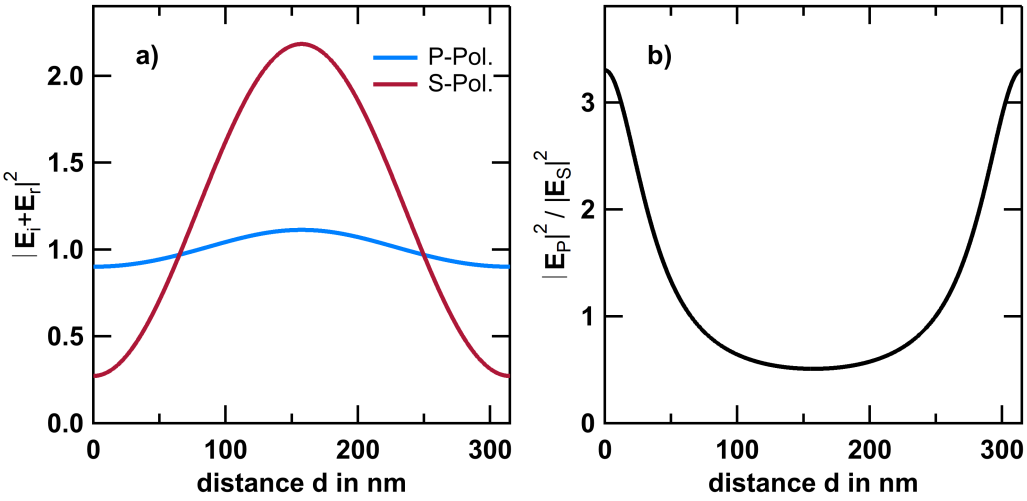

Figure 6.13: a) Square modulus of the irradiating light field as a function of distance from the sample's surface for excitation with 266 nm wavelength for p- (blue curve) and s-polarization (red curve). Under s-polarization incident and reflected beam interfere destructive at the surface but constructive around 150 nm above the surface while for p-polarization the variations are much weaker. b) Ratio of the curves shown in a).

When just focusing on the molecular signals in Figure 6.10, we see opposite behaviors of the two analyzed strands. While the higher one is emitting more electrons under s-polarization, the lower one prefers p-polarization. With the presence of the nanoparticles this trend is enhanced, which could bring us to the conclusion that the exciting light

3 This has also been confirmed by doing measurements in k-space mode, where the distribution of emission angles is imaged. It has been shown that the emission angle can be controlled to a certain amount by the polarization. See Appendix A.7 for further information.

4 Note that the electron trajectory is governed by the strong extraction field.

field is stronger in the according polarization. Referring to Figure 6.13b the lower strand would be at a ratio above one while the higher aggregate is excited by a ratio below one. By just taking the distances shown in the calculation this is not in accordance with the AFM measurements, but as stated before this model gives just a qualitative impression and the lengthscale might change due to the specific behavior of the substrate and the presence of the molecular aggregates themselves which on the one hand increased the optical path for the light, and on the other hand influenced the field by their dielectric properties. This is described in more detail within a multi reflection model elsewhere [11]. In addition, the emission is also influenced by the transition dipole moment of the molecules which has to overlap polarization-wise with the excitation. Since the in-plane component of the light-field rotates when changing the polarization the actual inner structure plays an important role as was shown in previous studies [11, 69].

Excitations at other Wavelengths

The initial idea was to excite the molecules in the vicinity of nanoparticles resonantly utilizing their plasmonic properties. However, images acquired around 400 nm wavelength where the absorption of the molecule overlaps with the plasmon resonance do not show any signature of the nanoparticles at all due to an extremely strong absorption of the molecules. Only at higher wavelengths some clusters having a strongly red shifted resonance appeared bright without a noticeable coupling to the molecules. Another possibility to look for an interaction would be a wavelength scan which was successfully done for silver particles covered by ZnTPP [103]. Hence, the plasmonic coupling is not evident based on these data which does not exclude its existence since a potential signal may have been just masked by the enormous yield of the CuTUP when exciting the Soret band.

6.4 CONCLUSION

In this chapter the photoemission of silver nanoparticles on and between strands of CuTUP aggregates was studied. The organic molecules were drop casted onto a silicon wafer with native oxide layer. The concentration of CuTUP in the solution was optimized to build cable like structures possibly allowing directional exciton migration processes. After preparation, size selected silver nanoparticles with a height of ≈ 9 nm were vacuum deposited onto the sample. A strong signal enhancement from areas where nanoparticles are exposed on CuTUP strands was visible. By analyzing the polarization dependence of obtained electron spectra and images, the effect was attributed to a pure geometrical origin.

Nevertheless, with this knowledge it becomes possible to beneficially use the different heights of the strands to place plasmonically active nanoparticles on top and selectively excite them by selecting a geometry of the incident light which leads to constructive interference where desired.

Although a plasmonical coupling was not observed, it can not be excluded due to a potential masking of the signal by the strong emission of the CuTUP. There are several possibilities to avoid this circumstance. By exciting parallel to the transition dipole of the Soret band the absorption would be minimized, however, due to the plasmonic near-field of the nanoparticles on top, the molecules could absorb photons of the enhanced near-field. Another possibility is the excitation above the Soret transition using nanoparticles with a blue shifted resonance.

Due to the results of this work, we can safely rule out an alternative scenario used in a prior work [69].

7 COMPARATIVE DISCUSSION AND OUTLOOK

One aim of this thesis was to utilize small metallic nanoparticles as far-field near-field couplers to selectively and locally excite aggregates of organic semiconductors. This enables an energy transport from a macroscopic light field into a nanoscopic semiconducting structure where possible exciton migration processes can transfer the energy on a pathway defined by the molecules' morphology.

In this chapter the main results are highlighted in a condensed fashion. We start with a short summary of the key findings of Chapter 4 studying the optical and electronic properties of silver nanoparticles with respect to their local dielectric environment. Afterwards the obtained hybrid systems involving tetracene (Chapter 5) and CuTUP (Chapter 6) are comparatively discussed, and an outlook with proposals for future experiments is given. For detailed summaries of the individual parts take a look at the respective conclusions of each chapter.

In the first part of this work (Chapter 4) supported silver nanoparticles were characterized which is demanding due to the low extinction cross-section of individual nanoparticles. By using the sensitivity of two-photon photoemission electron microscopy to the fourth order of the local electric field the plasmonic properties were successfully studied. We saw a crucial dependence of the overall light absorption characteristics on the dielectric properties of the surface which not only results in a simple shift of the plasmon resonance. Instead, completely new hybridizing plasmon modes appear. In addition to these changes of the ensemble behavior, the individual properties of each particle scatter around the global trend with shifts up to 200 meV in the resonance energy depending on the detailed local geometry and coupling. This highly sensitive dependence opens the perspective of several sensing applications on the atomic scale and shows that the nanoparticles' plasmonic properties need to be addressed individually in this size range. The local field enhancement which is the key requirement for a sufficient far-field near-field coupling was found to be in the order of 10. Further fundamental mechanisms could be analyzed using the spectral signatures detected by ToF measurements. Amongst others, an efficient Landau damping in the particles could be shown in combination with a preferred photoemission out of a relaxed intermediate state. Since plasmonic response may also lead to further interactions such as electron hole generation, this opens the route towards single particle SPV measurements. Resulting potential landscapes have impact far beyond cluster and surface science, one example being the role for field-assisted adhesion of living cells [217] which is being investigated within the framework of the Collaborative Research Center 1270 Elaine.

In a second step we used the nanoparticles and especially the local field enhancement to locally excite organic molecules. Here, we used tetracene and CuTUP as promising candidates. Under certain requirements it was possible to distinguish between cluster photoelectrons and molecular photoelectrons in the CuTUP system due to different energetic levels of the molecule compared to tetracene where the respective electronic levels overlap. Surprisingly, we observed blinking behavior in the photoemission intensity with very similar appearance as well-known luminescence blinking. Further analysis may shine light on responsible mechanisms such as local trapping or gating. On the other hand, blinking prohibited a spatially resolved analysis in some cases for tetracene while no respective signatures were observed for the porphyrin structures. The morphologies of both samples were completely contrary. The dropcasted CuTUP formed large, anisotropic branching structures with a high stability. The tetracene instead was studied as a thermal evaporated film which reduced to only a few layers with dendritic islands

and a potentially higher disorder upon initial examination in PEEM. Since triplet excitons are most promising for long range migration processes the aim was to highly populate these states which in general is spin forbidden in molecular systems. However, in the case of CuTUP this inter-system crossing is allowed and leads to a high triplet population which can even go in saturation upon illumination at the Soret band superimposing with the plasmon resonances of the used particles. For tetracene the plasmon resonance is far away of the absorption maximum, instead singlet fission becomes most effective at the resonance efficiently populating the triplet states. A benefit from the presence of the nanoparticles and therefore a coupling to the molecules was only detected for tetracene where an increased triplet population in the vicinity of the silver clusters was detected. For CuTUP a possible coupling was masked by the enormous absorption of the Soret band and possible saturation effects. However, an enhanced photoemission of the nanoparticles positioned on the strands was observed due to geometric reasons. The triplet state lifetime of this kind of CuTUP aggregates was studied before [KO-2] and showed some long living dark states with a lifetime of several ten µs without much spatial variation within the same aggregate. In the tetracene layer studied in this work, states with a comparable lifetime were detected and could be qualitatively mapped showing high spatial variations with especially long lifetimes at the edges of the dendritic islands. Although long triplet exciton migration ranges were observed for tetracene in literature [9], no spatially resolvable migration was detected. However, clear characteristics of exciton-exciton annihilation (here triplet fusion) were seen requiring a sufficient mobility of the excitons. In contrast, no signatures suggesting migration processes were observed for CuTUP, which does not exclude its presence. Especially due to the potentially missing coupling between nanoparticles and molecule aggregates the excitation could be too homogeneous to see specific migration features.

Since all key requirements for a long range exciton migration are fulfilled in tetracene and also signatures of short range migrations are observed, it is a promising pathway to continue. The prospects of adjusting the migration length by changing the morphology are excellent since a dependence was already reported [9]. In addition, the FLIM measurements showed a similarly long lifetime for large crystalline structures as observed in PEEM for the thin inhomogeneous layers. Hence, using these larger dropcasted structures is a promising pathway. In addition, during dropcasting also smaller branch-like structures evolve possibly enabling a more directional energy transport. Once successfully prepared structures with a sufficient migration length, the morphology could possibly be adjusted to the specific aims by means of lithographic techniques or nanografting. To temporally resolve the exciton migration a two color pump-probe PEEM experiment would be promising. The first pulse should excite the plasmon resonance of the metal nanoparticles and the second pulse probes the population of the tetracene ideally in a 1PPE and under non-resonant conditions to avoid possible blinking which could occur at typical resonance wavelengths. In the case that a sufficient stability of the aggregates is not given, a possibility would be to use tetracene derivatives like TIPS-tetracene which has similar electronic properties.

APPENDIX

A.1 OVERVIEW OF THE ANALYZED SAMPLES

The following tables give a short overview of the main samples used in this work.

Chapter 4	Sample A	Sample B	Sample C
Substrate	Si(111) + native oxide n-type (As) $< 0.01\,\Omega$cm	Si(111)-(7x7) n-type (As) $< 0.01\,\Omega$cm	Si(111)-(7x7) n-type (As) $< 0.01\,\Omega$cm
NP Height	$\approx 10 - 35\,$nm	$(10.9 \pm 1.6)\,$nm	$(25.5 \pm 1.8)\,$nm
NP Density	$\approx 2\,\mu m^{-2}$	$\approx 0.3\,\mu m^{-2}$	$\approx 0.3\,\mu m^{-2}$

Table A.1: Overview of the samples analyzed in Chapter 4. The nanoparticle (NP) heights and densities were obtained by AFM.

Chapter 5	PEEM Sample	FLIM Sample
Substrate	Si(111) + native oxide n-type (As) $< 0.01\,\Omega$cm	microscope slide Menzelglass
Molecule	Tetracene	Tetracene
Deposition Method	vacuum evaporation from powder at 135 °C	drop casting 5 µl droplet, $9 \cdot 10^{-4}$ M (toluene)
NP Height	$\approx 15\,$nm	-
NP Density	$\approx 0.07\,\mu m^{-2}$	-

Table A.2: Overview of the samples analyzed in Chapter 5. The nanoparticle (NP) heights and densities were obtained by AFM.

Chapter 6	PEEM Sample
Substrate	Si(111) + native oxide n-type (As) $< 0.01\,\Omega$cm
Molecule	CuTUP
Deposition Method	drop casting 1 µl droplet, $2 \cdot 10^{-4}$ M (n-heptane)
NP Height	$\approx 9\,$nm
NP Density	$\approx 0.1\,\mu m^{-2}$

Table A.3: Overview of the samples analyzed in Chapter 6. The nanoparticle (NP) heights and densities were obtained by AFM.

A.2 FUNDAMENTAL PEEM IMAGE PROCESSING

Here, all basic steps that were applied to the acquired images can be found and will be shortly described. Most procedures were already explained in [KO-4].

Dark Counts and Pixel Sensitivity

As a first step, a dark-count image in absence of laser excitation was subtracted from all images. To correct for varying sensitivity of each pixel (e.g. "hot" pixels) a defocused image was acquired and smoothened using a Savitzky-Golay filter. All images were then multiplied by the quotient of the smoothed and the raw defocused image.

Wavelength Scans

To correct for a constant linear thermal drift all images within a wavelength scan were aligned to each other by maximizing the 2D cross-correlations in an iterative scheme. Temporal fluctuations of the laser intensity are corrected using a similar procedure as for the pixel sensitivities: each image is multiplied with the spatially constant quotient of the smoothed and raw total electron yield averaged over the entire images (Sample A) or over all spectra (Sample B and C), respectively.

Extracting and Fitting Spectra

On Sample A the spectra were analyzed pixel-wise while on Sample B and C the particle density was less dense, therefore the analysis could be done for each cluster separately, i. e. by averaging all pixels of the same particle, in order to increase the signal to noise ratio of the spectra. Cluster positions were extracted by 2D Gaussian fits to each particle signal in images averaged over all excitation wavelengths. The resulting spectra were fitted by a sum of two squared Lorentzians to obtain resonance energies and spectral widths of both plasmon modes. To account for atypical outliers and occasionally failed fitting procedure, some of the obtained resonance parameters of both samples were not used for subsequent statistical analysis. To this end linewidth histograms of each resonance were created and data more than 2.5 standard deviations away from the mean value are rejected. The fraction of these outliers is below 5%.

Map of Resonance Energies and Lifetimes

For the maps in Figure 4.3 any spectra with intensity below a certain threshold (positions where no clusters are located) or where the fits resulted in resonance energies outside the available tuning range are not considered and the corresponding areas appear black.

Correlation of PEEM and AFM images

For Sample A spatial correlation between PEEM and AFM images was done by first extracting the particle locations using a semi-automated particle recognition algorithm. Three particles sufficiently far apart from each other are used for calculating a 2×2 transformation matrix which connects the particle locations from AFM to those from PEEM. Pairs of particle data (height from AFM; energy or lifetime from PEEM) are then identified at a single pixel location using this matrix.

DLD Chromatic Aberration Correction

During ToF measurements the instrument's drift tube needs to have a well defined potential to calibrate for electrons' kinetic energies from the acquired times of flight. Hence, all electrostatic lenses in the drift tube are on the same potential (here, typically 20 V), which is different from pure imaging mode and is leading to a slightly convergent electron beam additionally magnifying the image on the detector. This magnification depends on the electrons' ToF causing a blurred image especially in outer regions as can be seen in Figure A.1a. To correct this effect, we can apply a ToF dependent magnification to the acquired data stack. The optimal magnification was determined by maximizing the contrast of the image within a linear dependence of the magnification on the time axis. The result can be seen in Figure A.1b.

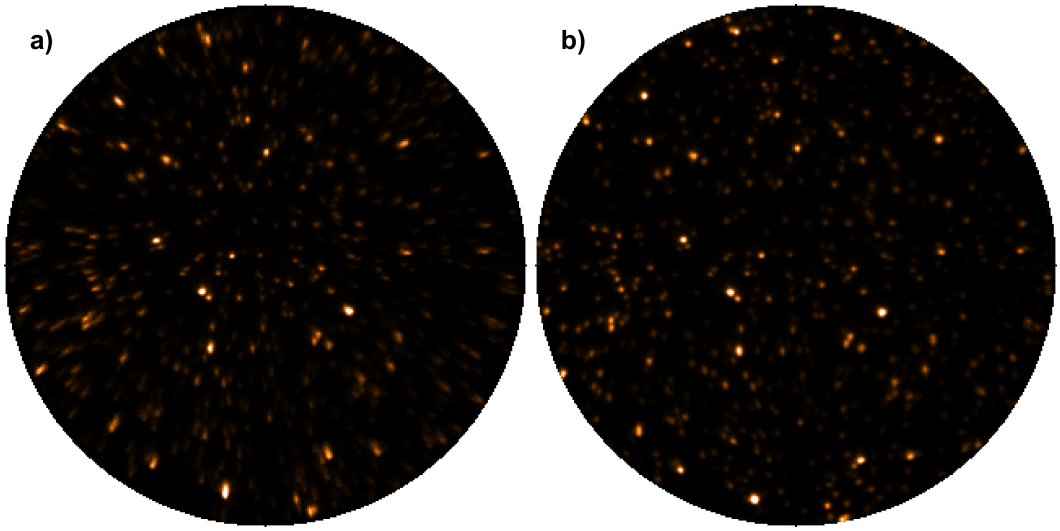

Figure A.1: a) Uncorrected and b) corrected ToF-PEEM images (field of view: 25 µm) under 410 nm fs-laser illumination.

A.3 ANALYSIS OF THE ORDER OF A MULTIPHOTON PROCESS

The photoemission yield Y in a nPPE process follows $Y \propto I^n$ with the laser intensity I. Hence, the order n can be determined by an intensity variation. The analysis was done by first logarithmize both I and Y and subsequently fit the obtained data linearly where the slope gives the order n as can be seen by logarithmizing aboves equation. The more obvious way of directly fitting a power law to determine n does overweight data points with higher intensities and is leading to inaccurate results. For all intensity dependent measurements the DLD was used due to its linearity and low noise. When using CCD images the subtraction of a non-illuminated dark image is crucial since this can effect the apparent photon order by more than 0.5.

A.4 COMPARISON OF P- AND S-POLARIZATION

Here, an analysis showing that we are predominantly sensitive to the perpendicular plasmon modes with respect to the surface (i. e. out-of-plane) is provided which can be partly found in [KO-4]. Due to the geometry of the experiment (p-polarized light excitation with an angle of incidence θ_i equal to 65°) both parallel (in-plane E_{parallel}) and perpendicular (out-of-plane E_{perpen}) electric field components are present. If only the incoming wave is considered the square ratio of both components is $r = |E_{\text{perpen}}/E_{\text{parallel}}|^2 = \tan^2(\theta_i)$.

In the presence of a substrate of high relative dielectric index n (as silicon), the relevant components governing the excitation are the sums of the electric field components from the incoming and reflected plane waves. Actually the substrate modifies drastically the above square ratio through interference effects. For a high index the square ratio in the immediate vicinity of the substrate (height $\ll$ wavelength) is of the order of $n^2 \sin^2(\theta_i)$. Since the magnitude of the absorption cross sections is related to the field intensity (proportional to the square electric field modulus) of the total irradiating field, this ratio allows estimating the respective contributions of the perpendicular and horizontal mode excitations to the overall spectra.

Figure A.2 shows the ratio, computed at the distance $d_{\text{eff}} = 5.5\,\text{nm}$ above the vacuum/silicon interface as a function of photon energy, for different angles of incidence. This figure shows that, for large θ_i, the interference effect is destructive for the in-plane component, pointing out that the excitation of perpendicular plasmon modes is highly dominating.

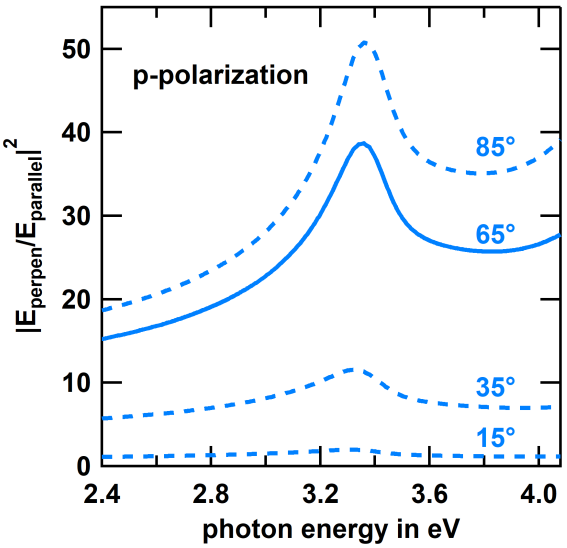

Figure A.2: Ratio of the square moduli of the irradiating field components E_{perpen} and E_{parallel} at the particle center in a distance of 5.5 nm above a silicon surface as a function of photon energy. The perpendicular field component is dominating in the present geometry. (According to [KO-4])

Figure A.3a shows the absorption cross-sections computed for different particle-substrate distances d_{eff}. The most red-shifted peak is due to the dipolar plasmon mode, while higher order multipole modes contribute to additional peaks of increasing weight with decreasing particle-surface distance. The emergence of these higher order modes, although the particle is of sub-wavelength size, results from the hybridization mechanism between the silver particle and its image induced by the strong electrostatic interaction between the electron surface charge densities which develop on the facing surfaces of both spheres (this coupling is indeed very strong in the case of a vertical excitation). All the observed features (red-shifts, multi-peak patterns, transfers of the oscillator strength of the dipolar mode towards the higher order multipole modes, and their evolutions as a function of d_{eff}) are described in great details in [34].

For comparison the absorption cross-section of the system under s-polarized illumination is displayed in Figure A.3b for different values of d_{eff} (angle of incidence equal to 65°, and identical field amplitude E_0 of the incoming plane wave, so the magnitude of the spectra in Figures A.3a and A.3b can be directly compared). Here, only in-plane modes

can be excited which are orders of magnitude weaker. Moreover, the red-shifts of the plasmon modes are much smaller. Two reasons explain the large decrease of the signal. First, due to the large value of the silicon dielectric index, the Fresnel reflection coefficient for s-polarized light is close to -1, so the particle, which is located close to the interface (height $\ll$ wavelength), is subject to a very weak total irradiating field due to destructive interference effects. Second, for in-plane mode excitations, the electrostatic coupling between the induced surface charge densities in the particle and its image is now much weaker as compared to the out-of-plane mode excitation case (there is no hotspot between the facing surfaces of both spheres), and the strength of the hybridization mechanism (and thus the red-shifts) is consequently weakened.

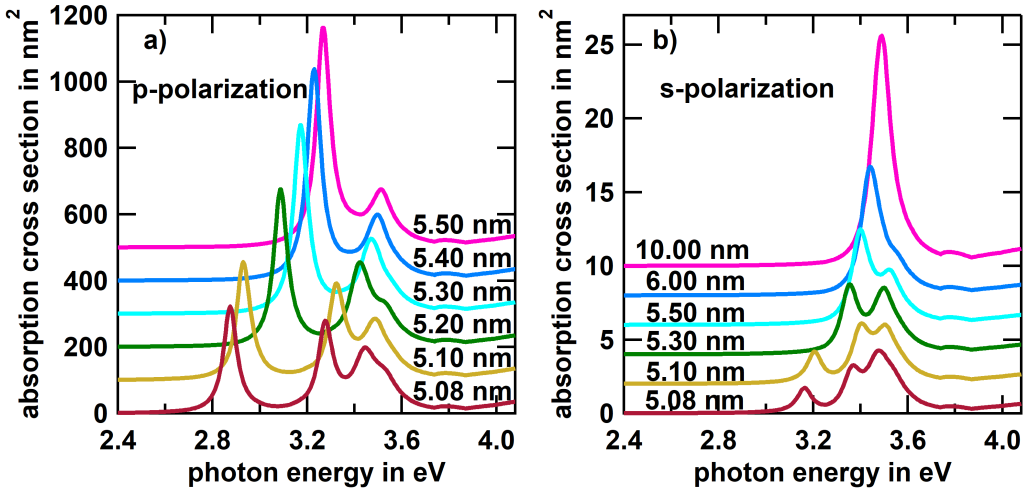

Figure A.3: Calculated absorption cross sections of silver spheres with 10 nm diameter with different distances d_{eff} to the silicon substrate as function of photon energy for a) p-polarized and b) s-polarized incident fields. The curves are offset vertically for clarity. (According to [KO-4])

A.5 CONVERSION OF TIME OF FLIGHT TO BINDING ENERGY AND DETERMINATION OF FERMI LEVEL AND LOW ENERGY CUTOFF IN PHOTOELECTRON SPECTRA

To render a physical interpretation of the acquired three dimensional ToF-PEEM data possible, a conversation of ToF to kinetic or binding energies must be accomplished. For samples with a homogeneous work function this is straightforward and can be found elsewhere [69] including all information needed for this specific instrument. The conversion uses the position of the Fermi edge as reference to assign the respective kinetic energy to this specific time of flight. Therefore the work function must be known, otherwise the low energetic cut off will not match with zero kinetic energy. If the work function is unknown it can be figured out by iteratively varying the kinetic energy at the Fermi edge until the secondary electron cut off is located at zero kinetic energy. Therefore, a determination of the Fermi edge as well as the low energetic cut off is necessary, which was done on a logarithmic scale by finding the intersection of two straight lines fitted at each side of the edge. In principle, one could do it on a linear scale as well by finding half the height of the spectra at the edges. However, this is not always possible since the cutoff is not clearly visible on a linear scale in some cases.

For samples with a significant inhomogeneous distribution of work functions across the surface as for the CuTUP sample this conversation falls short, since the potential difference between sample and detector has a spatial dependence which is not known. For different regions of one sample e. g. patches of a material on a substrate, the conversation could be done separately for each region. However, in the case of CuTUP aggregates the potentials will align depending on, amongst others, the actual morphology and coupling. Therefore, additional forces can act on emitted photoelectrons leading to apparent negative kinetic energies as in Figure 6.7.

A.6 SPATIALLY RESOLVED MAP OF THE ORDER OF THE PHOTOEMISSION PROCESS

In addition to an integrated analysis, the photon order of a nPPE process can be determined in a spatially resolved map as shown in Figure A.4. The colors indicate the photon order n under cw illumination with a wavelength of 266 nm (a) and 405 nm (b) of the tetracene PEEM sample. See Section 5.2.1 for details.

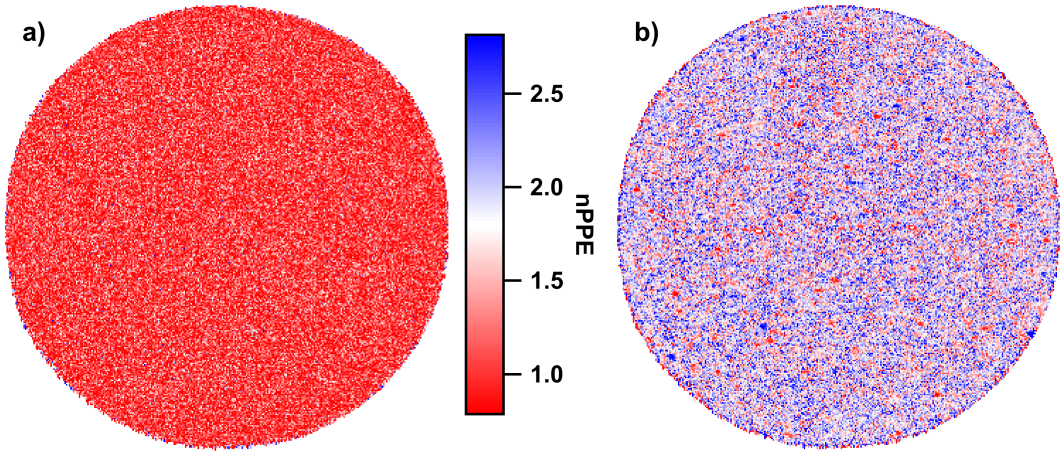

Figure A.4: Spatially resolved map of the photon order n of the nPPE process on the tetracene sample with a cw laser at a wavelength of a) 266 nm and b) 405 nm.

A.7 ANGULAR RESOLVED PHOTOEMISSION MICROSCOPY - K-SPACE PEEM

Apart from utilizing the PEEM in a spatial resolving mode it is possible to use the k-space mode as well where the momentum distribution and therefore the electron emission angle is detected. The analog experimental technique is ARPES where each emission angle needs to be recorded separately whereas in k-space PEEM the acquisition is performed parallel. Figure A.5 shows the obtained data for Sample C under p-polarized fs-laser excitation with 360 nm wavelength. The measurement shows a paraboloid due to the dispersion relation where the parallel momentum is conserved

$$k_{\parallel} = \frac{\sqrt{2m_e E_{\text{kin}}}}{\hbar} \sin\alpha \quad . \tag{A.1}$$

The photoemission yield has a maximum at the vertex of the paraboloid where kinetic energy and therefore the parallel momenta are minimal. In Section 4.2.6 we have assigned these as secondary electrons mainly originating from the clusters as a comparison with

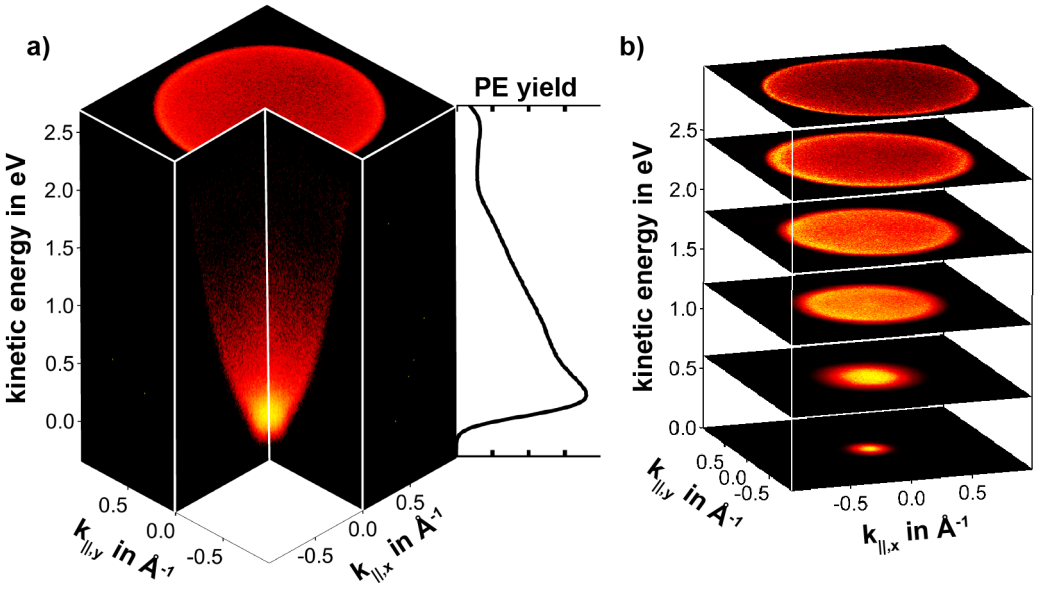

Figure A.5: a) k-Space ToF-PEEM dispersion from Sample C under p-polarized fs laser illumination at 360 nm on a logarithmic colorscale. The planes parallel to the energy axis are cuts through the data. The top plane was integrated from 2.55 to 3.08 eV for better visibility. The spectrum on the right shows the total photoemission yield as a function of E_{kin} integrated over all momenta. b) Equidistant planes from the same data as in a). Every plane is averaged over 0.62 eV and normalized for better visibility.

the spectrum next to the illustration shows. In Figure A.5b equidistant planes from the same data are shown. The top plane can be assigned to the Fermi surface. Upon closer examination we can see an inhomogeneous angular distribution of the electrons at high momenta. More electrons are emitted with negative $k_{||,x}$ than positive while for $k_{||,y}$ it is approximately equal. The only symmetry breaking component is the laser beam. To access a possible influence, the polarization dependence of the electron emission was studied. Figure A.6 shows the Fermi surfaces for several polarization angles. For 0° (p-polarization) the highest emission is detected at a ring with high $k_{||}$ having a maximum in the incident direction of the laser beam, which is parallel to the electric field in this case. For an increasing polarization angle the maximum rotates counterclockwise until 80° which is almost s-polarized. Here, the emission maximum is still along the electric field direction at the side where the component is pointing out of the surface. When passing s-polarization where the electric field in parallel to the surface the maximum of the emission direction flips as the electric field component is now pointing out of the surface on the opposite side which can be seen at a polarization angle of 80°. Afterwards the counterclockwise rotation resumes until a full polarization sweep is done.

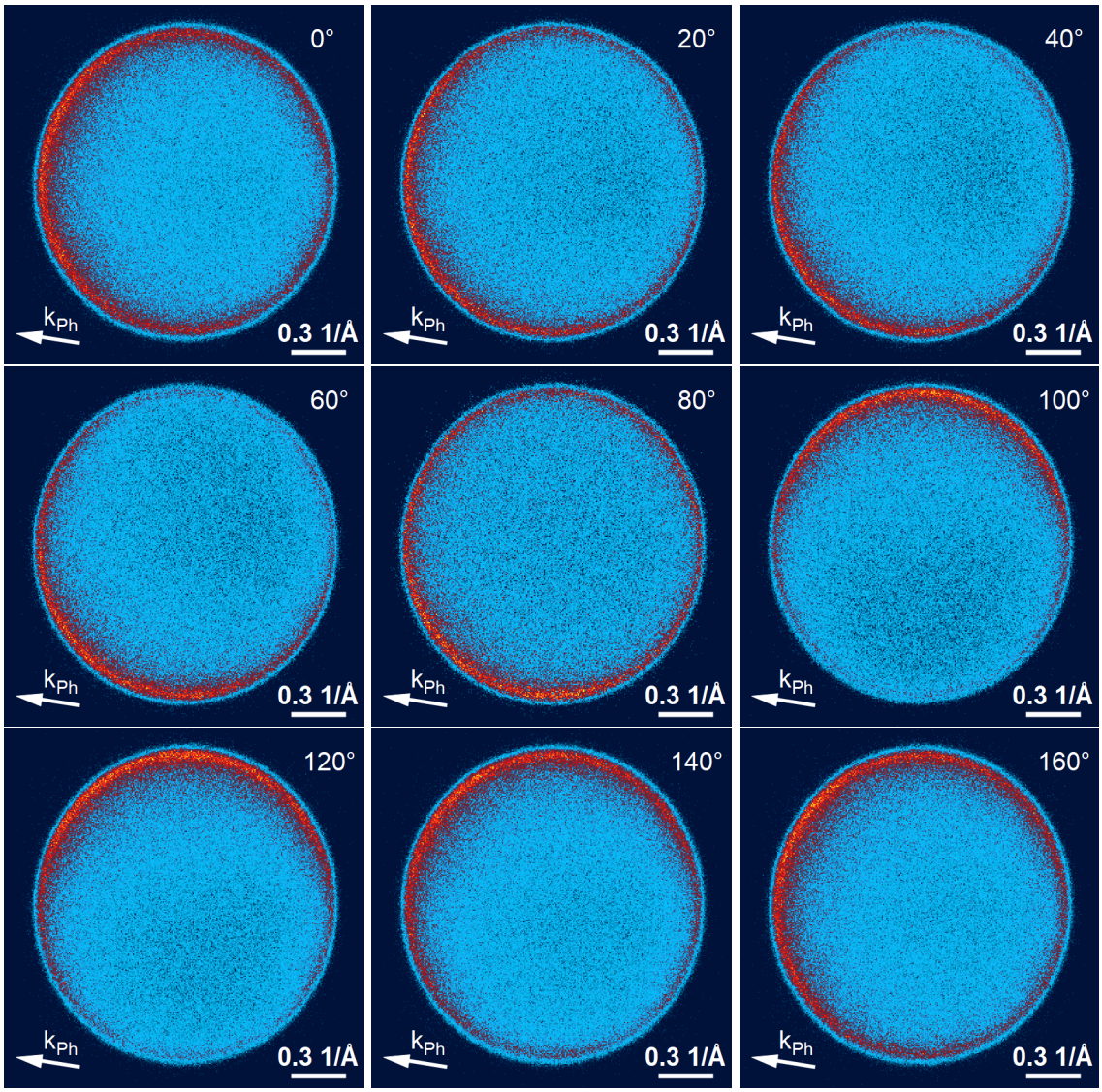

Figure A.6: Fermi surfaces for different polarization angles ranging from 0° (p-pol.) to 160°. The k_{Ph} arrow indicates the light's incidence direction. Red colors correspond to a higher photoemission signal. All images are normalized for better visibility.

A.8 ELECTRONICALLY CONTROLLED PUMP PROBE USING A DIODE LASER

In Section 5.2.5 exciton lifetimes were determined by performing a PEEM pump probe experiment using a diode laser (Stradus 405-100, Vortran) with 405 nm wavelength usually used for cw illumination. By applying a TTL signal the laser was digitally modulated. An appropriate signal was generated using a delay pulse generator (9530 Series, Quantum Composers). The laser output was checked with a fast silicon photodiode (PDA10A-EC, Thorlabs), the measured signal is shown in Figure A.7 (blue curve) together with the respective TTL signal (black curve). The delay is defined from center to center of the pulses as sketched in the plot and was variated for the measurement of the time dependence. The output of the laser shows obvious deviations from the trigger signal due to a limited bandwidth of the laser. The photoemission signal obtained by the DLD shows the same shape. Although these deviations from a rectangular shape will have some minor effects on the temporal evolution of the photoemission signal, the effect is small compared to the temporal width of the pulses and is systematic for all delay times. The DLD was used with a high drift voltage of 750 V to hinder a significant dispersion of the electrons. This means that the time axis can now be interpreted as time of the photoemission since all electrons need nearly the same time to reach the detector. Only electrons emitted by the probe pulse were measured by starting the measurement ≈ 50 ns before the pulse for 7.192 µs. The signal was integrated over time and over the FoV for averaging the occurrent blinking. The reproducibility was checked although in a spatially resolved analysis this is not given. To obtain the additional photoelectron yield ΔY the signal of a probe pulse without previous pump pulse was subtracted from all measurements.

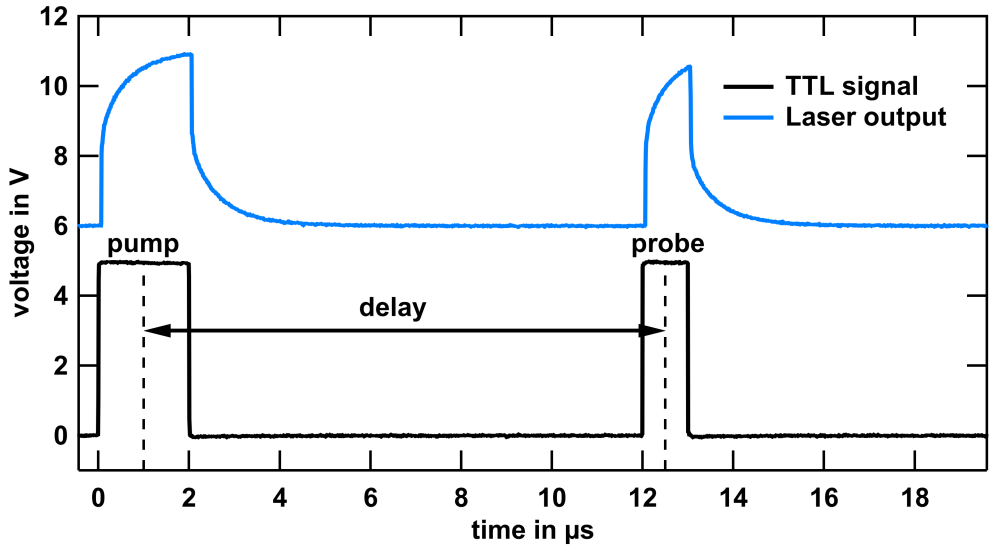

Figure A.7: TTL signal (black curve) and respective laser output (blue) measured with a photodiode as used for the pump probe experiment. The blue curve has an offset of 6 V for better visibility.

A.9 Superposition of incoming and from the surface reflected light fields

In order to evaluate the relative intensity of the irradiating light field at different distances d to the surface we have to take into account interference with light reflected from the surface. Therefore, we can calculate the local light intensity by a Fresnel type consideration. Starting with the Fresnel reflection coefficients for s- (r_S) and p-polarized light (r_P), respectively. We get

$$r_S(\theta_i) = \frac{\cos(\theta_i) - \sqrt{(n_{\text{sub}}^2 - 1) + \cos^2(\theta_i)}}{\cos(\theta_i) + \sqrt{(n_{\text{sub}}^2 - 1) + \cos^2(\theta_i)}} = \frac{\cos(\theta_i) - \sqrt{n_{\text{sub}}^2 - \sin^2(\theta_i)}}{\cos(\theta_i) + \sqrt{n_{\text{sub}}^2 - \sin^2(\theta_i)}} \tag{A.2}$$

$$r_P(\theta_i) = \frac{n_{\text{sub}}^2\cos(\theta_i) - \sqrt{(n_{\text{sub}}^2 - 1) + \cos^2(\theta_i)}}{n_{\text{sub}}^2\cos(\theta_i) + \sqrt{(n_{\text{sub}}^2 - 1) + \cos^2(\theta_i)}} = \frac{n_{\text{sub}}^2\cos(\theta_i) - \sqrt{n_{\text{sub}}^2 - \sin^2(\theta_i)}}{n_{\text{sub}}^2\cos(\theta_i) + \sqrt{n_{\text{sub}}^2 - \sin^2(\theta_i)}} \tag{A.3}$$

with the angle of incidence of $\theta_i = 65°$ and the refractive index of the substrate n_{sub}. The irradiating field can now be expressed as

$$\boldsymbol{E_i} + \boldsymbol{E_r} = E_P[1 - r_P\delta(d)]\cos(\theta_i)\boldsymbol{e_x} - E_P[1 + r_P\delta(d)]\sin(\theta_i)\boldsymbol{e_z} + E_S[1 + r_S\delta(d)]\boldsymbol{e_y} \tag{A.4}$$

with E_P, E_S being the amplitudes of the p- and s-polarized component of the incident field and $\delta(d) = \exp(i2kd\cos(\theta_i))$ where k is the wave vector in vacuum and being parallel to $\boldsymbol{e_x}$.

BIBLIOGRAPHY

[1] C. W. Tang, S. A. VanSlyke, and C. H. Chen, J. Appl. Phys. **65**, 3610 (1989).

[2] M. A. Baldo et al., Nature **395**, 151 (1998).

[3] A. Rose, Z. Zhu, C. F. Madigan, T. M. Swager, and V. Bulović, Nature **434**, 876 (2005).

[4] B. Kippelen and J.-L. Brédas, Energy & Environmental Science **2**, 251 (2009).

[5] I. D. W. Samuel and G. A. Turnbull, Chem. Rev. **107**, 1272 (2007).

[6] N. G. Bastús, J. Piella, and V. Puntes, Langmuir **32**, 290 (2015).

[7] M. Chanana and L. M. Liz-Marzán, Nanophotonics **1** (2012).

[8] P. K. Jain, X. Huang, I. H. El-Sayed, and M. A. El-Sayed, Acc. Chem. Res. **41**, 1578 (2008).

[9] G. M. Akselrod et al., Nat. Commun. **5** (2014).

[10] M. Pope, N. E. Geacintov, and F. Vogel, Molecular Crystals **6**, 83 (1969).

[11] M. Bahrami et al., J. Phys. B: At., Mol. Opt. Phys. **51**, 144002 (2018).

[12] S. A. Maier, *Plasmonics: Fundamentals and Applications*, Springer US, 2007.

[13] A. Sommerfeld and H. Bethe, *Elektronentheorie der Metalle*, Springer Berlin Heidelberg, 1967.

[14] P. B. Johnson and R. W. Christy, Phys. Rev. B **6**, 4370 (1972).

[15] K. Kopitzki and P. Herzog, *Einführung in die Festkörperphysik*, Vieweg + Teubner Verlag, 2007.

[16] H. Raether, *Surface Plasmons on Smooth and Rough Surfaces and on Gratings*, Springer Berlin Heidelberg, 1988.

[17] J. A. Scholl, A. L. Koh, and J. A. Dionne, Nature **483**, 421 (2012).

[18] J. R. Krenn et al., J. Microsc. **202**, 122 (2001).

[19] A. Otto, Zeitschrift für Physik A **216**, 398 (1968).

[20] E. Kretschmann and H. Raether, Zeitschrift für Naturforschung A **23**, 2135 (1968).

[21] D. Podbiel, P. Kahl, and F.-J. M. zu Heringdorf, Appl. Phys. B **122** (2016).

[22] J. D. Jackson, *Classical Electrodynamics*, John Wiley & Sons Inc, 1998.

[23] C. F. Bohren and D. R. Huffman, *Absorption and Scattering of Light by Small Particles*, Wiley, 1998.

[24] G. Mie, Ann. Phys. **330**, 377 (1908).

[25] A. L. Aden and M. Kerker, J. Appl. Phys. **22**, 1242 (1951).

[26] A. Güttler, Ann. Phys. **446**, 65 (1952).

[27] J. R. Wait, Appl. Sci. Res. B **10**, 441 (1962).

[28] C. Yeh, Phys. Rev. **135**, A1193 (1964).

[29] M. Quinten, *Optical Properties of Nanoparticle Systems: Mie and Beyond*, Wiley-VCH Verlag GmbH & Co. KGaA, Weinheim, 2011.

[30] F. Borghese, P. Denti, G. Toscano, and O. I. Sindoni, Appl. Opt. **18**, 116 (1979).

[31] J. M. Gérardy and M. Ausloos, Phys. Rev. B **25**, 4204 (1982).

[32] L. W. Casperson, C. Yeh, and W. F. Yeung, Appl. Opt. **16**, 1104 (1977).

[33] C. Yeh, S. Colak, and P. Barber, Appl. Opt. **21**, 4426 (1982).

[34] J. Lermé, J. Phys. Chem. C **119**, 21087 (2015).

[35] W.-H. Yang, G. C. Schatz, and R. P. V. Duyne, J. Chem. Phys. **103**, 869 (1995).

[36] E. Moreno, D. Erni, C. Hafner, and R. Vahldieck, J. Opt. Soc. Am. A **19**, 101 (2002).

[37] R. X. Bian, R. C. Dunn, X. S. Xie, and P. T. Leung, Phys. Rev. Lett. **75**, 4772 (1995).

[38] S. C. H. Allen Taflove, *Computational Electrodynamics: The Finite-Difference Time-Domain Method*, ARTECH HOUSE INC, 2005.

[39] Calculations have been done using MiePlot v4.503 based on the code by Bohren and Huffmann [23] using the dielectric function of silver from Johnson and Christy [14].

[40] U. Kreibig and M. Vollmer, *Optical properties of metal clusters*, Springer-Verlag Berlin Heidelberg, 1995.

[41] M. Meier and A. Wokaun, Opt. Lett. **8**, 581 (1983).

[42] H. Kuwata, H. Tamaru, K. Esumi, and K. Miyano, Appl. Phys. Lett. **83**, 4625 (2003).

[43] K. L. Kelly, E. Coronado, L. L. Zhao, and G. C. Schatz, J. Phys. Chem. B **107**, 668 (2003).

[44] C. Noguez, J. Phys. Chem. C **111**, 3806 (2007).

[45] M. Scharte et al., Proc. SPIE 4456 (2001).

[46] C. Sönnichsen, *Plasmons in Metal Nanostructures*, PhD thesis, Ludwig-Maximilians-Universität München, 2001.

[47] T. Kokkinakis and K. Alexopoulos, Phys. Rev. Lett. **28**, 1632 (1972).

[48] S. Link and M. A. El-Sayed, Int. Rev. Phys. Chem. **19**, 409 (2000).

[49] A. Wokaun, J. P. Gordon, and P. F. Liao, Phys. Rev. Lett. **48**, 957 (1982).

[50] J. Lehmann et al., J. Chem. Phys. **112**, 5428 (2000).

[51] C. Sönnichsen, T. Franzl, T. Wilk, G. von Plessen, and J. Feldmann, New J. Phys. **4**, 93 (2002).

[52] S. Maier, Opt. Express **14**, 1957 (2006).

[53] T. Klar et al., Phys. Rev. Lett. **80**, 4249 (1998).

[54] S. Tan et al., J. Am. Chem. Soc. **139**, 6160 (2017).

[55] K. Kolwas and A. Derkachova, J. Quant. Spectrosc. Radiat. Transfer **114**, 45 (2013).

[56] K. Kneipp et al., Phys. Rev. Lett. **78**, 1667 (1997).

[57] V. M. Shalaev, C. Douketis, T. Haslett, T. Stuckless, and M. Moskovits, Phys. Rev. B **53**, 11193 (1996).

[58] C. E. S. Martin Pope, *Electronic Processes in Organic Crystals and Polymers*, OXFORD UNIV PR, 1999.

[59] G. M. Akselrod, *Exciton transport and Coherence in Molecular and Nanostructured Materials*, PhD thesis, Massachusetts Institue of Technology, 2013.

[60] T. Förster, Ann. Phys. **437**, 55 (1948).

[61] D. L. Dexter, J. Chem. Phys. **21**, 836 (1953).

[62] S. R. Yost, E. Hontz, S. Yeganeh, and T. V. Voorhis, J. Phys. Chem. C **116**, 17369 (2012).

[63] L. Pithan et al., Adv. Mater. **29**, 1604382 (2016).

[64] R. B. Campbell, J. M. Robertson, and J. Trotter, Acta Crystallogr. **15**, 289 (1962).

[65] W. Shockley and H. J. Queisser, J. Appl. Phys. **32**, 510 (1961).

[66] J. J. Burdett, A. M. Müller, D. Gosztola, and C. J. Bardeen, J. Chem. Phys. **133**, 144506 (2010).

[67] S.-H. Lim, T. G. Bjorklund, F. C. Spano, and C. J. Bardeen, Phys. Rev. Lett. **92** (2004).

[68] M. J. J. Coenen et al., Phys. Chem. Chem. Phys. **15**, 12451 (2013).

[69] H. Hartmann, *Licht-Materie Wechselwirkung an deponierten Molekülaggregaten und freien Silber-Nanopartikeln*, PhD thesis, Universität Rostock, 2016.

[70] M.-H. Ha-Thi, N. Shafizadeh, L. Poisson, and B. Soep, J. Phys. Chem. A **117**, 8111 (2013).

[71] E. Brüche, Zeitschrift für Physik **86**, 448 (1933).

[72] J. H. Bechtel, W. L. Smith, and N. Bloembergen, Phys. Rev. B **15**, 4557 (1977).

[73] R. W. Boyd, *Nonlinear Optics*, Elsevier, 2003.

[74] L. I. Chelaru and F.-J. M. zu Heringdorf, Surf. Sci. **601**, 4541 (2007).

[75] P. Kahl et al., Plasmonics **9**, 1401 (2014).

[76] G. Schönhense et al., Ultramicroscopy **159**, 488 (2015).

[77] N. M. Buckanie et al., J. Phys.: Condens. Matter **21**, 314003 (2009).

[78] B. P. Tonner and G. R. Harp, Rev. Sci. Instrum. **59**, 853 (1988).

[79] B. P. Tonner and G. R. Harp, J. Vac. Sci. & Tech. A **7**, 1 (1989).

[80] E. Bauer, *Surface Microscopy with Low Energy Electrons*, Springer-Verlag GmbH, 2014.

[81] W. Kaiser and C. G. B. Garrett, Phys. Rev. Lett. **7**, 229 (1961).

[82] P. Bloch, J. Appl. Phys. **35**, 2052 (1964).

[83] M. D. Jones, G. A. Massey, D. L. Habliston, and O. H. Griffith, Proc. 1st Int. Conf. Electron Emission Microscopy, pp. 177-182 (1980).

[84] G. Massey, M. Jones, and J. Johnson, IEEE Journal of Quantum Electronics **17**, 1035 (1981).

[85] H. Ueba and B. Gumhalter, Prog. Surf. Sci. **82**, 193 (2007).

[86] H. Hartmann, V. N. Popok, I. Barke, V. von Oeynhausen, and K.-H. Meiwes-Broer, Rev. Sci. Instrum. **83**, 073304 (2012).

[87] T. Lunskens et al., Phys. Chem. Chem. Phys. **17**, 17541 (2015).

[88] S. Berciaud, L. Cognet, P. Tamarat, and B. Lounis, Nano Lett. **5**, 515 (2005).

[89] A. Arbouet et al., Phys. Rev. Lett. **93**, 127401 (2004).

[90] H. Baida et al., Nano Lett. **9**, 3463 (2009).

[91] A. Campos et al., Nat. Phys. (2018).

[92] J. Olson et al., Chem. Soc. Rev. **44**, 40 (2015).

[93] A. Crut, P. Maioli, F. Vallée, and N. D. Fatti, J. Phys.: Condens. Matter **29**, 123002 (2017).

[94] K. Ertel et al., Appl. Phys. B **68**, 439 (1999).

[95] H. Hövel, Appl. Phys. A **72**, 295 (2001).

[96] M. Munzinger et al., New J. Phys. **7**, 68 (2005).

[97] M. Rohmer et al., Phys. Stat. Sol. (b) **247**, 1132 (2010).

[98] S. J. Peppernick et al., Appl. Phys. A **112**, 35 (2012).

[99] F. Evers, C. Rakete, K. Watanabe, D. Menzel, and H.-J. Freund, Surf. Sci. **593**, 43 (2005).

[100] H. Hövel and I. Barke, Prog. Surf. Sci. **81**, 53 (2006).

[101] M. Merschdorf, W. Pfeiffer, A. Thon, S. Voll, and G. Gerber, Appl. Phys. A **71**, 547 (2000).

[102] M. Rohmer et al., Appl. Phys. A **82**, 87 (2006).

[103] K. Stallberg, G. Lilienkamp, and W. Daum, J. Phys. Chem. C **121**, 13833 (2017).

[104] A. Gloskovskii, D. Valdaitsev, S. Nepijko, G. Schönhense, and B. Rethfeld, Surf. Sci. **601**, 4706 (2007).

[105] P. Z. El-Khoury et al., J. Chem. Phys. **141**, 214308 (2014).

[106] F.-J. M. zu Heringdorf, L. Chelaru, S. Möllenbeck, D. Thien, and M. H. von Hoegen, Surf. Sci. **601**, 4700 (2007), Proceedings of the Fifth International Conference on LEEM/PEEM.

[107] E. Betzig et al., Science **313**, 1642 (2006).

[108] P. Zhang, S. Lee, H. Yu, N. Fang, and S. H. Kang, Sci. Rep. **5** (2015).

[109] G. V. Hartland, Chem. Rev. **111**, 3858 (2011), PMID: 21434614.

[110] C. Sönnichsen et al., Phys. Rev. Lett. **88**, 077402 (2002).

[111] K. Sell, *Electronic and structural properties of deposited silver nanoparticles: a STM and GISAXS study*, PhD thesis, Universität Rostock, 2010.

[112] I. H. Malitson, J. Opt. Soc. Am. **55**, 1205 (1965).

[113] M. A. Green, Sol. Energy Mater. Sol. Cells **92**, 1305 (2008).

[114] J. Lermé et al., J. Phys. Chem. C **117**, 6383 (2013).

[115] R. Ruppin, Surf. Sci. **127**, 108 (1983).

[116] P. Nordlander, C. Oubre, E. Prodan, K. Li, and M. I. Stockman, Nano Lett. **4**, 899 (2004).

[117] M. W. Knight, Y. Wu, J. B. Lassiter, P. Nordlander, and N. J. Halas, Nano Lett. **9**, 2188 (2009).

[118] J. Lermé, Generalized Mie Calculations, private communication 2018.

[119] C. Fadley and D. Shirley, Journal of Research of the National Bureau of Standards Section A: Physics and Chemistry **74A**, 543 (1970).

[120] A. W. Dweydari and C. H. B. Mee, Phys. Stat. Sol. (a) **27**, 223 (1975).

[121] H. Hövel, S. Fritz, A. Hilger, U. Kreibig, and M. Vollmer, Phys. Rev. B **48**, 18178 (1993).

[122] V. N. Popok, I. Barke, E. E. Campbell, and K.-H. Meiwes-Broer, Surf. Sci. Rep. **66**, 347 (2011).

[123] M. Hansen and K. Anderko, *Constitution of Binary Alloys*, McGraw-Hill Book Company., New York et.al., 1958.

[124] P. Fojan et al., Sens. Actuators, B **212**, 377 (2015).

[125] F. Stietz et al., Phys. Rev. Lett. **84**, 5644 (2000).

[126] T. Vartanyan, J. Bosbach, F. Stietz, and F. Träger, Appl. Phys. B **73**, 391 (2001).

[127] F. Hubenthal and F. Träger, Chemical damping of the localized surface plasmon polariton resonance: infuence of different chemical environments, in *Synthesis and Photonics of Nanoscale Materials VIII*, edited by D. B. Geohegan, J. J. Dubowski, and F. Träger, SPIE, 2011.

[128] J. Bosbach, C. Hendrich, F. Stietz, T. Vartanyan, and F. Träger, Phys. Rev. Lett. **89**, 257404 (2002).

[129] Tanvi et al., J. Appl. Phys. **117**, 083111 (2015).

[130] S. J. Peppernick, A. G. Joly, K. M. Beck, and W. P. Hess, J. Chem. Phys. **138**, 154701 (2013).

[131] A. Einstein, Ann. Phys. **322**, 132 (1905).

[132] F. Himpsel et al., Proceedings of the international school of physics, in *Enrico Fermi on Photoemission and Absorption Spectroscopy of Solids and Interfaces with Synchrotron Radiation*, edited by M. Campagna and R. Rosei, volume Course CVIII, p. 203, Elsevier, Amsterdam, 1990.

[133] V. Chakarian, D. Shuh, J. Yarmoff, M. Håkansson, and U. Karlsson, Surf. Sci. **296**, 383 (1993).

[134] M. Cinchetti and G. Schönhense, J. Phys.: Condens. Matter **17**, S1319 (2005).

[135] C. N. Berglund and W. E. Spicer, Phys. Rev. **136**, A1044 (1964).

[136] E. Knoesel, A. Hotzel, T. Hertel, M. Wolf, and G. Ertl, Surf. Sci. **368**, 76 (1996).

[137] M. Bauer and M. Aeschlimann, J. Electron Spectrosc. Relat. Phenom. **124**, 225 (2002).

[138] J. J. Quinn, Phys. Rev. **126**, 1453 (1962).

[139] R. Ritchie and J. Ashley, J. Phys. Chem. Solids **26**, 1689 (1965).

[140] X.-Y. Zhu, J. Phys. Chem. B **108**, 8778 (2004).

[141] L. G. Gerchikov, C. Guet, and A. N. Ipatov, Phys. Rev. A **66** (2002).

[142] C. A. Ullrich, P.-G. Reinhard, and E. Suraud, Phys. Rev. A **57**, 1938 (1998).

[143] D. Pines and P. Nozières, *The Theory of Quantum Liquids*, Benjamin, 1966.

[144] D. A. Papaconstantopoulos, *Handbook of the Band Structure of Elemental Solids*, Springer US, 2014.

[145] R. J. Hamers, R. M. Tromp, and J. E. Demuth, Phys. Rev. Lett. **56**, 1972 (1986).

[146] J. E. Demuth, B. N. J. Persson, and A. J. Schell-Sorokin, Phys. Rev. Lett. **51**, 2214 (1983).

[147] J. M. Nicholls and B. Reihl, Phys. Rev. B **36**, 8071 (1987).

[148] R. I. G. Uhrberg, G. V. Hansson, J. M. Nicholls, P. E. S. Persson, and S. A. Flodström, Phys. Rev. B **31**, 3805 (1985).

[149] P. Martensson, W.-X. Ni, G. V. Hansson, J. M. Nicholls, and B. Reihl, Phys. Rev. B **36**, 5974 (1987).

[150] T. Suzuki, Phys. Rev. B **61**, R5117 (2000).

[151] K. Takayanagi, Y. Tanishiro, M. Takahashi, and S. Takahashi, J. Vac. Sci. & Tech. A **3**, 1502 (1985).

[152] M. Aeschlimann et al., J. Chem. Phys. **102**, 8606 (1995).

[153] G. H. Fecher, O. Schmidt, Y. Hwu, and G. Schönhense, J. Electron Spectrosc. Relat. Phenom. **126**, 77 (2002).

[154] M. Wolf, A. Hotzel, E. Knoesel, and D. Velic, Phys. Rev. B **59**, 5926 (1999).

[155] F. Reif, *Fundamentals of Statistical and Thermal Physics (McGraw-Hill Series in Fundamentals of Physics)*, McGraw-Hill Science/Engineering/Math, 1965.

[156] K.-H. Meiwes-Broer, *Metal Clusters at Surfaces: Structure, Quantum Properties, Physical Chemistry (Springer Series in Cluster Physics)*, Springer, 2000.

[157] E. A. Rohlfing, D. M. Cox, A. Kaldor, and K. H. Johnson, J. Chem. Phys. **81**, 3846 (1984).

[158] W. A. de Heer, Rev. Mod. Phys. **65**, 611 (1993).

[159] H. Hövel, B. Grimm, M. Pollmann, and B. Reihl, Phys. Rev. Lett. **81**, 4608 (1998).

[160] K. H. Meiwes-Broer, Hyperfine Interact. **89**, 263 (1994).

[161] M. Seidl and J. P. Perdew, Phys. Rev. B **50**, 5744 (1994).

[162] D. M. Wood, Phys. Rev. Lett. **46**, 749 (1981).

[163] L.-S. Wang, H.-S. Cheng, and J. Fan, J. Chem. Phys. **102**, 9480 (1995).

[164] W. Gös, *Hole Trapping and the Negative Bias Temperature Instability*, PhD thesis, Technische Universität Wien, 2011.

[165] W. H. Brattain, Phys. Rev. **72**, 345 (1947).

[166] W. H. Brattain and J. Bardeen, Bell System Technical Journal **32**, 1 (1953).

[167] L. Kronik and Y. Shapira, Surf. Sci. Rep. **37**, 1 (1999).

[168] B. Streetman and G. Sanjay Banerjee, *Solid State electronic Devices (5th ed.)*, New Jersey: Prentice Hall, 2000.

[169] T. Hagen, S. Grafström, J. Kowalski, and R. Neumann, Appl. Phys. A **66**, S973 (1998).

[170] R. J. Hamers and K. Markert, Phys. Rev. Lett. **64**, 1051 (1990).

[171] R. J. Hamers and K. Markert, J. Vac. Sci. & Tech. A **8**, 3524 (1990).

[172] L. Galbraith and T. Fischer, Surf. Sci. **30**, 185 (1972).

[173] S. Grafström, J. Appl. Phys. **91**, 1717 (2002).

[174] S. Sze and K. K. Ng, *Physics of semicondutor devices*, Wiley, 2007.

[175] J. Dziewior and W. Schmid, Appl. Phys. Lett. **31**, 346 (1977).

[176] M. Schultze et al., Science **346**, 1348 (2014).

[177] T. Nakamura, N. Hirata, Y. Sekino, S. Nagaoka, and A. Nakajima, J. Phys. Chem. C **114**, 16270 (2010).

[178] J. P. Hoogenboom, J. Hernando, E. M. H. P. van Dijk, N. F. van Hulst, and M. F. García-Parajó, ChemPhysChem **8**, 823 (2007).

[179] F. D. Stefani, J. P. Hoogenboom, and E. Barkai, Phys. Today **62**, 34 (2009).

[180] J. J. Burdett and C. J. Bardeen, J. Am. Chem. Soc. **134**, 8597 (2012).

[181] G. Vaubel and H. Baessler, Phys. Stat. Sol. (b) **37**, K31 (1970).

[182] P. Delannoy and M. Schott, Phys. Stat. Sol. (b) **70**, 119 (1975).

[183] W.-L. Chan, M. Ligges, and X.-Y. Zhu, Nat. Chem. **4**, 840 (2012).

[184] J. R. Tritsch, W.-L. Chan, X. Wu, N. R. Monahan, and X.-Y. Zhu, Nat. Commun. **4** (2013).

[185] R. W. MacQueen et al., Mater. Horiz. **5**, 1065 (2018).

[186] M. Haase et al., J. Phys. Chem. B **108**, 10445 (2004).

[187] E. K. L. Yeow, S. M. Melnikov, T. D. M. Bell, F. C. D. Schryver, and J. Hofkens, J. Phys. Chem. A **110**, 1726 (2006).

[188] P. Frantsuzov, M. Kuno, B. Jankó, and R. A. Marcus, Nat. Phys. **4**, 519 (2008).

[189] X. Wang et al., Nature **459**, 686 (2009).

[190] T. D. Krauss and J. J. Peterson, J. Phys. Chem. Lett. **1**, 1377 (2010).

[191] H. Lin et al., Nano Lett. **10**, 620 (2010).

[192] E. A. Riley, C. Bingham, E. D. Bott, B. Kahr, and P. J. Reid, Phys. Chem. Chem. Phys. **13**, 1879 (2011).

[193] B. Ji et al., Nat. Nanotechnol. **10**, 170 (2015).

[194] T. D. Krauss and J. J. Peterson, Nat. Mater. **11**, 14 (2011).

[195] V. Schweikhard, A. Grubisic, T. A. Baker, and D. J. Nesbitt, J. Phys. Chem. C **115**, 83 (2010).

[196] C. N. Berglund and W. E. Spicer, Phys. Rev. **136**, A1030 (1964).

[197] M. J. Y. Tayebjee, R. G. C. R. Clady, and T. W. Schmidt, Phys. Chem. Chem. Phys. **15**, 14797 (2013).

[198] M. Voigt et al., J. Chem. Phys. **127**, 114705 (2007).

[199] L. G. Kaake, P. F. Barbara, and X.-Y. Zhu, J. Phys. Chem. Lett. **1**, 628 (2010).

[200] A. Ishii, M. Yoshida, and Y. K. Kato, Phys. Rev. B **91** (2015).

[201] Y.-Z. Ma, L. Valkunas, S. L. Dexheimer, S. M. Bachilo, and G. R. Fleming, Phys. Rev. Lett. **94** (2005).

[202] F. Fennel and S. Lochbrunner, Phys. Rev. B **92** (2015).

[203] U. Gösele, M. Hauser, U. Klein, and R. Frey, Chem. Phys. Lett. **34**, 519 (1975).

[204] S. Jang, K. J. Shin, and S. Lee, J. Chem. Phys. **102**, 815 (1995).

[205] P. G. de Gennes, J. Chem. Phys. **76**, 3316 (1982).

[206] T. Härtling, P. Reichenbach, and L. M. Eng, Opt. Express **15**, 12806 (2007).

[207] A. V. Sorokin et al., J. Phys. Chem. C **118**, 7599 (2014).

[208] P. K. Nayak, Synth. Met. **174**, 42 (2013).

[209] H. Hövel et al., Phys. Rev. B **70** (2004).

[210] J. J. Burdett, D. Gosztola, and C. J. Bardeen, J. Chem. Phys. **135**, 214508 (2011).

[211] W.-L. Chan et al., Acc. Chem. Res. **46**, 1321 (2013).

[212] Z. Birech, M. Schwoerer, T. Schmeiler, J. Pflaum, and H. Schwoerer, J. Chem. Phys. **140**, 114501 (2014).

[213] L. Valkunas, Y.-Z. Ma, and G. R. Fleming, Phys. Rev. B **73** (2006).

[214] M. Chabr, U. Wild, J. Fünfschilling, and I. Zschokke-Gränacher, Chem. Phys. **57**, 425 (1981).

[215] M. J. J. Coenen et al., Chem. Commun. **47**, 9666 (2011).

[216] G. D. Hale, S. J. Oldenburg, and N. J. Halas, Phys. Rev. B **55**, R16069 (1997).

[217] R. Glaser, *Biophysics*, Springer Berlin Heidelberg, 2012.

PUBLICATIONS

[KO-1] Stephan Bartling, Chunrong Yin, Ingo Barke, Kevin Oldenburg, Hannes Hartmann, Viola von Oeynhausen, Marga-Martina Pohl, Kelly Houben, Eric C. Tyo, Sönke Seifert, Peter Lievens, Karl-Heinz Meiwes-Broer, and Stefan Vajda. Pronounced Size Dependence in Structure and Morphology of Gas-Phase Produced, Partially Oxidized Cobalt Nanoparticles under Catalytic Reaction Conditions. *ACS Nano*, 9(6), 2015.

[KO-2] Hannes Hartmann, Ingo Barke, Aleksej Friedrich, Per-Arno Plötz, Olga S. Bokareva, Mohammadreza Bahrami, Kevin Oldenburg, Johannes A. A. W. Elemans, Robert Irsig, Karl-Heinz Meiwes-Broer, Oliver Kühn, Stefan Lochbrunner, and Sylvia Speller. Mapping Long-Lived Dark States in Copper Porphyrin Nanostructures. *The Journal of Physical Chemistry C*, 120(30), 2016.

[KO-3] Kevin Oldenburg, Sylvia Speller, and Ingo Barke. A Self-Tracking Method for Local Surface-Photovoltage Measurements on Semiconducting Surfaces. *Journal of Physics B: Atomic, Molecular and Optical Physics*, 50(20), 2017.

[KO-4] Kevin Oldenburg, Hannes Hartmann, Jean Lermé, Marga-Martina Pohl, Karl-Heinz Meiwes-Broer, Ingo Barke, and Sylvia Speller. Virtual Plasmonic Dimers for Ultrasensitive Inspection of Cluster–Surface Coupling. *The Journal of Physical Chemistry C*, 123(2), 2018.

[KO-5] Katharina Engster, Kevin Oldenburg, Ingo Barke, and Sylvia Speller. Spatially Resolved SPV Maps of the Vicinity of Silver Nanoparticles on Si(100)-p(2x1). To be published.

SUPERVISED MASTER PROJECTS

[MT-1] Bahaaeddin Irziqat. Morphological Properties of Gas-Phase Deposited Molecules on Si(111)-(7x7) Investigated by Scanning Tunneling Microscopy. Master's thesis, University of Rostock, 2017.

[MT-2] Christian Völkner. Untersuchung der Struktur und optischen Eigenschaften von Tetracen-Kristalliten. Master's thesis, University of Rostock, 2017.

[MT-3] Katharina Engster. Photospannungs-Mapping an Nanopartikeln auf Halbleiter-Oberflächen mit dem Photoemissions-Elektronenmikroskop. Master's thesis, University of Rostock, 2019.

PRESENTATIONS

Talks

2018 Workshop of the Department Life, Light & Matter, Rostock
*I*nteractions in Hybrid Nanocomposite Systems Studied by Laser-Induced Photoemission Electron Microscopy

2017 Deutsche Physikalische Gesellschaft: Spring Meeting, Dresden
*E*ffect of Substrate on Plasmonic Signatures of Silver Nanoparticles Studied by Photoemission Electron Microscopy

2016 Workshop of the Department Life, Light & Matter, Rostock
*P*lasmonic Mapping of Nanoparticles on Surfaces: Nanoscopic Light Sources for Molecules and Cells

2015 Deutsche Physikalische Gesellschaft: Spring Meeting, Berlin
A Self-Tracking Spectroscopic Method for Surface Photovoltage Measurements on Semiconducting Surfaces

Posters

2018 Workshop of the Department Life, Light & Matter, Rostock
*P*lasmonic Cluster-Surface Coupling unraveled by Size-Correlated Single-Object Photoemission

2018 Workshop of the Department Life, Light & Matter, Rostock
*I*nteractions in Hybrid Nanocomposite Systems Studied by Photoemission Electron Microscopy

2018 Deutsche Physikalische Gesellschaft: Spring Meeting, Berlin
*I*nteractions in Hybrid Nanocomposite Systems Studied by Laser-Induced Photoemission Electron Microscopy

2017 Deutsche Physikalische Gesellschaft Collarborative Research Center 652:"Strong correlations and collective effects in radiations fields: Coulomb systems, clusters and particles", Final Colloquium, Rostock
*S*ize Dependence of Plasmonic Photoemission from Individual Supported Silver Nanoparticles

2016 QUTIF Research School, Rostock
*P*lasmon-Enhanced Photoemission from Individual Silver Nanoparticles

2016 Deutsche Physikalische Gesellschaft: Spring Meeting, Regensburg
*P*lasmon-Enhanced Photoemission from Individual Silver Nanoparticles

2016 Cluster Surface Interaction, Argonne National Lab, USA
*P*lasmon-Enhanced Photoemission from Individual Silver Nanoparticles

2015 FOCUS PEEM Workshop, Huenstetten
*E*xcitation Processes in Copper Porphyrin Aggregates Studied by Multi-Photon Photoemission Electron Microscopy

2015 Clustertreffen, Lindow
*L*ocal Light-Induced Potential Variations Mapped with a Self-Tracking Spectroscopic Method for Semiconducting Surfaces

2015 CERF, Rostock
*L*ocal Light-Induced Potential Variations: A Self-Tracking Spectroscopic Method for Semiconducting Surfaces

2014 Deutsche Physikalische Gesellschaft: Spring Meeting, Dresden
*P*hotovoltage on Metallic and Semiconducting Surfaces in Vicinity of Metallic Nanostructures